

2017

Ruthenium Mesoionic Carbene Complexes and their Applications in Energy Generation and Storage

Brown, Douglas

Brown, D. (2017). Ruthenium Mesoionic Carbene Complexes and their Applications in Energy Generation and Storage (Doctoral thesis, University of Calgary, Calgary, Canada). Retrieved from <https://prism.ucalgary.ca>. doi:10.11575/PRISM/27698

<http://hdl.handle.net/11023/3779>

Downloaded from PRISM Repository, University of Calgary

UNIVERSITY OF CALGARY

Ruthenium Mesoionic Carbene Complexes and their Applications in Energy Generation and
Storage

by

Douglas Brown

A THESIS

SUBMITTED TO THE FACULTY OF GRADUATE STUDIES
IN PARTIAL FULFILMENT OF THE REQUIREMENTS FOR THE
DEGREE OF DOCTOR OF PHILOSOPHY

GRADUATE PROGRAM IN CHEMISTRY

CALGARY, ALBERTA

APRIL, 2017

© Douglas Brown 2017

Abstract

A series of *bis*(tridentate) ruthenium complexes bearing 2',6'-*bis*(1-(2,6-dimethyl-4-bromophenyl)-3-methyl-1,2,3-triazol-4-yl-5-ylene)pyridine (C[^]N[^]C) have been synthesized and characterized. The complexes of the type [Ru(terpy)(C[^]N[^]C)]²⁺ and derivatives herein, exhibit longer excited state lifetimes (τ) than the archetypical [Ru(terpy)₂]²⁺ (terpy = 2,2':6,2''-terpyridine; τ = 0.25 ns) by several orders of magnitude ($\tau \sim 8 \mu\text{s}$). Their unique ligand geometry and robust sensitization of TiO₂ offer insightful design considerations in both dye-sensitized solar cell (DSSC) and water oxidation.

In Chapter 2, a series of ruthenium complexes were investigated for their emission properties, which exhibited some of the longest room temperature excited state lifetimes ever reported. Modifications of both ligand fragments were conducted with electron-donating groups and electron-withdrawing groups, which enabled fine-tuning of the triplet metal-to-ligand charge transfer (³MLCT) state. This was a result of destabilizing the normally thermally accessible deactivating triplet metal centered (³MC) state. The location of the lowest-unoccupied molecular orbital (LUMO) could be tuned to reside on either the terpy or C[^]N[^]C fragment through chemical modification.

Chapter 3 provides details on the sensitization of TiO₂ through the cooperative anchoring of phosphonate (-PO₃H₂) and carboxylate (-CO₂H) groups and their performance in the DSSC. Using a combination of anchoring groups provided an opportunity to address the instability due to hydrolysis with the -PO₃H₂ group, while maintaining electronic communication through the preferred -CO₂H. The geometry of the two tridentate ligands within the complexes permitted them to be bind through both ligands to the TiO₂ surface. Temporal stability studies identified the cooperative binding approach successfully increased hydrolysis resistance and that the –

CO₂H moiety on the terpy ligand was critical for higher power conversion efficiencies (*PCE* ~ 0.2%). The absorption spectrum showed modest absorptions over the visible spectrum 400 to 650 nm ($\lambda_{\text{max}} \sim 470 \text{ nm}$; ϵ up to $1.0 \times 10^4 \text{ M}^{-1}\text{cm}^{-1}$), which limited the maximum *PCE* ~ 2% based on the solar spectrum.

In Chapter 4, the cooperative anchoring strategy was exploited in the heterogenization of a molecular water oxidation catalyst. The title complex ($[\text{Ru}(\text{bpy}-\text{CO}_2\text{H})(\text{C}^{\wedge}\text{N}^{\wedge}\text{C}-\text{PO}_3\text{H}_2)\text{Cl}]^{2+}$) investigated was anchored to TiO₂ and the catalytic oxidation of water ($\sim 4.0 \mu\text{A}/\text{cm}^2$; TOF 0.0004s^{-1}) was demonstrated.

Acknowledgements

I would like to thank both of my supervisors Dr. Curtis Berlinguette and Dr. Todd Sutherland for their support and mentorship throughout graduate school. Thank you Curtis for inspiring me and believing in my potential to be successful. Todd thank you for sharing your passion in the exploration of science and discovery. Paolo, Kiyoshi and Derek thank you for showing me how to succeed in graduate school and making the lab feel like home. Joel thanks for all the good times and always being ready to challenge every assumption and truth to a rigorous debate. Chris thank you for your friendship and sharing your passion for science. My extended family in Vancouver Demitri and Jessica, thank you for all your support through the years, I am grateful. To my parents Barb and Geoff I am so grateful and thankful to have your love and support through which this was all possible. Thank you to all those who have made my day-to-day life at graduate school truly blessed and I will miss you all!

Dedication

This thesis is dedicated to my parents who value education deeply and always inspired me to explore.

Table of Contents

Abstract.....	ii
Acknowledgements.....	iv
Dedication.....	v
Table of Contents.....	vi
List of Tables.....	viii
List of Figures.....	ix
List of Schemes.....	xiii
List of Symbols, Abbreviations and Nomenclature.....	xiv
Epigraph.....	xxi
CHAPTER 1 : INTRODUCTION.....	1
1.1. Motivation: Solar Energy Generation and Storage, Climate Change and Sustainability.....	1
1.2. Sensitization of Semiconductors and Ruthenium Complexes.....	8
1.2.1 Sensitization of Metal Oxides.....	8
1.2.2 Ruthenium Complexes.....	9
1.2.3 Photophysics.....	10
1.2.4 Electrochemistry.....	15
1.3. Power Generation: The Dye-Sensitized Solar Cell.....	15
1.3.1 Principle of Operation.....	15
1.3.2 Characterization Methods.....	19
1.3.2.1 Current Density-Voltage Measurements (<i>J-V</i> curves).....	19
1.3.2.2 Incident Photon-to-Current Conversion Efficiency (<i>IPCE</i>).....	20
1.3.2.3 Diffuse Reflectance Infrared Fourier Transform (DRIFTS).....	22
1.4. Power Storage: Molecular Heterogeneous Water Oxidation.....	22
1.4.1 Principle of Operation.....	22
1.4.2 Characterization Methods.....	25
1.4.2.1 Catalysis.....	25
1.5. Thesis Objectives and Goals.....	27
CHAPTER 2 : LONG LIVE THE EXCITED STATES OF METAL TO LIGAND CHARGE TRANSFER.....	29
2.1. Introduction.....	29
2.2. Microsecond Excited-State Lifetimes in <i>Bistridentate</i> Ruthenium-Terpyridine complexes.....	30
2.2.1 Abstract.....	30
2.2.2 Introduction.....	31
2.2.3 Results.....	35
2.3. Experimental Details.....	46
2.3.1 Synthesis.....	46
2.3.2 Characterization.....	59
CHAPTER 3 : STABILIZATION OF RUTHENIUM SENSITIZERS TO TiO ₂ SURFACES THROUGH COOPERATIVE ANCHORING GROUPS.....	60
3.1 Introduction.....	60

3.2 Stabilization of Ruthenium Sensitizers to TiO ₂ Surfaces Through Cooperative Anchoring Groups.....	61
3.2.1 Abstract.....	62
3.2.2 Introduction.....	62
3.2.3 Results.....	64
3.3 DSSC optimization and performance studies from collaboration	73
3.4 Experimental Details.....	76
3.4.1 Synthesis	76
3.4.2 Physical Methods	89
 CHAPTER 4 : MOLECULAR HETEROGENEOUS RUTHENIUM WATER OXIDATION CATALYSIS.....	 92
4.1 Introduction.....	92
4.2 Results and Discussion	93
4.2.1 Electrochemical and UV-vis Spectroscopic Characterization	98
4.2.2 Catalytic water oxidation experiments.....	103
4.3 Summary.....	110
4.4 Conclusions.....	111
4.5 Experimental Details.....	111
4.5.1 Synthesis	111
4.5.2 Physical Methods	116
 CHAPTER 5 : CONCLUSIONS AND FUTURE DIRECTIONS	 117
5.1. Conclusions.....	117
5.2. Future Directions	120
 APPENDIX.....	 123
1.1. Experimental Details and Supporting Information for Chapter Two (<i>J. Am. Chem. Soc.</i> , 2012, <i>134</i> , 12354–12357)	123
1.2. Experimental Details and Supporting Information for Chapter Three (<i>J. Am. Chem. Soc.</i> , 2013, <i>135</i> , 1692–1695)	124
 REFERENCES	 148

List of Tables

Table 2.1. Photophysical and electrochemical data for 2.1-2.4 and [Ru(terpy) ₂](PF ₆) ₂	43
Table 2.2. Excited-state lifetime (τ) data for 2.2-2.4 . (Values expressed in units of $\mu\text{s.}^a$)	46
Table 3.1. Photophysical data for ester precursors 3.1'-3.4'	66
Table 3.2. Photophysical and photovoltaic data obtained for the title complexes under AM1.5 conditions.	70
Table 3.3. Selected DSSC Data for the Ru(II) Complexes Measured under AM1.5 Light Conditions	76

List of Figures and Illustrations

Figure 1.1. Electricity generation in U.S in 2015 and Global 2014. Note sum of components do not equal 100% due to independent rounding. ^{11,12}	2
Figure 1.2. The price of installed solar in the U.S. over the last decade. ²⁴	4
Figure 1.3. Performance comparison the DSSC and c-Si at various light intensities.....	5
Figure 1.4. Grätzel's famous N3 dye that was the first dye reported with a DSSC <i>PCE</i> > 5% and SM315 that broke the <i>PCE</i> = 13% barrier.	6
Figure 1.5. A simplified orbital diagram for [Ru(bpy) ₂] ²⁺ and [Ru(terpy) ₂] ²⁺ in an idealized octahedral environment showing relevant orbitals and transitions.....	11
Figure 1.6. Energy diagram illustrating the thermal accessibility of the ³ MC state in [Ru(terpy) ₂] ²⁺	12
Figure 1.7. Selected ruthenium polypyridyl compounds for discussion of excited-state lifetimes.....	13
Figure 1.8. Example of determining the HOMO-LUMO energy gap (<i>E</i> ₀₋₀) by normalization of the emission peak to the lowest major MLCT energy of the absorption spectrum.	14
Figure 1.9. Dye-sensitized solar cell schematic and relevant energy levels for a dye (S = HOMO/S* = lowest excited state) in a working device. Rate constants shown for electron injection (<i>k</i> ₁), dye regeneration (<i>k</i> ₂), electron transport (<i>k</i> ₃) and interfacial recombination (<i>k</i> ₄).....	18
Figure 1.10. Representative photocurrent density-voltage curve and relevant performance metrics identified.....	20
Figure 1.11. Representative <i>IPCE</i> curve for illustrating the fraction of incident light that is converted into electricity.....	21
Figure 1.12. Simplified mechanism of Ru(Mebimpy)(4,4'-((HO) ₂ OPCH ₂) ₂ bpy)(OH ₂) ²⁺ (Mebimpy = 2,6-bis(1-methylbenzimidazol-2-yl) mediated water oxidation adopted from reference 101.....	23
Figure 1.14. <i>E</i> _{1/2} vs pH a typical Pourbaix diagram for a [Ru ^{II} -OH ₂] ²⁺ complex.	25
Figure 2.1 Energies (reported vs NHE) of HOMOs (black) and LUMOs (red) of benchmark complexes. The energies of the lowest excited states are approximated as <i>E</i> _{1/2,ox} + <i>E</i> ₀₋₀ . [bpy = 2,2'-bipyridine; terpy = 2,2':6',2"-terpyridine].....	32
Figure 2.2. Benchmark and title Ru(II) complexes for excited-state lifetime study. (Counterion = BF ₄ ⁻ in all cases.).....	33

Figure 2.3. Summary of relevant energy levels for 2.1-2.4 . The HOMO and LUMO energies correspond to the ground- and excited-state oxidation potentials, respectively; the LUMO+1 and higher levels are estimated from computational data. Data for $[\text{Ru}(\text{terpy})_2]^{2+}$ is also provided for comparison.....	37
Figure 2.4 UV- <i>vis</i> absorption spectrum of $\text{Ag}(\text{C}^{\wedge}\text{N}^{\wedge}\text{C}-\text{Br})$ recorded in MeCN under ambient conditions.....	39
Figure 2.5 Experimental UV- <i>vis</i> absorption spectrum of 2.2 overlaid with calculated transitions represented by vertical bars. Details of the three largest calculated transitions (theoretical wavelength in nm, oscillator strength, % contribution to transition): λ_1 : HOMO-1 \rightarrow LUMO (484, 0.065, 54%); λ_2 : HOMO \rightarrow LUMO+3 (437, 0.230, 30%); λ_3 : HOMO-1 \rightarrow LUMO+5 (360, 0.058, 72%).....	40
Figure 2.6 Experimental UV- <i>vis</i> absorption spectrum of 2.3 overlaid with calculated transitions represented by vertical bars. Details of the three largest calculated transitions (theoretical wavelength in nm, oscillator strength, % contribution to transition): λ_1 : HOMO \rightarrow LUMO+2 (487, 0.1411, 65%); λ_2 : HOMO-2 \rightarrow LUMO (446, 0.2021, 43%); λ_3 : HOMO \rightarrow LUMO+5 (358, 0.1037, 91%).....	41
Figure 2.7. Experimental UV- <i>vis</i> absorption spectrum of 2.4 overlaid with calculated transitions represented by vertical bars. Details of the three largest calculated transitions (theoretical wavelength in nm, oscillator strength, % contribution to transition): λ_1 : HOMO \rightarrow LUMO+2 (486, 0.1464, 65%) λ_2 : HOMO-2 \rightarrow LUMO (446, 0.1848, 46%) λ_3 : HOMO \rightarrow LUMO+5 (356, 0.1006, 91%). Select molecular orbitals are also shown.....	42
Figure 2.8. UV- <i>vis</i> and normalized emission spectra for 2.1 (orange), 2.2 (red), 2.3 (green) and 2.4 (blue) recorded in deaerated ethanol/methanol (80:20 v/v) at ambient temperatures. (Emission spectra are normalized to MLCT absorptions). <i>Inset</i> : Representative time-correlated single photon emission decay profile for 2.4 (blue) overlaid with a monoexponential fit (red) in ethanol/methanol (80:20 v/v).	44
Figure 3.1 Ruthenium(II) complexes bearing carboxylate (3.1 and 3.2), phosphonate (3.3) and both (3.4) anchoring groups (counterion = BF_4^- in all cases). Single-crystal X-ray diffraction structural depictions of the ester derivatives 3.1' , 3.3' and 3.4' are shown to illustrate that the phosphonate and/or carboxylate functional groups are geometrically positioned for simultaneous surface binding. Ellipsoids are shown at a 50% probability. Atom colors are given for carbon (grey), nitrogen (blue), oxygen (red), phosphorous (orange) and ruthenium (teal). Hydrogen atoms, anions, methylcarboxylate and diethylphosphonate ester linkages are omitted for clarity. See appendix for crystallographic data.	65
Figure 3.2. Energy level diagram for complexes 3.1'-3.4' . The ground-state energy (S) corresponds to the oxidative redox couple determined by cyclic voltammetry in 0.1 M $\text{NBu}_4\text{BF}_4/\text{MeCN}$ (internal standard: $[\text{Fc}]^+ / [\text{Fc}]^0 = +0.63 \text{ V vs NHE}$); the excited-state energy (S^*) corresponds to $S + E_{0-0}$ (E_{0-0} = intersection point of the absorption and emission curves, where the latter is normalized to the lowest energy $^1\text{MLCT}$ band; see	

Appendix); HOMO and LUMO molecular orbitals (0.05 a.u.) of the singlet states are plotted as representations of S and S*, respectively. (The nearly isogenic LUMO+1 for 3.4' is shown because it is a better representation of the LUMO of 3.4 .).....	69
Figure 3.3. Kubelka-Munk DRIFTS spectra of 3.1-3.4/TiO₂ and 3.4/KBr . Subscripts “s” and “as” represent symmetric and asymmetric, respectively.	71
Figure 3.4. Temporal stability (pH 7.0) of 3.1-3.4/TiO₂ submerged in water. Data for N3 is also shown so as to highlight the enhanced stability engendered by the cooperatively binding anchoring groups of 3.4	72
Figure 3.5 Series of dyes tested in the DSSC for device performance	74
Figure 3.6 Comparison of the excited-state and ground-state redox potentials (values refer to the NHE scale) with the relevant redox potential of the electrolyte and the conduction band edge (solid line) as well as the appropriate position of the Fermi level (dashed line) of TiO ₂ . Ground states determined by cyclic voltammetry. Excited states determined at the intersection of the absorption and emission spectra with the latter being normalized with respect to the lowest-energy absorption.....	75
Figure 4.1. Surface-bound [Ru(Mebimpy)(4,4'-((HO) ₂ OPCH ₂) ₂ bpy)(OH ₂)] ²⁺ [Mebimpy = 2,6-bis(1-methylbenzimidazol-2-yl)pyridine; bpy = 2,2'-bipyridine] by Meyer and coworkers.....	93
Figure 4.2. Molecular Ruthenium complex 4.1 for heterogeneous molecular water oxidation. ..	94
Figure 4.4. UV-vis absorption spectra for a) 4.1' in H ₂ O (blue), MeCN (red) and DCM (green) and b) 4.1' (blue) and 4.1 (black) in H ₂ O.....	99
Figure 4.5. Temporal study of Ru(bpy-COOCH ₃)(terpy)Cl (red), 4.1/TiO₂ (black) bound to titania and submerged in neutral water over the period of 1 h. Temporal study of 4.1/TiO₂ (blue) in pH 4 Britton-Robinson buffer.	100
Figure 4.6. Kubelka-Munk DRIFTS spectra of 4.1/TiO₂ . Subscripts “s” and “as” represent symmetric and asymmetric, respectively.....	101
Figure 4.7 Proposed binding geometries for catalyst 4.1 to titania substrate when a) both carboxylate groups are bound and b) all groups are partially bound.....	102
Figure 4.8. Cyclic voltammograms of 4.1' measured in deaerated MeCN using a platinum working electrode with a TBABF ₄ electrolyte (0.1 M) at 100 mVs ⁻¹ . Reference electrode Ag/Ag ⁺ . Referenced using ferrocene reported vs NHE (+0.62 V). Relevant redox couples are listed.....	103
Figure 4.9. Cyclic voltammograms of 4.1' with different amounts of spiked H ₂ O measured in deaerated MeCN using a platinum working electrode with a TBABF ₄ electrolyte (0.1 M) at 10 mVs ⁻¹ . Reference electrode Ag/Ag ⁺ . Referenced using ferrocene reported vs NHE (+0.62 V). a) MeCN/100H ₂ O (red), 4.1' in MeCN/100H ₂ O (black) and 4.1' in MeCN	

(blue). b) 4.1' in MeCN (blue), in MeCN/100H ₂ O (black), in MeCN/150H ₂ O. (green) and in MeCN/200H ₂ O (orange).	104
Figure 4.10 Cyclic voltammograms with different amounts of spiked H ₂ O measured in deaerated MeCN using a platinum working electrode with a TBABF ₄ electrolyte (0.1 M) at 10 mVs ⁻¹ . Reference electrode Ag/Ag ⁺ . Referenced using ferrocene reported vs NHE (+0.62 V). a) Background MeCN (black), MeCN/50H ₂ O (red) and MeCN/100H ₂ O (green). d) Zoomed in version of graph Figure 4.9b (4.1') (see for details).	105
Figure 4.11. Cyclic voltammograms of 4.1' at scan rates 10 mVs ⁻¹ (black), 50 mVs ⁻¹ (green), 100 mVs ⁻¹ (orange) and 500 mVs ⁻¹ (blue) measured in deaerated MeCN/200H ₂ O using a platinum working electrode with a TBABF ₄ electrolyte (0.1 M). 10 mVs ⁻¹ . Reference electrode Ag/Ag ⁺ . Referenced using ferrocene reported vs NHE (+0.62 V). Inset shows <i>E</i> _{pc} (•) and <i>E</i> _{pa} (°) peak currents of Ru(III/II) couple plotted vs scan rate.	105
Figure 4.12. Cyclic voltammograms in acetate buffer (0.1 M) at pH 4 of a) 4.1 in solution with glass carbon working electrode and b) 4.1/TiO₂ bound to titania as working electrode. Scan rate 10 mVs ⁻¹ . Reference electrode Ag/Ag ⁺	106
Figure 4.13. UV-vis spectra of a) 4.1 (blue) in H ₂ O and 4.1/TiO₂ (black) and b) 4.1/TiO₂ (black) and Ru(terpy)(bpy-CO ₂ H)Cl/TiO ₂ (red).....	107
Figure 4.14. Cyclic voltammograms of 4.1/TiO₂ a) at scan rates 10 mVs ⁻¹ (blue), 50 mVs ⁻¹ (black), 200 mVs ⁻¹ (green) and 500 mVs ⁻¹ (orange) and b) shows <i>E</i> _{pc} (•) and <i>E</i> _{pa} (°) peak currents of Ru(III/II) couple plotted vs square root of scan rate. Measured in acetate buffer (0.1 M) at pH 4. Reference electrode Ag/Ag ⁺	108
Figure 4.16. Cyclic voltammograms of 4.1/TiO₂ (black) and Ru(bpy-CO ₂ H)(terpy)Cl/TiO ₂ (red) taken at a) 10 mVs ⁻¹ in acetate at pH 4.0; reported vs. Ag/Ag ⁺ and b) Sustained catalysis at 1.3 V.	110
Figure 5.1 Top performing dye from Chapter 3 that illustrated cooperative binding approach using carboxylate and phosphonate anchoring groups.	119
Figure 5.2 Water oxidation catalyst from Chapter 4.....	120
Figure 5.3. Two operational modes of smart window with solar spectrum overlaid with absorption spectrum of 4.1/TiO₂ and predicted transparent mode 1 window.	121
Figure 5.4 Proposed Fe(terpy-CO ₂ H)(C [^] N [^] C-PO ₃ H ₂) complex	122

List of Schemes

Scheme 2.1 Transmetallation scheme for complexes 2.1-2.4	36
Scheme 2.2 Synthetic route for compound 2.9	48
Scheme 2.3 Synthetic route for compound 2.11	49
Scheme 2.4 Synthetic route for the transmetallation silver carbene complex ($\text{Ag-C}^{\wedge}\text{N}^{\wedge}\text{C-R}^2$)..	50
Scheme 2.5. Synthesis of Ruthenium terpy derivatives for transmetallation reaction.	53
Scheme 3.1 Synthesis of azido phosphonate	77
Scheme 3.2. Synthesis of the transmetallating reagent ($\text{Ag-C}^{\wedge}\text{N}^{\wedge}\text{C-R}^2$).....	80
Scheme 3.3. Synthesis of mesoionic carbene complexes	85
Scheme 4.1. Synthetic approach to synthesizing the water oxidation catalyst 4.1	95
Scheme 4.2. Cross-coupling reactions with diethyl phosphonate and different aromatic halogens.	96
Scheme 4.3. Copper catalyzed cyclization reaction and methylation with Meerwein's salt.	97

List of Symbols, Abbreviations and Nomenclature

Symbol	Definition
1	singlet state
3	triplet state
\sim	approximately
*	antibonding
\approx	approximately equal to
18-NRT	Dyesol™ active TiO ₂ paste (20 nm particles)
Å	angstrom
ABS	EtOH absolute ethanol
AcOH	acetic acid
AM1.5	Air Mass 1.5 solar spectrum
Anal. Calcd.	calculated (elemental) analysis
aq.	aqueous
b	broad (NMR)
B3	Becke's 3-parameter exchange functional
bpy	2,2'-bipyridine
bpy-CO ₂ H	4,4'-dicarboxylic acid 2,2'-bipyridine
bpy-CO ₂ Me	4,4'-dimethoxycarbonyl-2,2'-bipyridine
c-Si	crystalline silicon
$C^{\wedge}N^{\wedge}C$	4,4'-(pyridine-2,6-diyl)bis(1-(2,4,6-trimethyl-phenyl)-3-methyl-1H-1,2,3-triazol-3-ium) tetrafluoroborate
$C^{\wedge}N^{\wedge}C-R^2$	4,4'-(pyridine-2,6-diyl)bis(1-(2,6-dimethyl-4-substituted-phenyl)-3-

	methyl-1H-1,2,3-triazol-3-ium) tetrafluoroborate derivatives
ca.	circa
calcd.	calculated
Ce	(IV) generic Ce(IV) species
CV	cyclic voltammogram
D	deuterium
d	doublet (NMR)
d6-DMSO	deuterated dimethylsulfoxide
DCM	dichloromethane
dd	doublet of doublets (NMR)
ddd	doublet of doublet of doublets (NMR)
DFT	density functional theory
DMF	N,N-dimethylformamide
DMII	1,3-dimethylimidazolium
DMSO	dimethylsulfoxide
dpq	2,6-di(8'-quinolinyl)pyridine
DRIFTS	diffuse reflectance infrared fourier transform spectroscopy
DSSC	dye-sensitized solar cell
e	electron
E	reduction potential
e.g.	exempli gratia
E(S+/S)	ground-state oxidation potential
E(S+/S*)	excited-state oxidation potential

E_{0-0}	zero-zero excitation energy
$E_{1/2}$	mid-point of $E_{p,a}$ and $E_{p,c}$
EA	elemental analysis
E_{cb}	conduction band energy
EDG	electron-donating group
EDTA	ethylenediaminetetraacetic acid
E_f	Fermi level energy
eg	metal orbitals in (pseudo)octahedral geometry of σ character
EI	electron impact ionization
EI-MS	electron-impact mass spectrometry
E°	standard reduction potential
E_{pa}	potential of the anodic peak
E_{pc}	potential of the cathodic peak
eq	equivalent
Eq.	equation
ESI-MS	electrospray ionization mass spectrometry
eV	electron volt
EWG	electron-withdrawing group
f	oscillator strength constant
Fc	Ferrocene
FF	fill factor
FTO	Fluorine-doped tin oxide
GS	ground-state

h	hour
HOMO	highest occupied molecular orbital
HRMS	high resolution mass spectrometry
<i>i</i>	current
I-V	current-voltage
<i>IPCE</i>	incident photon to current efficiency
IR	infrared
ITO	indium tin oxide
J	Joule
<i>J-V</i>	current density-voltage
J_{\max}	current density at the maximum power point
J_{SC}	short-circuit current density
k	rate constant
k_1	rate constant for electron injection
k_2	rate constant for dye regeneration
k_3	rate constant for electron transport
k_4	rate constant for interfacial recombination
L	litre
LANL2DZ	Los Alamos Nation Laboratory 2-double-z
LUMO	lowest unoccupied molecular orbital
LYP	Lee-Yang-Parr functional
M	molar
m	Multiplet (NMR)

m	number of protons
m/z	mass to charge ratio
MALDI-TOF	matrix-assisted laser desorption ionization time of flight
MLCT	metal-to-ligand charge transfer
mmol	millimole
mol	mole
MS	mass spectrometry
MW	molecular weight
n	number of electrons
NHC	N-heterocyclic carbene
NHE	normal hydrogen electrode
NMR	nuclear magnetic resonance
pbpy	6-phenyl-2,2'-bipyridine
PCE	power conversion efficiency
PCET	proton-coupled electron transfer
PCM	polarizable continuum model
Pi	phosphate buffer
P_{in}	incident power of illumination
P_{max}	maximum power point
ppm	parts per million
PV	photovoltaic
r.t	room temperature
S	sensitizer

s	singlet (NMR)
S*	excited sensitizer
sat.	saturated
SiO ₂	silica
t	triplet (NMR)
T	temperature
t _{2g}	metal orbitals in a (pseudo)octahedral geometry with π symmetry
TD-DFT	time dependent density functional theory
terpy	2,2':6',2''-terpyridine
terpy-R ₁	2,2':6',2''-terpyridine -4'-substitue derivative
TOF	turnover frequency
terpy-CO ₂ Me	2,2':6',2''-terpyridine-4'-carboxylic acid, methyl ester
terpy-furyl	2,2':6',2''-terpyridine-4'-furyl
TWh	terawatt hour
UV- <i>vis</i>	ultraviolet-visible
V _{max}	voltage at maximum power point
V _{OC}	open-circuit voltage
Γ	dye loading
δ	chemical shift
Δ	difference
ε	molar extinction coefficient
λ	wavelength
λ_{em}	emission maximum

λ_{ex}	excitation wavelength
λ_{max}	absorption maximum
π	a bond or interaction with orbitals containing a nodal plane
σ	a bond or interaction with orbitals containing a nodal plane
τ	excited state lifetime
Φ	quantum yield
χ^2	chi-squared value (error determination)
Ω	resistance (ohms)

Epigraph

“When you have an established scientific emergent truth, it is true, whether or not you believe in it.” - Neil deGrasse Tyson

Chapter 1 : Introduction

1.1.Motivation: Solar Energy Generation and Storage, Climate Change and Sustainability

The 21st century has seen an unprecedented level of globalization and economic integration.¹⁻³ Economies of the world are inherently intertwined through business and growth, while still adversely racing to divide the necessary finite resources to maintain growth. One of the most conflict-prone issues is energy generation and security, mainly in the form of fossil fuels.^{4,5} This is a non-renewable energy source, meaning that once consumed it is depleted. The issue of climate change related to the burning of fossil fuels has divided opinions of mitigation strategies.⁶ The science of global heating due to the presence of gases that absorb heat is beyond question, but due to the natural oscillation and inherent unpredictability of weather patterns some are left unconvinced that we are entering a period of human driven global warming versus a natural heating cycle of the earth.⁷ Regardless of climate change, the argument of sustainability for energy product and generation is irrefutable and perhaps a more unifying argument for change.^{8,9} Future generations will eventually be left with a world void of easily accessible fossil fuels and this will require strategies to find alternatives. Currently, about 75% of fossil fuels are used in the production of electricity and this accounts for 66% of total power generation in the U.S (Figure 1.1). Global electricity generation is about 67% based on fossil fuels. Current targets for U.S electricity generation until 2035 are: coal 39%, natural gas 27%, nuclear 18%, renewable energy 16%, and oil and other liquids 1%.^{10,11}

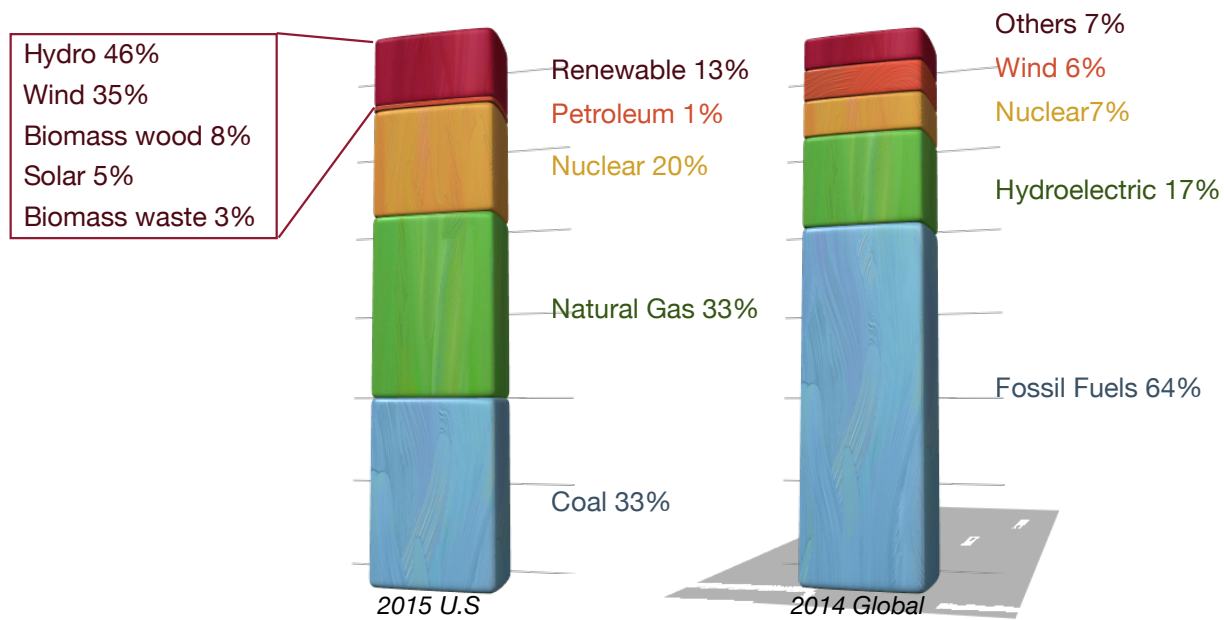


Figure 1.1. Electricity generation in U.S in 2015 and Global 2014. Note sum of components do not equal 100% due to independent rounding.^{11,12}

Addressing power generation using renewable and/or green energy sources would lead to a dramatic change in the global consumption of fossil fuels. Renewable or green energy sources are energy sources that have an inexhaustible energy source or with low or net zero CO₂ production intensity.^{13,14} Sources that would be classified in these categories are wind, tidal, hydro, thermal, solar and nuclear (although nuclear is not inexhaustible it is considered green for lack of CO₂ production). It is broadly accepted that the solution to energy generation sustainability will require a combination of various technologies.¹⁵⁻¹⁷ Renewable energy generation already accounts for 13% of U.S electricity production and is expect to be one of the largest growing sectors over the next century.¹⁴ A shortcoming of most renewable energy sources is availability. For instance, it makes little sense to build a wind turbine in a place where the

wind does not blow strongly. Perhaps a less obvious limitation is the infrastructure consideration in transporting the energy from the source to the consumer.¹⁸ Modern day transmission lines contribute to a ~5% loss in efficiency and unless you have access to a grid, in many cases the intermittency is unacceptable to replace fossil fuel based sources.¹⁹ Some of these technologies, however, can be advantageous in that they allows energy to be produced in regions of the world where grids are not practical or accessible such as in developing nations.

In 2014, world power generation capacity was increased by 313 TWh of which 45% was due to renewables (world power generation total 22352 TWh).¹² By 2050, world power generation is expected to roughly triple.¹² In the renewable energy capacity added, roughly one-third was due to solar power generation. The sun offers a virtually unlimited energy supply (1.05×10^9 TWh) if one can convert sunlight into electrical power via the absorption of light and the subsequent utilization of the energy associated with it.²⁰ This process is known as the photovoltaic effect and was first demonstrated over 170 years ago by French physicist Becquerel when he showed a current could be produced by uneven illumination of two plates of platinum in electrolytes of different pH.²¹ To incorporate large-scale solar power generation effectively, it will need to be coupled with energy storage capacity to meet energy demands during times of low sunlight.²²

The most widely used solar technology is based on crystalline silicon (c-Si). The price of solar in recent years has declined considerably (Figure 1.2). In 2015, the price paid for long-term contracts for bulk purchase of solar electricity on average fell below 0.06 \$/kWh.^{23,24} To put this value into context, coal is 0.06 \$/kWh, hydroelectric is 0.03 \$/kWh and natural gas is 0.05 \$/kWh.²⁵

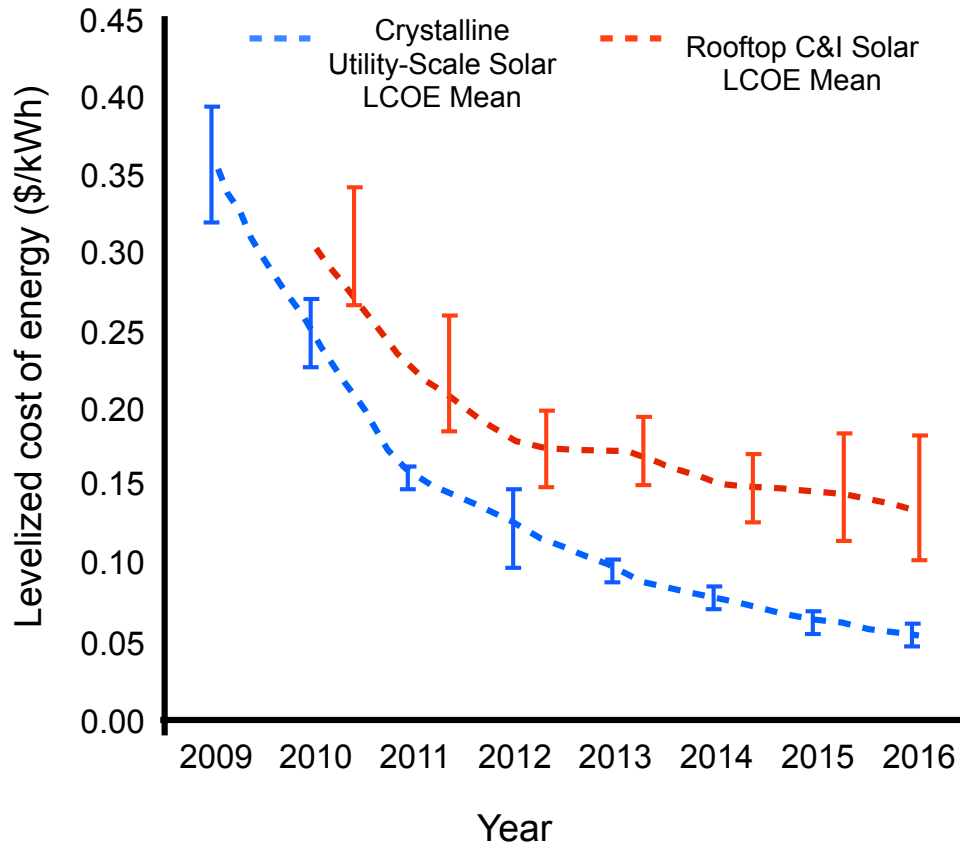


Figure 1.2. The price of installed solar in the U.S. over the last decade.²⁴

Installed power does not necessarily correlate to power output and solar based on c-Si operates at high efficiency only at times of high intensity sunlight and performs quite poorly in times of low sunlight (cloudy days). Figure 1.3 highlights the fact that c-Si cells, with a power conversion efficiency (*PCE*) of 18%, actually operate closer to 8% on a cloudy day, which corresponds to 5 mW/cm² intensity. Unfortunately, this leaves ideal locations in desert like areas often devoid of large population bases.

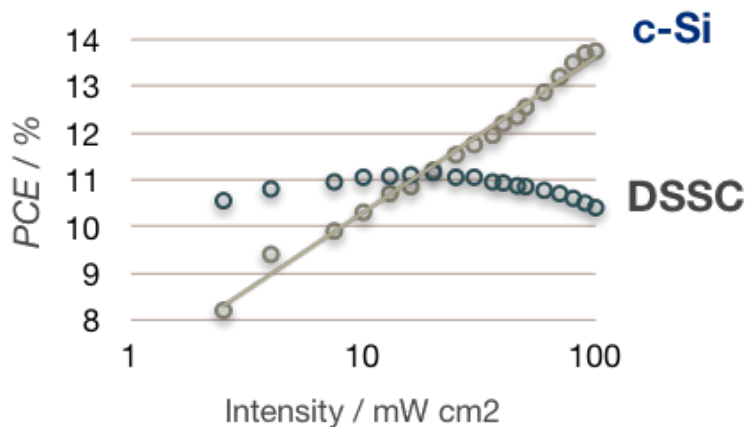


Figure 1.3. Performance comparison the DSSC and c-Si at various light intensities.

There are a myriad of solar technologies that are showing promise to garner market share as potential alternatives to the classical silicon-based solar technology. The dye-sensitized solar cell (DSSC) is a next-generation solar technology that has shown promise and is already at the commercial level.^{26,27} The DSSC far out performs c-Si based solar cells in times of low intensity sunlight, which opens the possibility for DSSC based solar in locations that have cloudier climates, which greatly enhances location accessibility as shown in Figure 1.3.²⁸

The DSSC is a photoelectrochemical cell that consists of micrometer thick mesoporous titania (TiO₂) semiconductor grown from a conductive substrate (fluorine doped-SnO₂), a light absorbing dye and a redox mediator. The modular design allows for fine-tuning of the individual components for maximum efficiency. The archetypical DSSC was first developed by Grätzel and O'Regan, and operated at *PCE* ~ 12% in diffuse light and *PCE* ~ 7% under solar irradiation utilizing a ruthenium polypyridyl based dye **N3** (Figure 1.4).²⁹

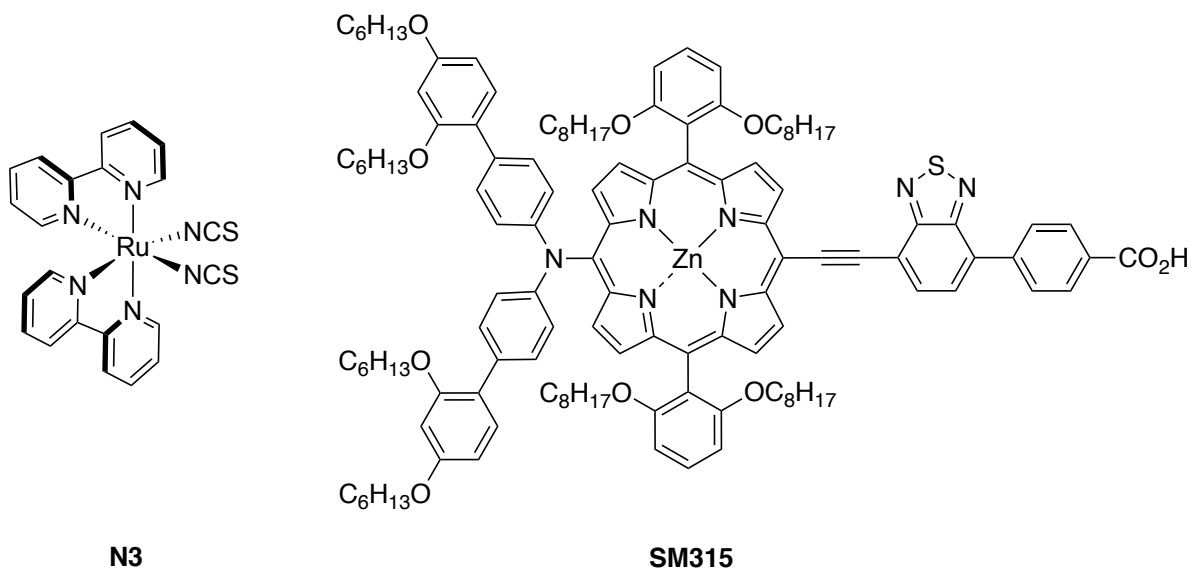


Figure 1.4. Grätzel's famous **N3** dye that was the first dye reported with a DSSC *PCE* > 5% and **SM315** that broke the *PCE* = 13% barrier.

More recently, dyes based on porphyrin (**SM315**) chemistry using alternative electrolytes have achieved *PCE* ~ 13%.³⁰ Successive generations have achieved *PCE* >14% by modification to all solid state devices, however at the sacrifice of long-term stability.^{31,32}

There are numerous energy storage approaches being employed that are divided into two fundamental groups based on potential energy and kinetic energy storage, such as pumped hydroelectric and electrochemical fuels, respectively.³³ The prospect of using solar-based electrochemical fuels for energy storage is advantageous as it allows energy output from solar in times of low sunlight. Furthermore, the energy supply is secure and sustainable with low CO₂ emission and it allows small-scale storage distribution.³³ Plants employ the concept of solar fuel all around the world. It is based on the principle of photosynthesis, where plants absorb light and convert this light into stored energy by the rearrangement of CO₂ and H₂O bonds into carbohydrates and oxygen. Central to this process is Photosystem II, which is responsible for the

electrochemical splitting of water using light as the energy input. Furthermore, the redox reaction that is at the heart of the complexity of this reversible cycle is the splitting of water into four electrons and four protons (equation 1.1). Proton reduction is trivial using platinum electrodes and occurs at 0 V (*vs* NHE) (equation 1.2).



All the above equations are pH dependent and under strongly acidic conditions (pH 0) the total cell potential is 1.23 V (*vs* NHE) (equation 1.3). H₂O offers the perfect carbon neutral fuel and has been at the heart of considerable research into energy storage for decades.^{34,35} The mechanism of water splitting will be briefly introduced in section 1.4.1, but was not investigated in this thesis.

This Chapter will briefly explain the history of the sensitization of semiconductors and the development of ruthenium complexes for electron-transfer process related to the DSSC and heterogeneous water oxidation. The photophysical and electrochemical properties of ruthenium polypyridyl complexes will be introduced, followed by the principle of operation for a system in power generation and power storage.

1.2.Sensitization of Semiconductors and Ruthenium Complexes

1.2.1 Sensitization of Metal Oxides

In the late 1960s and early 1970s, Gerischer and Tributsch investigated the sensitization of metal oxides using rhodamine B to understand the charge-injection kinetics of excited state and ground state molecules with semiconductors.^{36,37} Tributsch demonstrated the potential to maintain photon to electron conversion by using chlorophyll b-sensitized to ZnO crystals and found that currents could be prolonged by the addition of different types of reducing agents to the electrolyte solution leading to regeneration of oxidized chlorophyll molecules.^{38,39} In 1977 the sensitization of single crystals of TiO₂ by Rose Bengal was reported along with electron-injection efficiencies and the effect of dye concentration on the surface;⁴⁰ an important step in using TiO₂ as a semiconductor in conjunction with a dye. Simultaneously, research was being carried out on direct modification of electrodes with chemisorbed organic molecules.^{41,42} Further work with polymorphs anatase and rutile TiO₂ were found to have a dependency of adsorption kinetics as well as electron-injection yields when using the N3 dye.⁴³ In combination, these studies contributed to the understanding of the photoelectrochemical effects of electron transfer events at semiconductor/dye interfaces. In the application of high efficiency DSSCs the major break through occurred in 1991, when O'Regan and Grätzel demonstrated that moving from a monolayer of dyes on a flat TiO₂ surface to a mesoporous semiconducting surface the *PCE* could be greatly increased due to higher dye loading and excellent quantum efficiencies.²⁹ This was a pivotal moment in not only DSSC design, but in photoelectrode-based architectures. Ruthenium complexes anchored to titania have been explored for numerous applications and will be explained in the following section.

1.2.2 Ruthenium Complexes

Ruthenium complexes have a rich history and their development for photochemistry and photophysics based applications is well documented.⁴⁴⁻⁴⁹ Over the last several decades their study in solar-energy generation, water oxidation, and a myriad of other applications has led to several commercial products (O₂ sensors, DSSC, etc.).⁵⁰⁻⁵⁶ The archetypical compound [Ru(bpy)₃]²⁺ (bpy = 2,2'-bipyridine) with its chemical stability, redox properties, excited-state lifetimes and absorption/emission properties has attracted thousands of derivitizations of polypyridyl bi-, tri- and tetra-dentate ligand scaffolds.⁵⁷⁻⁶¹ Combinations of polypyridyl and other ligand designs have yielded even more diversity in the photophysics of these compounds giving the chemist a high level of control in molecular engineering complexes for particular applications of photochemistry, photocatalysis, electrochemistry and combinations thereof. Ru(II) complexes decorated with highly conjugated ligand scaffolds with low-lying ligand π^* orbitals yield compounds with impressive absorption properties over the visible spectrum through multiple metal-to-ligand charge transfer (MLCT) transitions that can be finely tuned with electron-donating and -accepting substituents.⁶² Excellent redox stability of the oxidized metal and reduced multidentate ligands make them ideally suited for light harvesting and energy-transfer applications where light is the desired energy input.⁶³⁻⁶⁵ Ruthenium may be considered a somewhat exotic metal for broad-scale application due to its rarity, but nonetheless it is well suited for fundamental study and is currently cost effective for some applications such as in olefin metathesis, DSSCs, as part of hardening alloys with platinum group elements for use in electrical contacts and thick-film chip resistors.⁶⁶⁻⁶⁸ Perhaps at the nexus of its interest in chemistry are the photophysical properties that will be discussed in the following section.

1.2.3 Photophysics

Ruthenium is a d^6 -transition metal that when bonded to aromatic ligand scaffolds has a highest-occupied molecular orbital (HOMO) that is dominated by metal character from non-bonding d -orbitals and lowest-unoccupied molecular orbital (LUMO) of anti-bonding character that are either metal centered or ligand centered.⁶⁹ The prototypical compounds $[\text{Ru}(\text{bpy})_3]^{2+}$ and $[\text{Ru}(\text{terpy})_2]^{2+}$ (terpy = 2,2':6',2''-terpyridine) with D_3 and C_2 symmetry, respectively, absorb light in the visible spectrum (400 – 700 nm). The most intense lowest-energy transition for $[\text{Ru}(\text{bpy})_3]^{2+}$ being a $^1\text{MLCT}$ in the 450 nm wavelength range with an extinction coefficient of $14600 \text{ M}^{-1}\text{cm}^{-1}$. Higher energy absorptions are associated with ligand centered (LC) transitions in the UV region. A simplified picture of the orbital diagram in an idealized octahedral environment is represented in Figure 1.5. The e_g orbital of σ^* character is more destabilized in the bpy ligand environment due to the stronger σ interaction. The t_{2g} is of non-bonding character and is roughly the same in both complexes. The energy spacing of e_g and π^* orbitals gives rise to the difference in emission properties.

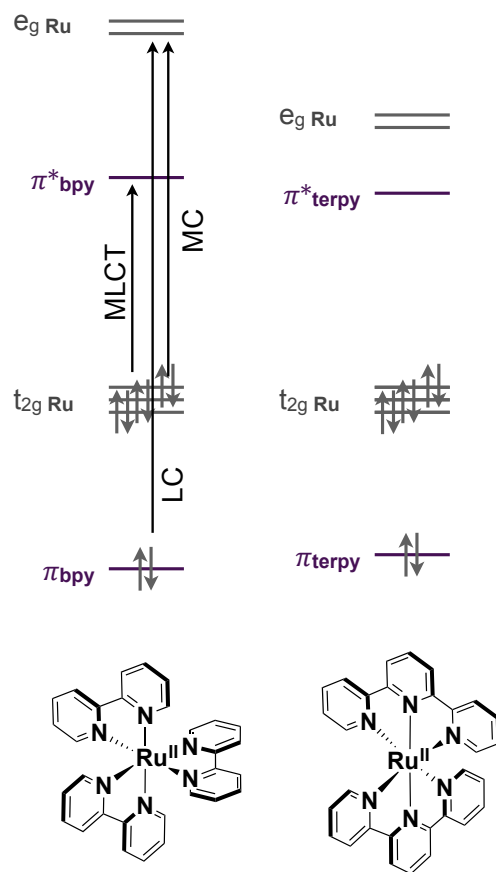


Figure 1.5. A simplified orbital diagram for $[\text{Ru}(\text{bpy})_2]^{2+}$ and $[\text{Ru}(\text{terpy})_2]^{2+}$ in an idealized octahedral environment showing relevant orbitals and transitions.

An electron that is excited (10^{-15} s) undergoes intersystem crossing (ISC $\sim 75 \times 10^{-15}$ s) quantitatively from the $^1\text{MLCT}$ to the $^3\text{MLCT}$ state due to strong spin-orbit coupling, which either undergoes radiative (phosphorescence) or non-radiative decay with lifetimes governed by their rates k_r and k_{nr} respectively.⁷⁰ The deactivating metal-centered (^3MC) is non-emissive and can be thermally accessible from the $^3\text{MLCT}$ state (Figure 1.6). Ligand field theory implies that the less idealized octahedral binding geometry around ruthenium leads to a weaker ligand field strength, which results in a smaller energy spacing between the metal orbitals and the π^* orbitals

for the tridentate ligand scaffold and consequently renders $[\text{Ru}(\text{terpy})_2]^{2+}$ non-emissive or weakly emissive with short excited state lifetimes in the picosecond time regime (10^{-12} s).⁴⁷

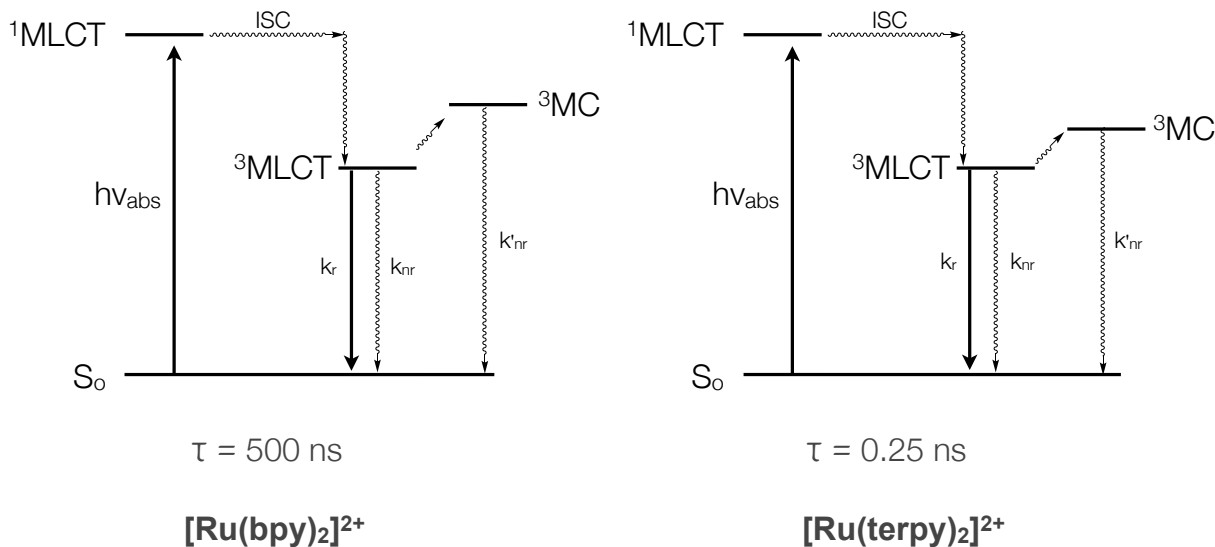


Figure 1.6. Energy diagram illustrating the thermal accessibility of the ^3MC state in $[\text{Ru}(\text{terpy})_2]^{2+}$.

Much attention has been focused on increasing the emission lifetimes and quantum yields of $[\text{Ru}(\text{terpy})_2]^{2+}$ and bistridentate-type derivatives as they afford a more simplistic synthetic protocol with the elimination of *fac* and *mer* isomers rendered by the *trisbidentate* ligand environment.^{58,71-73} One strategy to improve the lifetimes of these complexes has been demonstrated by Hammarström *et al.* using ligands that afford a more idealized octahedral binding geometry, which raises the deactivating ^3MC state, such as the approach shown in Figure 1.7 $[\text{Ru}(\text{dqp})_2]^{2+}$ (dqp = 2,6-di(8'-quinolinyl)pyridine) which exhibited an excited-state lifetime of 3.0 μs improving on $[\text{Ru}(\text{terpy})_2]^{2+}$ by 4 orders of magnitude.⁷⁴ Another approach is to use ligands that increase the energy gap between the ^3MC and $^3\text{MLCT}$ state by installation of strongly σ - and π -accepting auxiliary ligands such as the work by Chung *et al.* with

$[\text{Ru}(\text{terpy})(\text{pbpy})]^+$ (pbpy = 6-phenyl-2,2'-bipyridine) which rendered a 10 ns lifetime, an improvement of 2 orders of magnitude over $[\text{Ru}(\text{terpy})_2]^{2+}$. Utilizing stronger donating ligands has limitations as it begins to lead to lower lifetimes by virtue of the energy gap law.^{62,75} The energy-gap law dictates that as two states approach each other in energy the rate of non-radiative decay increases.

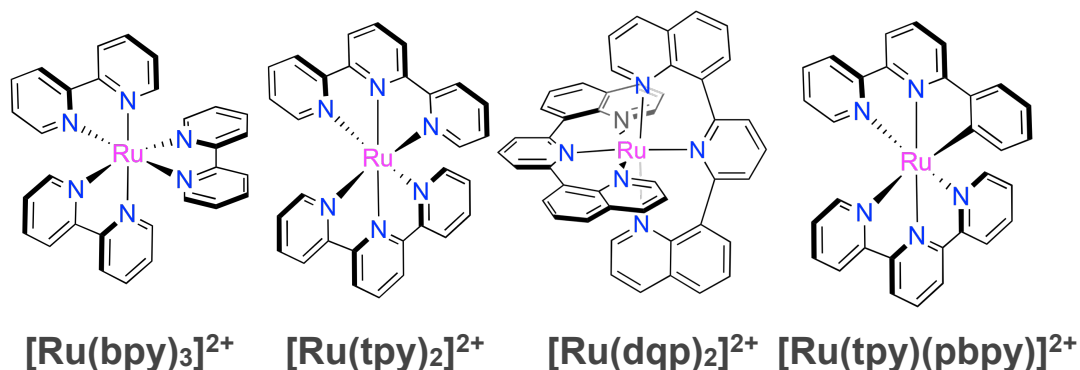


Figure 1.7. Selected ruthenium polypyridyl compounds for discussion of excited-state lifetimes.

There have been numerous approaches to prolonging the excited-state lifetimes using strongly donating carbanion ligands through cyclometalation to using anionic N-heterocycles and N-heterocyclic carbenes (NHCs).⁷⁶⁻⁷⁹ Most suffer from poor excited-state lifetimes due to the aforementioned energy-gap law or a blue-shifted emission (> 100 nm for an NHC), losing practical application. Mesoionic carbene ligands offer a strongly σ -donating and moderate π -accepting ligand maintaining the $^3\text{MLCT}$ energy and increasing the spacing between the ^3MC and $^3\text{MLCT}$ states (described in Chapter 2).^{80,81} Notably, room-temperature lifetimes of >7.0 μs have been achieved.⁸¹ Strategies to enhance lifetimes using ligands equipped with a ^3LC state that act like a reservoir for so-called delayed phosphorescence are not increasing the $^3\text{MLCT}$ lifetime, but rather delaying it.⁷¹ Ruthenium complexes with long-lived excited states at room

temperature are suited to be used as electron donors, electron acceptors and/or energy transfer donors. $[\text{Ru}(\text{bpy})_3]^{2+}$ has a $^3\text{MLCT}$ state that lies 2.12 eV (in aqueous solution) higher in energy than the ground state, which is useful for energy transfer processes. This energy can be found by the lowest energy absorption in a glass matrix at 77K by direct population of the $^3\text{MLCT}$ state. Approximation of the HOMO-LUMO energy gap (E_{0-0}) can also be accomplished by normalization of the emission curve to the lowest energy MLCT absorption and taking the intersection of the curves as shown in Figure 1.8.⁴⁴ $[\text{Ru}(\text{terpy})_2]^{2+}$ has a 2.13 eV HOMO-LUMO gap, however as previously mentioned only a 0.25 ns lifetime.⁸¹ Understanding the ground state electron-transfer processes can be studied electrochemically and will be discussed in detail in the following section.

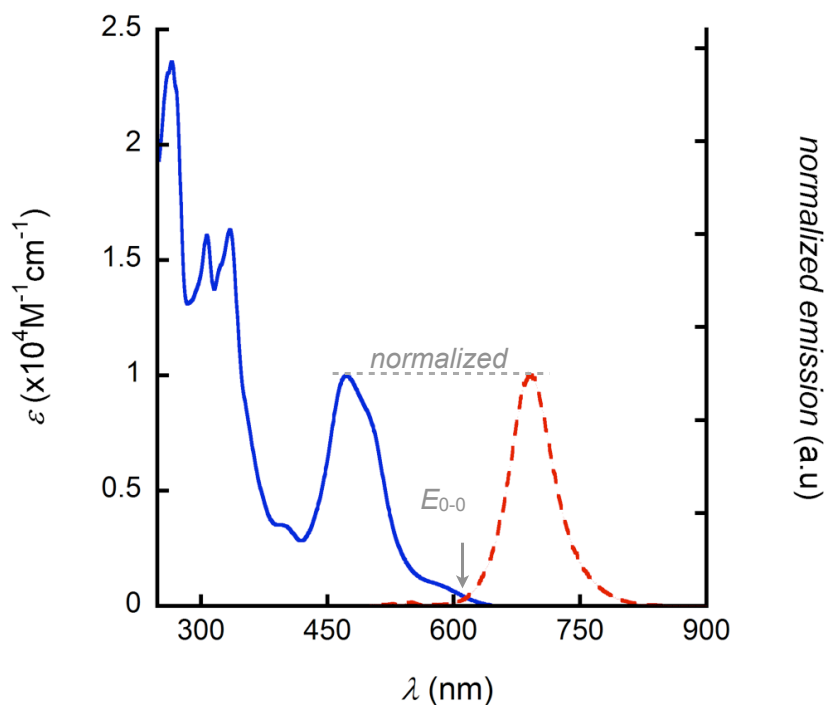


Figure 1.8. Example of determining the HOMO-LUMO energy gap (E_{0-0}) by normalization of the emission peak to the lowest major MLCT energy of the absorption spectrum.

1.2.4 Electrochemistry

Ruthenium complexes have an impressive number of applications for long-lived excited states, but the redox chemistry of ruthenium in its ground state may be of equal potential. $[\text{Ru}(\text{bpy})_3]^{2+}$ shows a reversible (III/II) redox couple at +1.50 V vs NHE and 3 reversible redox couples for the reduction for each bpy ligand (~ -1.2 V) in MeCN with all being one-electron events. Most ruthenium complexes exhibit metal-based oxidation events and ligand-based reduction events with the energy spacing dependent on the electronics of the environment. The oxidized $[\text{Ru}(\text{bpy})_3]^{3+}$ is reduced by water, but the reaction is pH dependent and can be complicated by the formation of small quantities of Ru nanoparticles.⁴⁴ The archetypical $\text{Ru}(\text{terpy})(\text{bpy})\text{Cl}$ complex in aqueous solution has been shown to undergo ligand exchange to the aqua complex and catalytically oxidize water by accessing several higher oxidation-state intermediates (Ru^{III} , Ru^{IV} , Ru^{V}).⁸² This will be described in more detail in section 1.4.1.

1.3. Power Generation: The Dye-Sensitized Solar Cell

1.3.1 Principle of Operation

The DSSC operates as a complex photoelectrochemical cell converting photons into electricity. It consists of four major parts: Anode, cathode, sensitizer and electrolyte. The anode is comprised of conducting FTO (fluorine doped tin oxide) glass onto which a mesoporous semiconductor metal oxide titania is sintered. This sintering process involves careful heat treatment (~ 500 °C) of an applied nanoparticle paste of titania (nanoparticles ~ 20 nm in diameter), which insures conductivity of the nanoparticle film while maintaining porosity. This paste is typically applied by doctor blading or screen printing and tuned for a desired thickness. Post treatment of the film is carried out by submersion in aqueous TiCl_4 in order to improve connectivity. The titania is a wide band-gap (3.2 eV) semiconductor and absorbs mostly in the

UV region $<385\text{ nm}$.⁸³ A wide band gap is required so that visible light can be absorbed by the sensitizer. Absorption of light by the titania would result in a hole which would short-circuit the cell. In high-performance cells, the titania can be comprised of several layers of different sized nanoparticle films to improve efficiency. Large nanoparticle films ($\sim 400\text{ nm}$) act to trap the incident light within the cell by scattering it and increasing the path length, which improves the odds of a dye absorbing the photon.^{84,85} Other titania morphologies have been investigated but are beyond the scope of this thesis.

The titania is coated with a visible light-absorbing dye or sensitizer (Figure 1.9). The sensitizer is covalently linked to the TiO_2 surface through anchoring groups. These anchoring groups are acids that undergo hydrolysis in the linking with the TiO_2 and are typically $-\text{CO}_2\text{H}$, $-\text{PO}_3\text{H}_2$ or $-\text{cyanoacetic acid}$. The anchoring groups supply a path for electron injection into the semiconductor. Dye molecules are usually dip-coated onto the titania. There are a plethora of dye designs, but most have the following basic elements. First, they must have a lowest excited state negatively shifted relative to the conduction band of the TiO_2 at $\sim 0.5\text{ V vs NHE}$ to allow for charge injection. Second, the dye must have a HOMO positively shifted from the redox couple within the electrolyte $\sim +0.78\text{ V}$. Third, the dye should be photochemically stable and absorb as much of the visible and near IR spectrum as possible.

The electrolyte is filled into the porous device and sealed with a platinum coated counter electrode (cathode). The electrolyte consists of a redox couple iodide/triiodide (I^-/I_3^-) and a other components such as 4-*tert*-butylpyridine that passivates the incompletely coordinated Ti atoms, LiI concentration to adjust the conduction band which are used to affect cell performance in MeCN.⁸⁶ DSSC designs that involve all solid-state devices and different redox mediators have been investigated with some success.^{30,87-90} The electrolyte is a major path of degradation in

these devices as the corrosive solvent can wreak havoc on the sealants used to hold the two pieces of conducting glass together. Long-term stability studies have showed that water eventually seeps into the devices through the degradation of the sealant and causes dye hydrolysis and efficiency losses.

The conventional cell operates by a photo-induced charge separation at the dye-sensitized interface between an electrolyte and the aforementioned semiconducting metal oxide (e.g. TiO_2) as shown in Figure 1.8. Upon absorption of a photon by a dye molecule, an electron is promoted from the ground state (S) to the excited state (S^*). From the excited state the electron is injected into the conduction band of the semiconductor ($k_1 = 10^{11} - 10^{13} \text{ s}^{-1}$). For efficiently designed dyes, the injection yield is approximately unity even for compounds with emission lifetimes on the nanosecond timescale. Once the electron is injected into the semiconductor, the electron percolates through the semiconductor to the conducting glass ($k_3 = 10^0 - 10^3 \text{ s}^{-1}$) where it travels around a circuit to do useful work before returning to the platinized counter electrode. At the platinized electrode, the electrolyte becomes reduced and transfers an electron to the oxidized dye, a process known as regeneration ($k_2 = 10^5 \text{ s}^{-1}$).⁹¹ Interfacial recombination ($k_4 = 10^0 - 10^3 \text{ s}^{-1}$) between injected electrons and I_3^- is competitive with charge collection at the electrode and is addressed by passivation of the TiO_2 layer, as previously discussed, to sterically hinder the interaction between the electrolyte and TiO_2 . The dyes are archetypically ruthenium polypyridyl complexes.

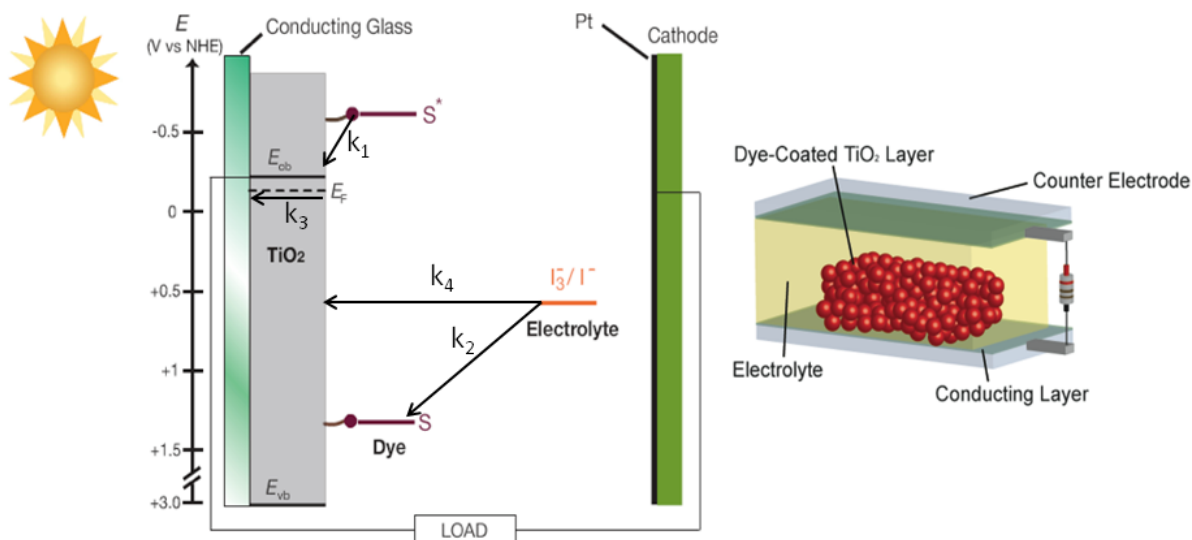


Figure 1.9. Dye-sensitized solar cell schematic and relevant energy levels for a dye ($S = \text{HOMO}/S^* = \text{lowest excited state}$) in a working device. Rate constants shown for electron injection (k_1), dye regeneration (k_2), electron transport (k_3) and interfacial recombination (k_4).

The solar cell efficiency is related to the kinetic rate of all the competing processes within the solar cell. The thermodynamic driving force for charge injection is determined by the difference in energy between the excited state of the dye and the Fermi level of the semiconductor. The exact position of the Fermi level (E_f ; Figure 1.9) depends on the equilibrium established between the dye and electrolyte at the surface of the semiconductor. The driving force for regeneration of the oxidized dye, is approximated as the difference in energy between the redox couple in the electrolyte and the highest occupied molecular orbital (HOMO; S) of the dye. When using the conventional iodide/triiodide redox couple, there is a complex series of redox reactions to consider, making the exact energy of the electrolyte difficult to determine precisely. Recent research progress has discerned the important redox reaction for dye regeneration in the DSSC as the oxidation of iodide to form an iodine radical anion (+0.79 V vs

NHE) and is the important metric to consider in engineering the HOMO for dye regeneration, however the Γ/I_3^- couple governs the maximum open circuit voltage (V_{OC}) as described in this next section.^{92,93}

1.3.2 Characterization Methods

1.3.2.1 Current Density-Voltage Measurements (J - V curves)

The fundamental performance characterization method for a solar cell is a current-voltage measurement. A solar simulator instrument projects light, mimicking the solar spectrum, while applying different bias voltages and recording the current. The applied voltage generates a current equal to the photo-induced current and results in an I - V curve. The curve can then be normalized using the active area of the material to determine the current-density-voltage curve (J - V) as demonstrated in Figure 1.10. From this curve the short-circuit photocurrent density (J_{SC}), open circuit voltage, fill factor (FF) and power conversion efficiency (PCE) can be determined.⁹⁴ The J_{SC} is the y-intercept of the curve in Figure 1.10. This value is associated with the efficiency of photon absorption, charge injection/collection, negative charge recombination and dye regeneration.⁹⁵ The V_{OC} is the x-intercept of the J - V curve and is similarly dependent on a number of factors including the Fermi level and redox couple. V_{OC} has a maximum attainable value related to the E_f (-0.5 V) and the redox potential of the Γ/I_3^- redox couple (+0.4 V) of about 0.9 V. The FF is calculated by equation 1.4 and is related to the quality of the overall device and usually reported to have values between 0.6-0.8 for DSSCs with a maximum theoretical value of 1. The value is the ratio between the maximum power output ($V_{max} \times J_{max}$) and the actual power output ($V_{OC} \times J_{SC}$).

$$FF = \frac{V_{max} \times J_{max}}{V_{OC} \times J_{SC}} = \frac{P_{max}}{V_{OC} \times J_{SC}} \quad (1.4)$$

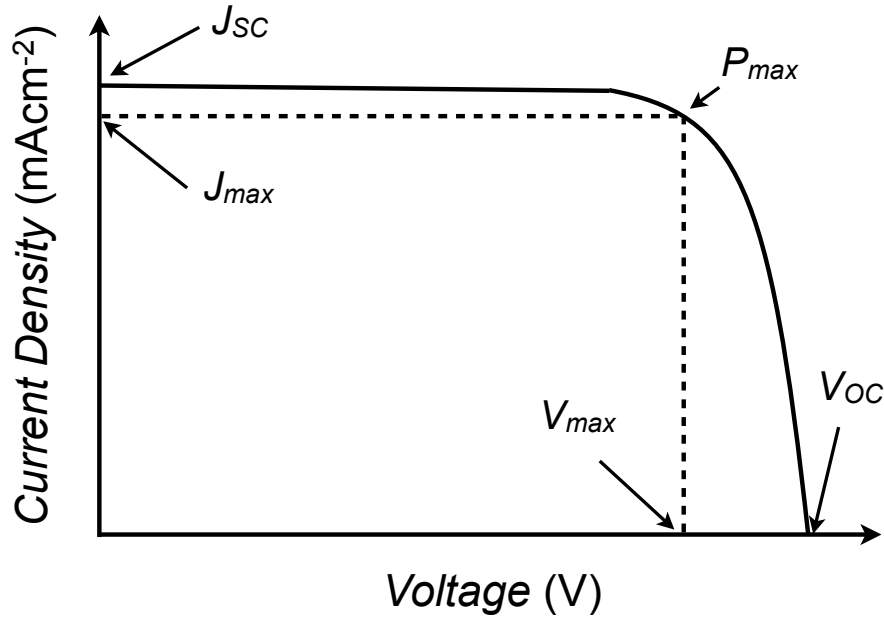


Figure 1.10. Representative photocurrent density-voltage curve and relevant performance metrics identified.

The *PCE* is the ratio of the maximum power generated (P_{max}) to the incident power input. The input power has a standard condition of AM1.5, which is a power density of 1000 Wm^{-2} at 298 K.

$$PCE = \frac{P_{max}}{P_{in}} = \frac{FF \times J_{SC} \times V_{OC}}{P_{in}} \quad (1.5)$$

1.3.2.2 Incident Photon-to-Current Conversion Efficiency (*IPCE*)

Measuring the number of electrons generated relative to incident monochromated photons yields the *IPCE*. Losses associated with scattering and reflection contribute to this

number never reaching 100%.⁹⁶ Ideally, the integrated *IPCE* curve should correspond to the J_{SC} .⁹⁴ The *IPCE* curve is a useful tool in comparing dyes and determining what absorptions are responsible for the highest current generation (MLCT, LC, etc.). Maximizing the *IPCE* over the visible spectrum and into the near-IR is necessary for high-efficiency dyes. Understanding the binding geometry of the dye to the titania also gives insight into the effectiveness of the dye design. Equation 1.6 describes the relation where h is planck's constant and c is the speed of light.

$$IPCE = \frac{h \times c \times J_{SC}}{P_{in} \times \lambda(nm)} \times 100\% \quad (1.6)$$

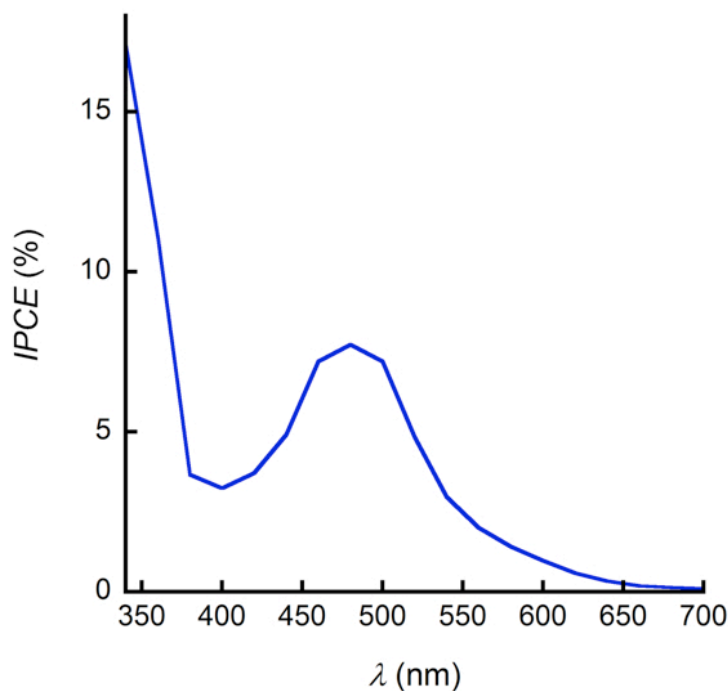


Figure 1.11. Representative *IPCE* curve for illustrating the fraction of incident light that is converted into electricity.

1.3.2.3 Diffuse Reflectance Infrared Fourier Transform (DRIFTS)

The nature of the anchoring geometry and surface attachment of the ruthenium complex with the semiconductor is important in ascertaining the binding effectiveness. DRIFTS experiments of the free complex and once bound to the surface shows the absence of the stretching frequencies of the –OH and =O anchoring oxygens as evidence of binding.⁹⁷ This method is useful when designing molecules with multiple anchoring groups in determining the binding orientation of the dye monolayer. Anchoring groups ($-\text{CO}^{2-}$ and $-\text{PO}_3^{2-}$) with possible mono-, bi- and tridentate bridging oxygens have potentially multiple binding geometries which can affect which anchoring groups are bound and unbound.

1.4. Power Storage: Molecular Heterogeneous Water Oxidation

1.4.1 Principle of Operation

Ruthenium complexes have demonstrated robust electrochemical properties and have been well studied in water splitting.⁹⁸⁻¹⁰⁰ Mechanistic studies of molecular ruthenium complexes for water oxidation is a vast field^{98,100,101} and usually involves a sacrificial oxidant such as cerium, which can further complicate the mechanism if the source is cerium nitrate.¹⁰² Nonetheless, a proposed mechanism developed by Meyer is shown in Figure 1.12.^{103,104} The important steps for ruthenium-based water oxidation are the accessibility of the Ru^{V} oxidation state and sufficient electrophilicity of the $\text{Ru}^{\text{V}}=\text{O}$ oxo-intermediate to nucleophilic attack by water.

There is an extensive library of molecular ruthenium complexes that undergo water oxidation with impressive activity and tunability; however their major drawback is their limited industrial processability in solution in regards to separation of catalyst from solution as well as long-term catalyst stability to decomposition. Heterogenization strategies for molecular catalysts on electrode surfaces has been sought to overcome this stability issue.^{103,105-108} One shortcoming of this strategy is the necessity for the catalyst anchoring ligands to be oxidatively stable and remain bound during catalysis. Titania-covered FTO glass has been successfully employed as a substrate for heterogeneous molecular water oxidation. This type of system is tested in a three electrode cell consists of working electrode, reference electrode and counter electrode. The dye-coated titania substrate acts as the working electrode where the potential is controlled and the setup is illustrated in Figure 1.13.

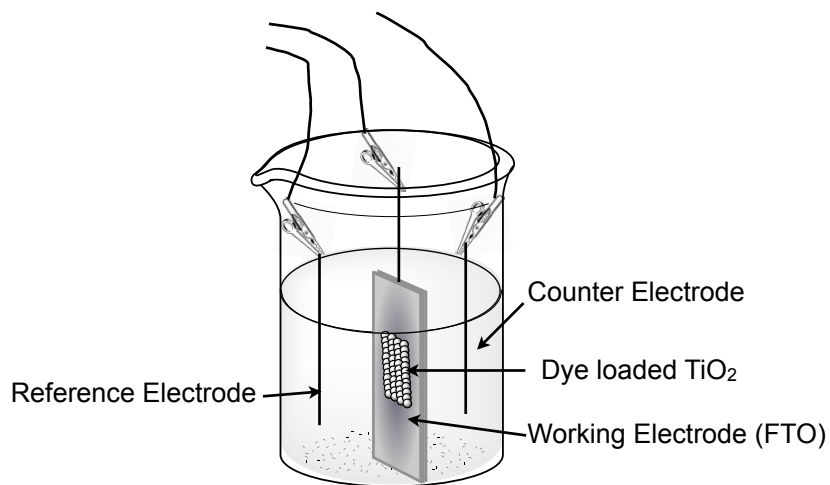


Figure 1.13. Three-electrode setup for heterogeneous water oxidation study. Electrodes are connected to potentiostat by soldered alligator clips. Reference electrode is silver wire, working electrode is FTO glass with titania covered in molecular catalyst and the counter electrode is platinum.

1.4.2 Characterization Methods

1.4.2.1 Catalysis

The catalyst efficacy for water oxidation can be tested under a variety of pHs. The mechanism also changes based on the pH and is described by the Pourbaix diagram shown in Figure 1.14.¹⁰⁹⁻¹¹¹ Thermodynamics of proton-coupled electron-transfer (PCET) reactions are typically described using a Pourbaix diagram.¹¹² These diagrams depict the equilibrium species under variable pH and can be determined using cyclic voltammetry (CV). The sloped lines correspond to the Nernstian relation with pH dependent PCET redox processes and the horizontal lines are pH independent electron transfer processes. The Nernst equation,^{113,114} where m is the number of protons, n is the number of electrons, E is the potential of interest, E^0 is the cell potential at standard condition is given by equation 1.7 at 25°C:

$$E = E^0 - 0.059 \left(\frac{m}{n} \right) \quad (1.7)$$

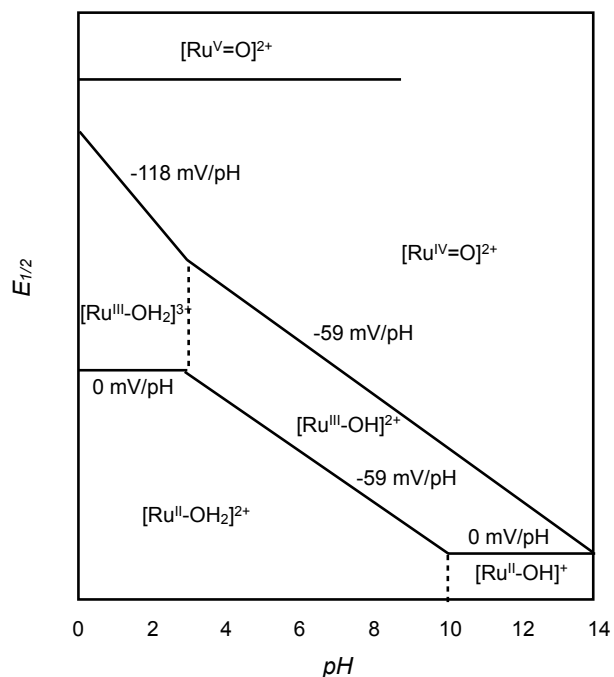


Figure 1.14. $E_{1/2}$ vs pH a typical Pourbaix diagram for a $[\text{Ru}^{\text{II}}-\text{OH}_2]^{2+}$ complex.

Only pH 4 was examined in regard to heterogeneous molecular water oxidation, which indicates that two PCET events followed by ET should be the mechanism of water oxidation. Preparation of the catalyst-loaded titania FTO glass is done by dip coating in a mM alcohol solution of the acid linker dye. Saturation coverage of the mesoporous titania can be monitored by the area under the cyclic voltammetric wave for the Ru(III/II) couple, which occurs within a few hours of dip coating. Saturation can be insured by leaving the titania substrate in the dipping solution overnight. The surface loading on the electrode in mol/cm² can be calculated from the UV-vis measurements using the expression shown in equation 1.8:

$$\Gamma = \frac{A(\lambda)}{10^3 \varepsilon(\lambda)} \quad (1.8)$$

Where $\varepsilon(\lambda)$ is the molar absorptivity at wavelength λ and $A(\lambda)$ is the film absorbance.¹¹⁵ The $\varepsilon(\lambda)$ is the value taken from the catalyst in solution. The TiO₂ substrate acts as the working electrode where the applied potential can be used to induce changes in the oxidation state of the ruthenium catalyst and monitor for the presence of catalytic water oxidation. Catalytic water oxidation is tested for by observation of a sharp increase in the current in the cyclic voltammogram (CV) taken in the presence of water.¹⁰¹ This increase must register before the oxidation of water by the electrode itself to be considered water oxidation by the molecular catalyst. The Ru(III/II) and Ru(IV/III) couples are pH-dependent as stated above. The Ru(IV/III) couple is kinetically inhibited at low pH as a result of the proton demands of the couple (Ru^{IV}=O²⁺/ Ru^{III}-OH²⁺).¹¹⁶ Direct one-electron oxidation is inaccessible due to the high potential (Ru^{IV}=OH³⁺/ Ru^{III}-OH²⁺). The mechanism proceeds through disproportionation of 2 Ru^{III}-OH²⁺ to Ru^{II}-OH₂²⁺ and Ru^{IV}=O²⁺.^{117,118} One can observe the couple at high pH or slow scan rates, thus the Ru(IV/III) couple is not observed at pH 4.

The fundamental metrics used in catalytic water oxidation to compare catalysts are turnover frequency (TOF), turnover number (TON) and the overpotential applied. The overpotential is the difference in the potential between the thermodynamically determined reduction potential and experimentally observed. The catalytic peak current can be measured at various surface coverages and if it varies linearly, it suggests a single-site mechanism for water oxidation. A rate-limiting step prior to electron transfer to the electrode can be determined by the scan-rate-normalized catalytic peak current (i / \bar{v}) that increases with decreasing scan-rate. A square root relation implies a diffusion-limiting mechanism, whereas a linear relation implies rate-limiting step before electron transfer i.e., O-O bond formation.^{104,113} By holding the potential at the catalytic peak current, sustained electrocatalytic water oxidation can be achieved. The current density can be determined by dividing the surface area by the asymptotic current from the current vs time curve and finally the TOF can then be calculated from the moles of catalyst determined photometrically and the current density determined electrochemically.

1.5. Thesis Objectives and Goals

Mesoionic carbene ruthenium complexes offer a new molecular scaffold for the DSSC to improve device efficiency by retarding dye dissociation from the surface through cooperative binding. The first series of complexes synthesized and characterized led to a serendipitous discovery that this ligand environment provided a bistridentate ruthenium complex bearing a terpy fragment with long room-temperature excited-state emission lifetime. Chapter 2 details the investigation into the photophysical properties of these types of complexes and the origin of the long-lived excited state emission lifetimes. Decorating ligand scaffolds with electron-withdrawing and electron-donating groups show a strong affect on the lifetime of these

complexes. A crystal structure obtained for these complexes reveal they indeed would be ideal for a complex that anchors through both tridentate ligands to a semiconductor surface. Chapter 3 studies the opportunity to use a combination of anchoring groups that would facilitate stronger binding and good electronic communication to TiO_2 . A major degradation of DSSC devices is the desorption of dye molecules from the surface, but strategies to improve binding affinity is often at the expense of electron-injection efficiency. Synthesizing a series of molecules with different combinations of the phosphonate anchoring group for strong binding and the carboxylate anchoring group for better electronic communication revealed our intended design. Chapter 4 details the studies of using this strongly anchored molecular platform for water oxidation. The principle of cooperative binding is employed in a strategy of heterogenization for the homogeneous catalyst with TiO_2 as a proof-of-principle to improve the stability of these water oxidation catalysts.

Chapter 2 : Long-lived excited-states of Metal-to-ligand charge transfer

2.1. Introduction

Ruthenium polypyridyl complexes have garnered considerable research attention due to a diversity of applications based on their tuneable photophysics. Ruthenium photosensitizers with redox stability in the ground state, high quantum yields and long emission lifetimes from high-energy excited states are desirable. The prototypical *tris*bidentate compound $[\text{Ru}(\text{bpy})_3]^{2+}$ (bpy= 2,2'-bipyridine) motivated an effort to engineer further compounds to understand structure/character relationships. These pyridine scaffolds can involve mono-, bi-, tri- and even tetradentate ligand scaffolds that can be molecularly engineered for specific requirements. The excited state has the ability undergo photochemical reactions if the lifetime is sufficient for electron transfer to occur before relaxation. The excited state of interest is a triplet metal-to-ligand charge transfer state ($^3\text{MLCT}$). This requirement advanced a plethora of research towards the development of long-lived $^3\text{MLCT}$ states in ruthenium compounds. Most long-lived ruthenium polypyridyl complexes are based on *tris*bidentate ligands that afford a more idealized octahedral geometry around the metal centre, which renders the deactivating triplet metal centered state (^3MC) thermally inaccessible. Chapter 2 is based on my efforts towards increasing the $^3\text{MLCT}$ lifetime in more synthetically accessible ruthenium *bis*tridentate scaffolds and the work was published in *The Journal of the American Chemical Society* (*J. Am. Chem. Soc.*, **2012**, *134*, 12354–12357).⁸¹ I was the first author on this paper and completed the initial synthesis of most of the compounds and all the characterization. Dr. Nawaporn Sanguantrakun was instrumental in scaling up and purification of final compounds to quantities required for complete analysis. Dr. Benjamin Schulze provided the initial synthetic framework in his paper published in *Chemistry A European Journal* in 2011 (*Chem. Eur. J.*, **2011**, *17*, 5494 – 5498) and

provided insightful discussions during manuscript preparations.¹¹⁹ The numbering scheme used in Chapter 2 is the numbering system from the manuscript with addition of the Chapter designation followed by the compound number (2.#).

The conclusions from this paper were that *bistridentate* systems using mesoionic carbene ligand (2',6'-*bis*(1-(2,6-dimethyl-4-bromophenyl)-3-methyl-1,2,3-triazol-4-yl-5-idene)pyridine) in place of one of the terpy (terpy = 2,2':6',2''-terpyridine) ligands have lifetimes that are four orders of magnitude higher than the archetypical *bistridentate* [Ru(terpy)₂]²⁺. Compounds **2.3** and **2.4** demonstrated that shifting the LUMO from the terpy to the carbene ligand increases the lifetime by one order of magnitude. The carbene ligand offers a combination of strongly σ -donating and π -accepting ability, which separates the emissive ³MLCT state from the deactivating ³MC state to render emission lifetimes in ruthenium complexes up to 7.9 μ s at room temperature.

2.2. Microsecond Excited-State Lifetimes in *Bistridentate* Ruthenium-Terpyridine complexes

Douglas G. Brown,¹ Nawaporn Sanguantrakun,¹ Benjamin Schulze,² Ulrich S. Schubert,^{*2} Curtis P. Berlinguette*

2.2.1 Abstract

A heteroleptic *bistridentate* ruthenium(II) complex bearing a substituted 2,2':6',2''-terpyridine (terpy) ligand is characterized by a room temperature microsecond excited state lifetime under aerobic conditions. This observation is a consequence of the strongly σ -donating and weakly π -accepting tridentate carbene ligand, 2',6'-*bis*(1-mesityl-3-methyl-1,2,3-triazol-4-yl-5-idene)-pyridine (C[^]N[^]C), adjacent to the terpy maintaining a large separation between the

ligand field and metal-to-ligand charge transfer (MLCT) states while also preserving a large $^3\text{MLCT}$ energy. The observed lifetimes are the highest documented lifetimes for unimolecular ruthenium(II) complexes, and are four orders in magnitude higher than that associated with $[\text{Ru}(\text{terpy})_2]^{2+}$.

2.2.2 Introduction

The viability of ruthenium(II) photosensitizers in a myriad of applications (e.g., photodynamic therapy, molecular electronics, sensitization of semiconductors, artificial photosynthesis, environmental remediation) hinges on a high excited-state energy that is sufficiently long-lived to facilitate the desirable electron-/energy-transfer process or photochemical reaction.^{49,95,120-124} The coordination complex, $[\text{Ru}(\text{bpy})_3]^{2+}$ (bpy = 2,2'-bipyridine), and derivatives thereof have demonstrated remarkable utility in this regard due to redox stability in both the ground and excited states, a broad and tunable metal-to-ligand charge-transfer (MLCT) band in the visible region, and a reasonably long excited-state lifetime ($\tau = 860$ ns for $[\text{Ru}(\text{bpy})_3](\text{PF}_6)_2$ in deoxygenated MeCN) with high emission quantum yields ($\Phi = 0.062$).¹²⁰ This dynamic photophysical behavior is manifested in the lowest-lying metal-to-ligand charge transfer ($^3\text{MLCT}$) states being energetically resolved from the deactivating metal-centered (^3MC) states. Figure 2.1 shows the approximate energies of the HOMOs and LUMOs of the relevant compounds.

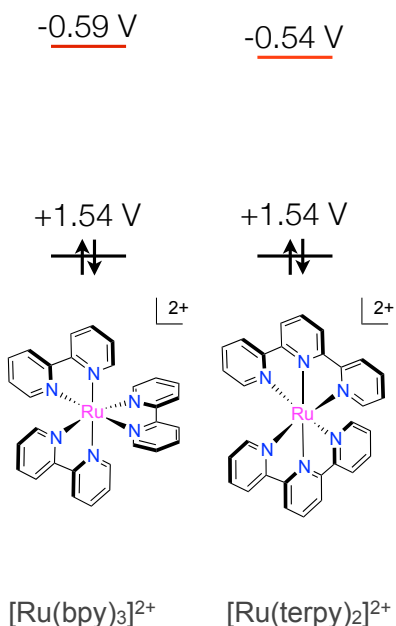


Figure 2.1 Energies (reported vs NHE) of HOMOs (black) and LUMOs (red) of benchmark complexes. The energies of the lowest excited states are approximated as $E_{1/2,\text{ox}} + E_{0-0}$. [bpy = 2,2'-bipyridine; terpy = 2,2':6',2''-terpyridine].

The related *bis*tridentate complex, $[\text{Ru}(\text{terpy})_2]^{2+}$ (terpy = 2,2':6',2''-terpyridine; Figure 2.2), benefits from many of the same properties; however, the acute bite angle of the tridentate ligand renders the radiationless deactivating ^3MC states thermally accessible thus compromising the excited-state lifetimes (e.g., $\tau = 0.25 \text{ ns}$ for $[\text{Ru}(\text{terpy})_2](\text{PF}_6)_2$).¹²¹ This outcome is unfortunate because the inherent C_2 symmetry of $[\text{Ru}(\text{terpy})_2]^{2+}$ provides many synthetic advantages in that it circumvents isomerization issues and can be easily incorporated into supramolecular assemblies through facile substitution at the 4' position of the terpy ligand to promote vectorial electron-transfer in said assemblies.^{121,125} These observations provide the

imperative to design *bistridentate* platforms with longer-lived excited-state lifetimes to, for example, render long-lived charge-separated states that can rival the photosynthetic construct.

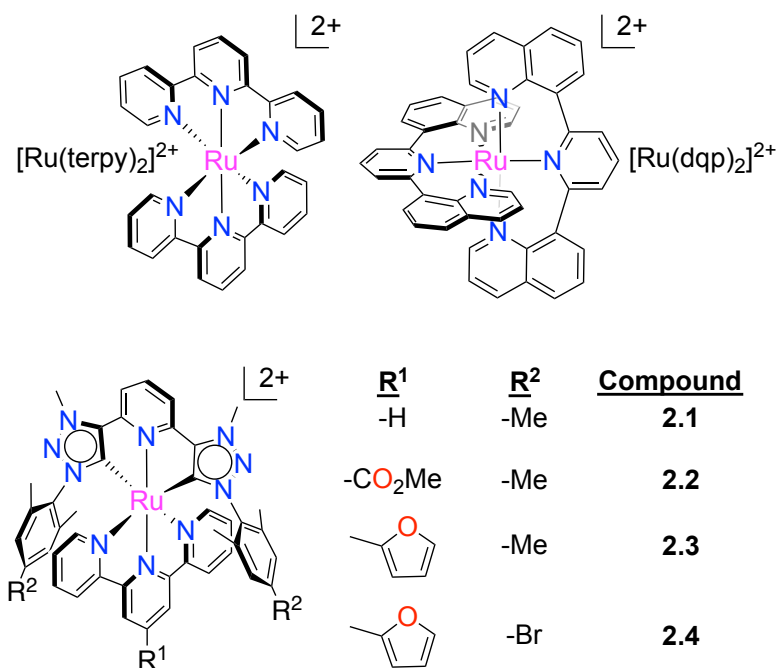


Figure 2.2. Benchmark and title Ru(II) complexes for excited-state lifetime study. (Counterion = BF₄⁻ in all cases.) Adapted with permission from *J. Am. Chem. Soc.*, 2012, *134* (30), pp 12354–12357. Copyright 2017 American Chemical Society.

One proven strategy to prolong τ for tridentate ligands is to bestow a more idealized octahedral ligand environment¹²⁶⁻¹²⁸ on the metal to increase the ligand field splitting, and thus the energy difference between ³MLCT and ³MC states. Hammarström *et al.* demonstrated the viability of this approach by showing that [Ru(dqp)₂]²⁺ (dqp = 2,6-di(8'-quinolinyl)pyridine; Figure 2.2), where the metal exists in a nearly ideal octahedral environment, exhibits an excited-

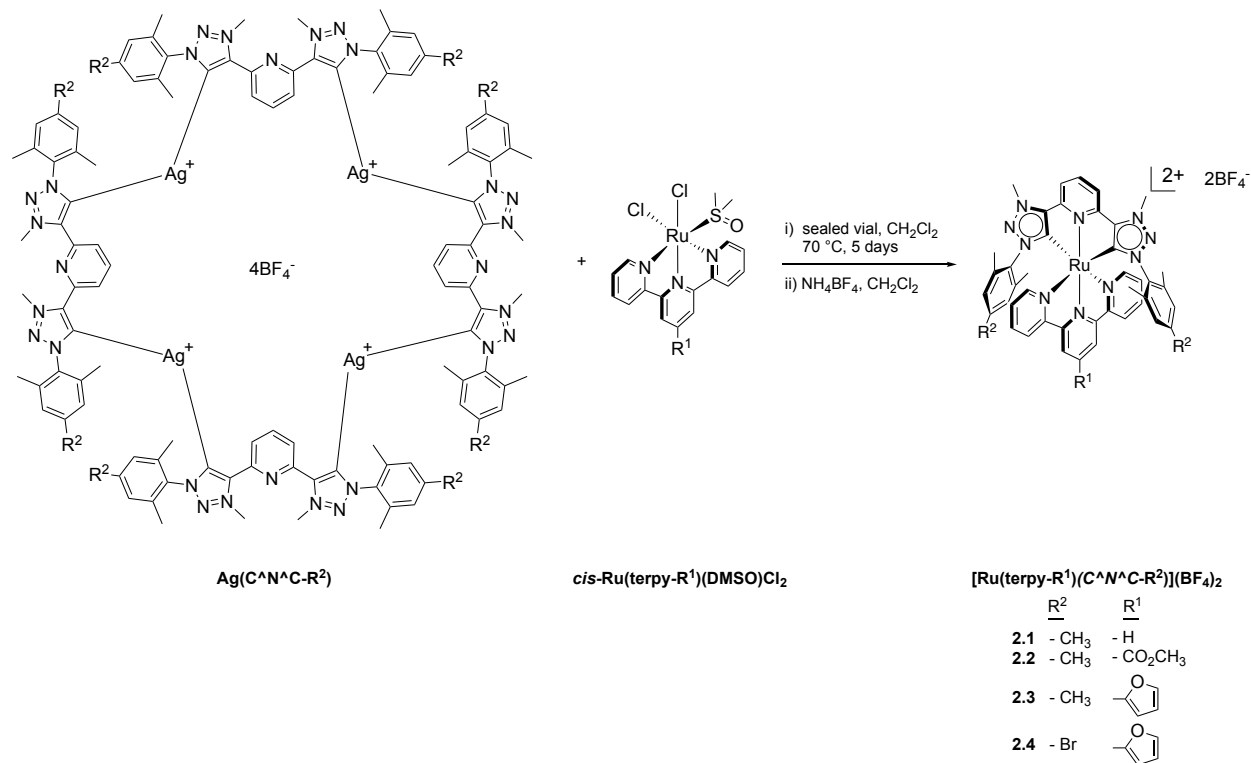
state lifetime of 3.0 μs .¹²⁹ It has since been inferred that symmetry reasons and, consequently, the extended shape of the ³MLCT potential energy surface rather than ³MC destabilization contributes to the long lifetime.¹³⁰ Although the 5.5 μs lifetime of a derivative of this complex represents the longest reported room temperature lifetime for a ³MLCT state in the literature to date,¹³¹ this type of *bistridentate* Ru(II) complex suffers from the formation of *mer* and *fac* isomers while substitution of one dqp ligand with a terpy ligand significantly diminishes the lifetime of the complex to 7.4 ns.¹²⁹ An alternative strategy is to increase the energy gap between the ³MC and ³MLCT states by placing π acceptors on the polypyridyl ligand or to install anionic, σ - and π -donating auxiliary ligands (e.g. pbpy = 6-phenyl-2,2'-bipyridine).^{62,122,132-137} While the latter approach often leads to lower lifetimes by virtue of the energy gap law^{138,139} (e.g. $\tau = 10$ ns for [Ru(terpy)(pbpy)]¹⁺^{62,140,141}), the work of Chung *et al.* demonstrated that the combination of the strong σ -donating and π -accepting character of charge-neutral *N*-heterocyclic carbene ligands can raise the energy of the ³MC state while almost maintaining the ³MLCT energy to render long-lived excited states.⁷⁸

The separation between the ³MC and ³MLCT states can be further improved by utilizing even stronger σ -donating ligands as well as auxiliary substituents. Indeed, it was recently demonstrated in one of our laboratories⁸⁰ that ruthenium(II) complexes bearing abnormal carbene ligands, such as 2',6'-*bis*(1-mesityl-3-methyl-1,2,3-triazol-4-yl-5-ylidene)pyridine tetrafluoroborate (**C[^]N[^]C**), can render a long-lived room temperature excited-state lifetime (e.g., 633 ns for **2.1**,¹¹⁹ Figure 2.2). I rationalized that further fine-tuning of the separation of the ³MC and ³MLCT states could be achieved by adding electron-withdrawing groups (EWGs) or electron-donating groups (EDGs) to the ligand scaffold to induce even longer lifetimes. Following this line of inquiry, we demonstrate herein that judicious installation of EWGs and

EDGs about both tridentate ligands affords an electronic structure that leads to the longest room-temperature $^3\text{MLCT}$ lifetime ever reported for a complex bearing a single ruthenium center.

2.2.3 Results

The title complexes were produced by the sequential coordination of the two tridentate ligands to the metal ion (synthetic details are provided in the experimental section). Compounds **2.2-2.4** were synthesized in a similar manner to that of **2.1**¹¹⁹ using mild and selective transmetalation reactions between silver-activated forms of the carbene ligands [namely, silver(I) complexes of $\text{C}^{\wedge}\text{N}^{\wedge}\text{C}$ and 2',6'-bis(1-(2,6-dimethyl-4-bromophenyl)-3-methyl-1,2,3-triazol-4-yl-5-ylene)pyridine ($\text{C}^{\wedge}\text{N}^{\wedge}\text{C}\text{-Br}$)] and *cis*-[Ru(terpy- R^2)(DMSO)Cl₂] ($\text{R}^2 = \text{-H, 2-furyl, -CO}_2\text{Me}$ positioned at the 4'-position of terpy) derivatives (Scheme 2.1). Notably, the *trans*-[Ru(terpy- R^2)(DMSO)Cl₂] derivatives were inert to reactions with said carbene precursors. The identity and purity of the dark red microcrystalline solids were verified by ^1H and ^{13}C NMR spectroscopic techniques, elemental analyses, and matrix-assisted laser desorption/ionization (MALDI) and high-resolution electrospray-ionization (HR-ESI) mass spectrometry (see experimental details).



Scheme 2.1 Transmetalation scheme for complexes **2.1-2.4**. Adapted with permission from *J. Am. Chem. Soc.*, 2012, *134* (30), pp 12354–12357. Copyright 2017 American Chemical Society.

The electrochemical behaviour of **2.1-2.4** in MeCN was examined by cyclic voltammetry (Table 2.1). Each complex exhibits a single reversible oxidation wave at *ca.* 1.2 V (all potentials reported herein are *vs* NHE) that is assigned as a Ru(III)/Ru(II) redox couple (*vide infra*). The metal-based redox couple for **2.1** was measured at 1.24 V. The -CO₂Me and -2-furyl groups positioned on the terpy ligands of **2.2** and **2.3** shift the HOMO energies to 1.31 and 1.18 V, respectively. Replacement of a methyl group belonging to each mesityl moiety of **2.3** with a bromo substituent (i.e., **2.4**) leads to a diminution of electron density on the metal thus lowering the HOMO energy to 1.22 V. Note that the halide is moderately σ -accepting and π -donating, but

the latter is suppressed by the orthogonality of the mesityl and carbene groups of the C[^]N[^]C ligand.

The trends in the first reductive waves for **2.1-2.4** indicate that the π^* systems of the terpy and C[^]N[^]C ligands of **2.1** are very close in energy. The presence of the π acceptor on the terpy ligand lowers the LUMO, which is reflected by a ligand-based reduction potential for **2.2** that is 140 mV lower than that of **2.1** (Figure 2.3). The presence of the electron-donating 2-furyl group about the terpy in **2.3**, however, produces a ligand-based reduction potential at \sim 0.84 V that is consonant with **2.1**. This observation suggests that the π^* system of the terpy ligand is higher in energy and that the LUMO resides on the carbene ligand in **2.3** and **2.4**. This arrangement of energy levels is supported by the disparities of the first reduction waves for **2.3** and **2.4**; i.e. a lower LUMO for **2.4**, where the carbene ligand features an additional acceptor (Figure 2.3).

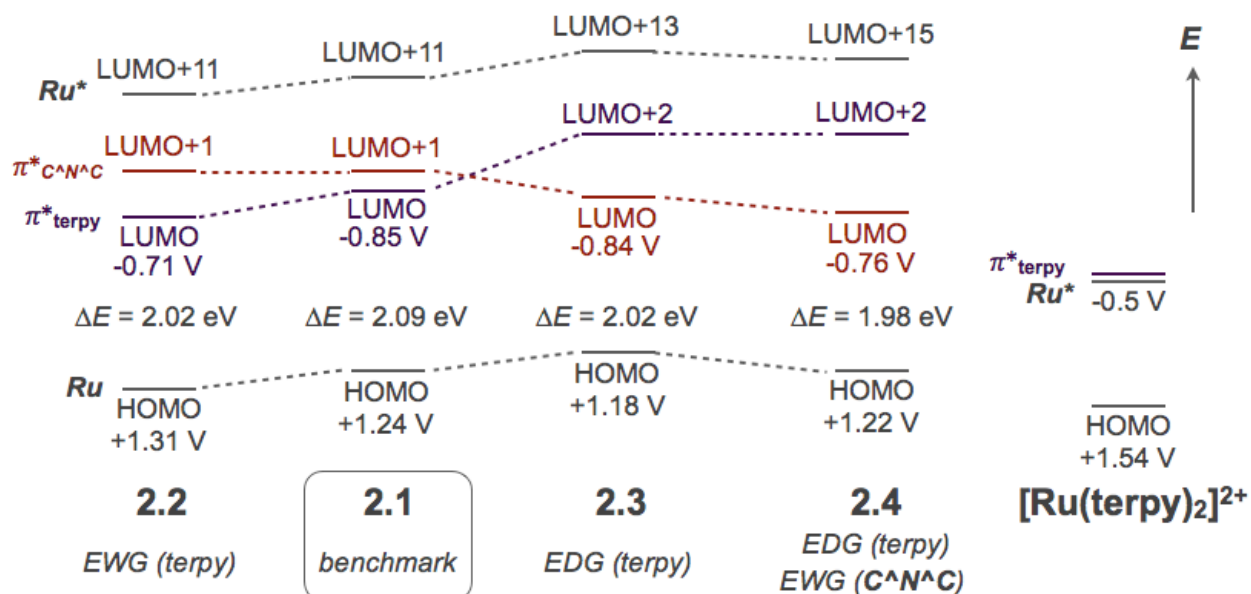


Figure 2.3. Summary of relevant energy levels for **2.1-2.4**. The HOMO and LUMO energies correspond to the ground- and excited-state oxidation potentials, respectively; the LUMO+1 and

higher levels are estimated from computational data. Data for $[\text{Ru}(\text{terpy})_2]^{2+}$ is also provided for comparison. Adapted with permission from *J. Am. Chem. Soc.*, 2012, *134* (30), pp 12354–12357. Copyright 2017 American Chemical Society.

The UV-*vis* absorption spectra of solutions of **2.2-2.4** each reveal MLCT bands centered at *ca.* 500 nm with moderate extinction coefficients (e.g., $\sim 1.0 \times 10^4 \text{ M}^{-1} \text{ cm}^{-1}$). The narrow MLCT band in the visible region for each complex is a manifestation of the C_{2v} symmetry and the nearly degenerate π^* orbitals of both ligands. Time-dependent-DFT calculations were carried out with MeCN included in the model (IEFPCM-B3LYP/LanL2DZ) to aid the assignment of the spin-allowed absorption transitions (all molecular orbital representations were provided by DFT calculations; B3LYP/LanL2DZ). While the simulated MLCT bands are slightly blue-shifted relative to the measured spectra, there is reasonable agreement between the computational and experimental data (Figure 2.5-Figure 2.7). It was determined that the HOMO, HOMO-1 and HOMO-2 levels of **2.4** (Figure 2.7), for example, contain significant metal character (which is corroborated by the electrochemistry experiments) with some delocalization over the tridentate ligands, while the low-lying unoccupied orbitals are localized primarily to the π^* networks of both ligands with the LUMO assigned to the **C^NC-Br** ligand (Figure 2.7). The low-energy shoulder of the MLCT band appears to involve the π^* of the terpy ligand (λ_1), while the λ_2 transition, which is characterized by the highest oscillator strength of the transitions in the visible region, involves the promotion of an electron to the LUMO. The low-energy tail is tentatively assigned as the direct population of the $^3\text{MLCT}$ manifold. The higher energy transitions (i.e., $<400 \text{ nm}$) correspond to a combination of MLCT and ligand-centered transitions of the **C^NC-Br** (Figure 2.4).

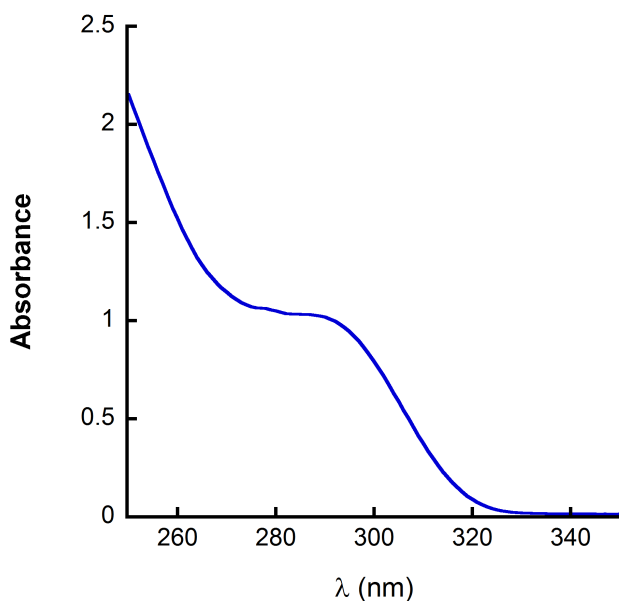


Figure 2.4 UV-*vis* absorption spectrum of Ag(C^NC-Br) recorded in MeCN under ambient conditions. Adapted with permission from *J. Am. Chem. Soc.*, 2012, *134* (30), pp 12354–12357. Copyright 2017 American Chemical Society.

The orbitals for **2.1-2.3** are reasonably similar to that of **2.4** in that the HOMO-2 to HOMO levels are primarily metal-based and with low-lying unoccupied orbitals confined to the π^* system of the two ligands (Figure 2.5 and 2.6). The computational data indicate that the LUMO shifts from the terpy ligand in **2.1** and **2.2** to the carbene in **2.3** and **2.4**. Thus, the excited electron density is expected to reside on the terpy for **2.2** but on the carbene ligand for **2.3** and **2.4** in the ³MLCT state. Taking this feature into account with the optical and electrochemical data, the relative energy levels appear to follow the order depicted in Figure 2.3. The presence of EWGs on the terpy, for example, lower the terpy-based LUMO to a greater extent than the metal-based HOMO, thereby inducing a bathochromic shift for **2.2** relative to **2.1**. The

bathochromic shifts for **2.3** and **2.4** relative to **2.1** are consistent with the EDGs on the terpy inducing higher HOMO energies and a LUMO that is confined to the C[^]N[^]C ligands.

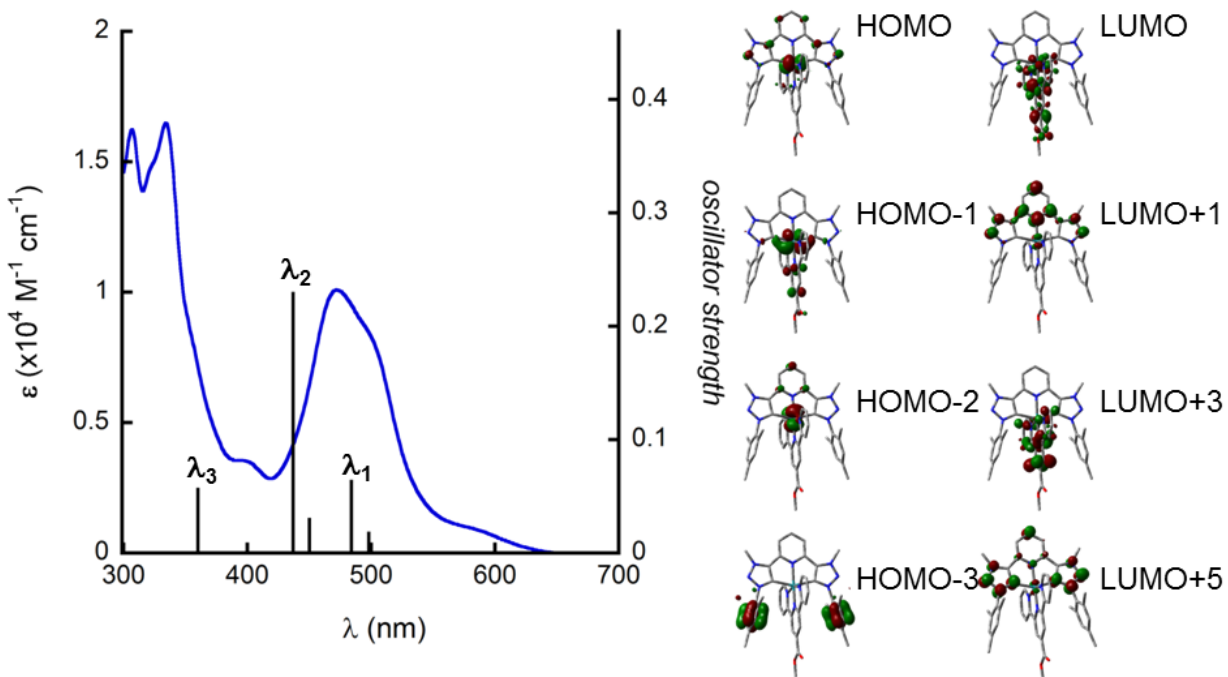


Figure 2.5 Experimental UV-*vis* absorption spectrum of **2.2** overlaid with calculated transitions represented by vertical bars. Details of the three largest calculated transitions (theoretical wavelength in nm, oscillator strength, % contribution to transition): λ_1 : HOMO-1 \rightarrow LUMO (484, 0.065, 54%); λ_2 : HOMO \rightarrow LUMO+3 (437, 0.230, 30%); λ_3 : HOMO-1 \rightarrow LUMO+5 (360, 0.058, 72%). Adapted with permission from *J. Am. Chem. Soc.*, 2012, *134* (30), pp 12354–12357. Copyright 2017 American Chemical Society.

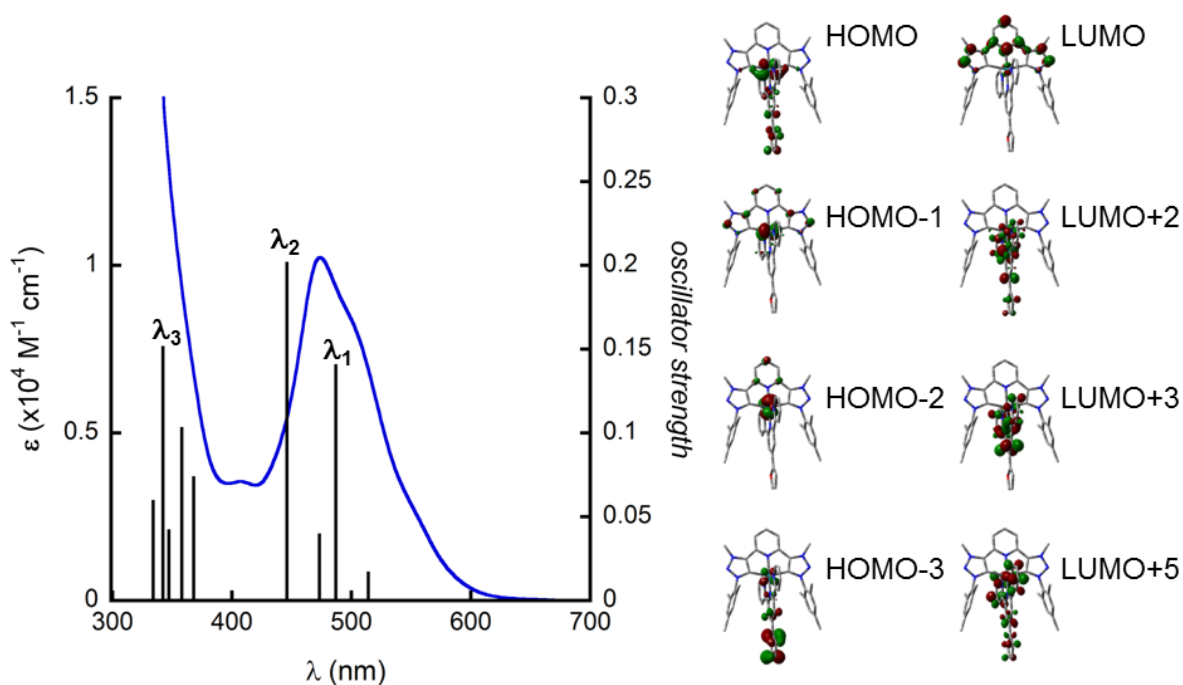


Figure 2.6 Experimental UV-*vis* absorption spectrum of **2.3** overlaid with calculated transitions represented by vertical bars. Details of the three largest calculated transitions (theoretical wavelength in nm, oscillator strength, % contribution to transition): λ_1 : HOMO \rightarrow LUMO+2 (487, 0.1411, 65%); λ_2 : HOMO-2 \rightarrow LUMO (446, 0.2021, 43%); λ_3 : HOMO \rightarrow LUMO+5 (358, 0.1037, 91%). Adapted with permission from *J. Am. Chem. Soc.*, 2012, *134* (30), pp 12354–12357. Copyright 2017 American Chemical Society.

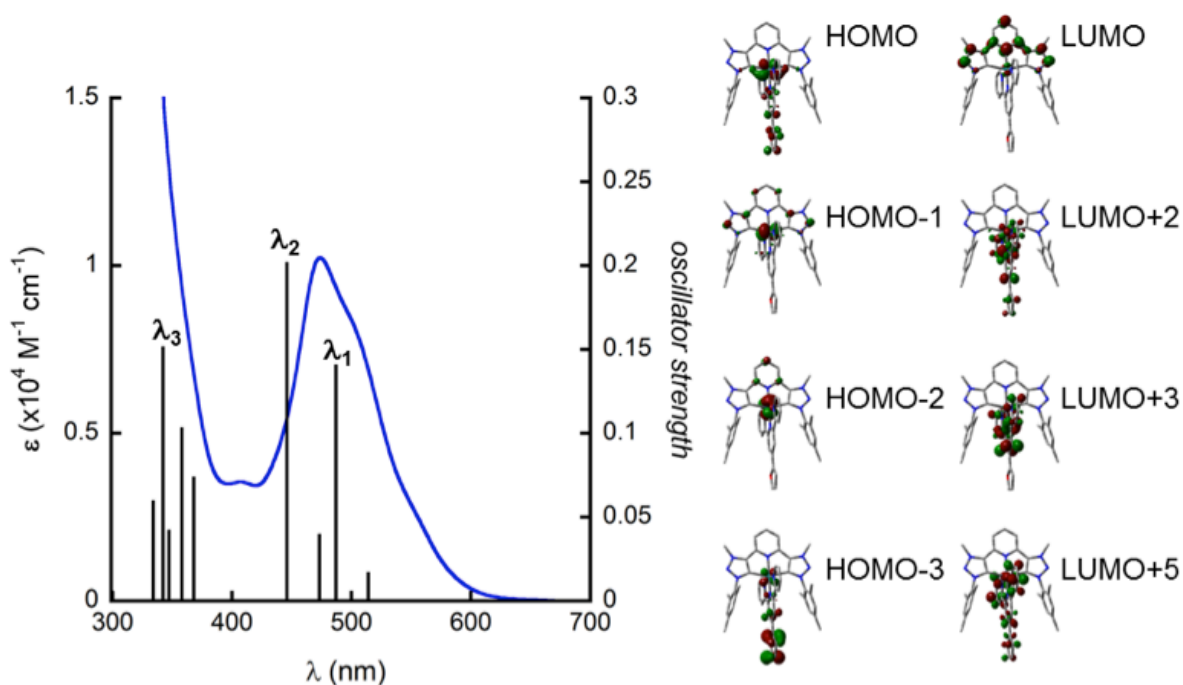


Figure 2.7. Experimental UV-vis absorption spectrum of **2.4** overlaid with calculated transitions represented by vertical bars. Details of the three largest calculated transitions (theoretical wavelength in nm, oscillator strength, % contribution to transition): λ_1 : HOMO→LUMO+2 (486, 0.1464, 65%) λ_2 : HOMO-2→LUMO (446, 0.1848, 46%) λ_3 : HOMO→LUMO+5 (356, 0.1006, 91%). Select molecular orbitals are also shown. Adapted with permission from *J. Am. Chem. Soc.*, 2012, *134* (30), pp 12354–12357. Copyright 2017 American Chemical Society.

Table 2.1. Photophysical and electrochemical data for **2.1-2.4** and [Ru(terpy)₂](PF₆)₂.

	2.1	2.2	2.3	2.4	[Ru(terpy) ₂](PF ₆) ₂
λ_{abs} (nm) ^b	463	472	472	473	476 ⁱ
ε ($\times 10^4$ M ⁻¹ cm ⁻¹)	1.0	1.0	1.0	1.0	1.5 ⁱ
λ_{em} (nm) ^c	643	688	691	694	-
τ (ns) ^c	385	1720	6980	7900	0.25 ^h
Φ (%) ^{c,d}	11.4	7.5	2.5	1.7	-
E_{ox} (V) ^{e,f}	1.24	1.31	1.18	1.22	1.52 ^h
E_{red} (V) ^{e,f}	-1.31	-1.08	-1.33	-1.24	-1.02 ^h
E_{0-0} (eV) ^g	2.09	2.02	2.02	1.98	2.13 ^h

^aMeasured in deaerated MeCN at 298 K unless otherwise stated. ^bMaximum absorption of lowest energy MLCT band. ^cEmission maxima measured in deaerated EtOH:MeOH (v/v 80:20). ^dDetermined using [Ru(bpy)₃](PF₆)₂ as a standard. ^eMeasured in MeCN using a 0.1 M NBu₄BF₄ supporting electrolyte and [Fc]⁺/[Fc]⁰ as a standard. ^fReported vs NHE. ^gDetermined by the intersection point of the absorption and emission curve normalized to the lowest energy MLCT band. ^hReported in ref. 120. ⁱReported in ref. 119. Adapted with permission from *J. Am. Chem. Soc.*, 2012, 134 (30), pp 12354–12357. Copyright 2017 American Chemical Society.

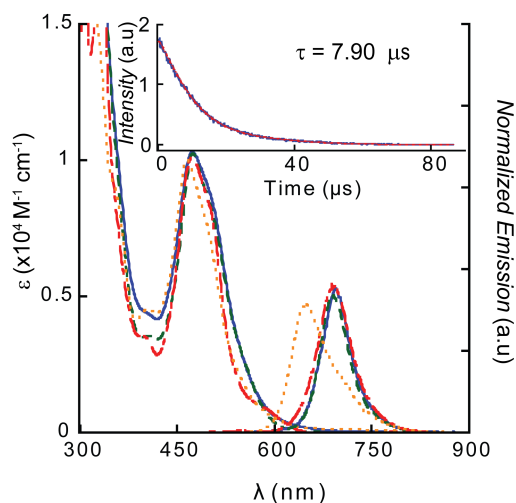


Figure 2.8. UV-*vis* and normalized emission spectra for **2.1** (orange), **2.2** (red), **2.3** (green) and **2.4** (blue) recorded in deaerated ethanol/methanol (80:20 *v/v*) at ambient temperatures. (Emission spectra are normalized to MLCT absorptions). *Inset:* Representative time-correlated single photon emission decay profile for **2.4** (blue) overlaid with a monoexponential fit (red) in ethanol/methanol (80:20 *v/v*). Adapted with permission from *J. Am. Chem. Soc.*, 2012, *134* (30), pp 12354–12357. Copyright 2017 American Chemical Society.

The emission spectra for **2.2-2.4** were measured in deaerated ethanol/methanol (80:20 *v/v*) solutions at 77 and 298 K upon excitation at wavelengths corresponding to the maximum of the MLCT band at *ca.* 500 nm. Each complex was characterized by a Stokes shift in excess of 50000 cm^{-1} , which is consistent with phosphorescence. Similar experiments performed in air revealed a partial quenching of the emission band that is consistent with a triplet emitting state, and thus we ascribe the decay for **2.2-2.4** to be emission from a $^3\text{MLCT}$ state. The $E_{0,0}$ values were assigned as the energies corresponding to the intersections of the absorption and emission spectra, where the emission band was normalized to the apparent $^1\text{MLCT}$ excitation band). The

E_{0-0} values were determined to be *ca.* 2 eV for the series (Table 2.1), with the largest and smallest E_{0-0} values being measured for **2.1** and **2.4**, respectively.

The excited-state lifetimes (τ) for **2.2-2.4** in deaerated solvents were measured by time-correlated single-photon counting to be 1.7-7.9 μs . These values are striking in that they are several orders of magnitude longer than τ values typically observed for the vast majority of Ru(II) chromophores bearing a terpy ligand, even though the abnormal carbene ligand imposes a more strained ligand environment around the metal center ($\angle\text{N-Ru-N} = 154.3^\circ$) than of terpy ($\angle\text{N-Ru-N} = 158.4^\circ$).²⁵ Moreover, the lifetime of **2.4** even beats the longest lifetimes achieved so far by any mononuclear Ru(II) complex.^{125-127,134} Interestingly, the data for **2.1-2.4** does not strictly conform to the energy gap law: the shortest τ value is observed in the case with the largest energy gap (*i.e.*, **2.1**) while the longest τ was measured with **2.4**, which is characterized by the smallest E_{0-0} . We therefore surmise that the longer τ values of **2.2-2.4** relative to **2.1** are governed primarily by the increased separation between the emitting $^3\text{MLCT}$ state and the deactivating ^3MC state (Figure 2.3). Lending support to a thermally inaccessible ^3MC state is that the lifetimes at 77 K for complexes **2.1-2.4** (12-18 μs ; Table 2.2) are similar to that exhibited by $[\text{Ru}(\text{terpy})_2](\text{PF}_6)_2$ (11 μs) at 77 K. The conjugated substituents of the terpy ligand may also have an auxiliary role on the τ values (0.39, 1.72, and 6.98 μs where $\text{R}_2 = -\text{H}$, $-\text{CO}_2\text{Me}$, and $-\text{2-furyl}$, respectively), but the increase in the τ value with the terminal bromides present in **2.4** is indicative of inductive effects on the carbene ligand playing a significant role in the photophysics.

Table 2.2. Excited-state lifetime (τ) data for **2.2-2.4**. (Values expressed in units of μs .^a)

<i>Temperature</i>	2.2	2.3	2.4
298 K	1.7 (0.98)	7.0 (1.04)	7.9 (0.97)
77 K	12.9 (0.99)	18.3 (1.00)	17.1 (1.02)

[a] τ measured in deaerated EtOH/MeOH (80:20 v/v) solution. Values in parentheses indicate χ^2 as the goodness of fit. Adapted with permission from *J. Am. Chem. Soc.*, 2012, *134* (30), pp 12354–12357. Copyright 2017 American Chemical Society.

To the best of my knowledge, the lifetimes of **2.3** and **2.4** are among the highest for any monometallic ruthenium(II) complexes where emission originates from a $^3\text{MLCT}$ state. These long-lived excited states are manifested in the strongly σ -donating and π -accepting ability of the carbene ligand resolving the $^3\text{MLCT}$ and ^3MC states, while the presence of EWGs or EDGs about the terpy helps to further separate these states. These collective results demonstrate the enormous potential of using abnormal carbene complexes to modify the photophysical properties of ruthenium(II) complexes for a myriad of applications.

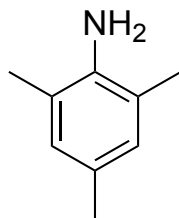
2.3.Experimental Details

2.3.1 Synthesis

All manipulations were performed using solvents passed through an MBraun solvent purification system prior to use; chloroform (CHCl_3) and tetrahydrofuran (THF) solvents were analytical grade (without stabilizer). All known and commercially available reagents were purchased from commercial suppliers and used as received unless otherwise stated. 2,6-diethynylpyridine,¹⁴² 2-nitromesitylene,¹⁴³ **2.12a**,¹¹⁹ **2.13a**,¹¹⁹ **2.5a**,¹¹⁹ 4'-(furan-2-yl)-2,2':6',2''-terpyridine (**2.14**),¹⁴⁴ were synthesized according to the literature procedures. All reactions were

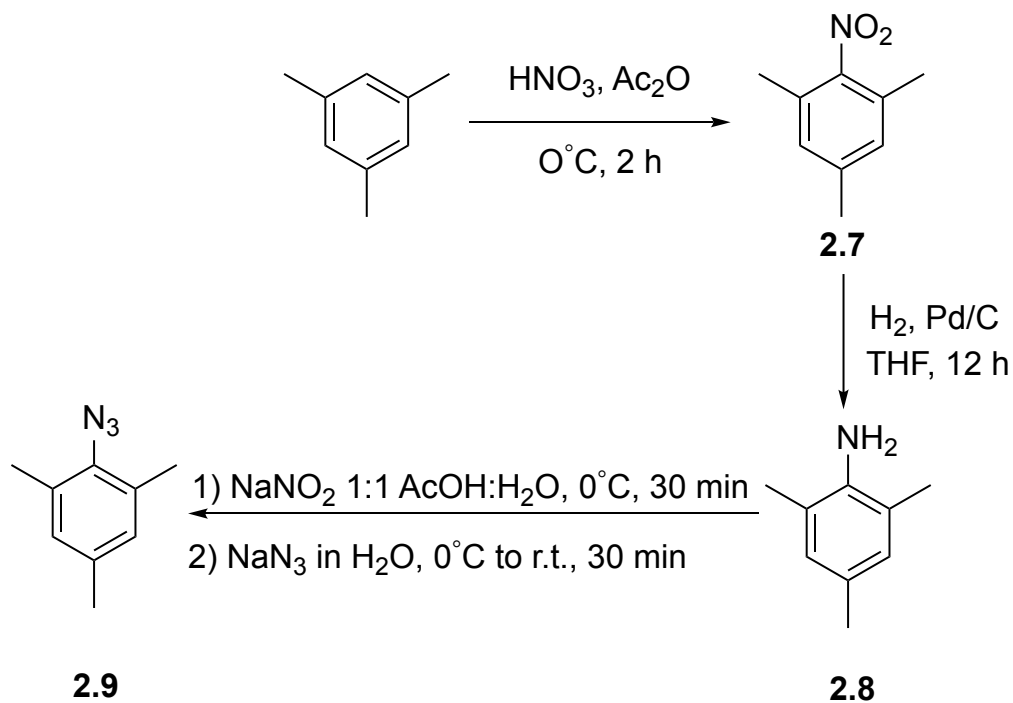
performed in oven-dried flasks and were monitored by thin layer chromatography (TLC) on aluminum-backed sheets pre-coated with silica 60 F254 adsorbent (0.25 mm thick; Merck, Germany). Purification by column chromatography was carried out using silica (Silicycle: Ultrapure Flash Silica) and Sephadex L-20. 1D and 2D ^1H and ^{13}C spectra were recorded at 400 MHz and 600 MHz with BrukerAvance 400 MHz, BrukerAvance II 400 MHz, BrukerAvance III 400 MHz and BrukerAvance III 600 MHz instruments at 298 K. ^1H NMR chemical shifts (δ) are reported in parts per million (ppm) from low to high field and referenced to residual non-deuterated solvent. Elemental analysis (EA) and electrospray ionization (ESI) and matrix-assisted laser desorption/ionization time-of-flight (MALDI) mass spectrometry data were collected at the University of Calgary using Perkin Elmer *Model 2400 series II* Elemental Analyzer and Agilent 6520 Q-ToF Mass Spectrometers, respectively.

Safety Comment. Sodium azide is very toxic, personal protection precautions should be taken. As low molar mass organic azides are potential explosives, care must be taken during their handling. All azide experiments were conducted with ice chilled aqueous solutions of sodium nitrate and sodium azide and added dropwise behind a blast shield.

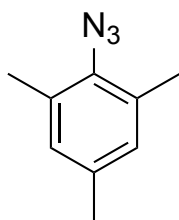


2,4,6-Trimethylaniline (2.8). 2-Nitromesitylene (**2.7**)¹⁴³ (2.00 g, 12.1 mmol) was dissolved in 40 ml of THF in a two-necked flask. After the addition of 10%-activated Pd on carbon (1 g), the flask was purged with H_2 and stirred vigorously for 12 h. The reaction mixture was then filtered

through Celite prior to the removal of solvent to afford 1.62 g (12.0 mmol) of 2,4,6-trimethylaniline. The reagent was used in subsequent reactions without further purification. ^1H NMR (400 MHz, CDCl_3 , ppm) δ 6.78 (d, $J = 0.5$ Hz, 2H), 3.47 (bs, 2H), 2.22 (s, 3H), 2.17 (s, 6H).

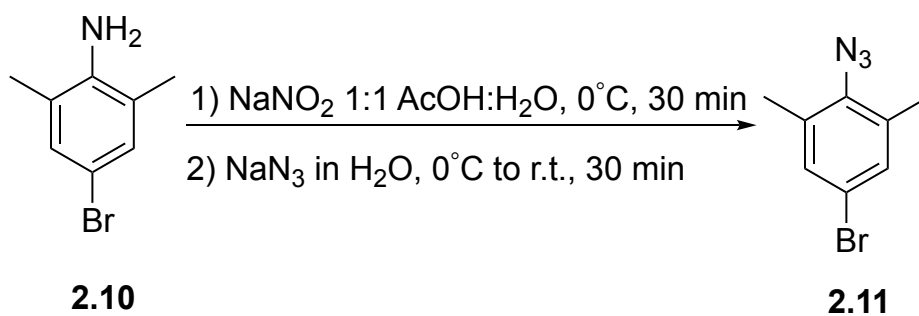


Scheme 2.2 Synthetic route for compound **2.9**.

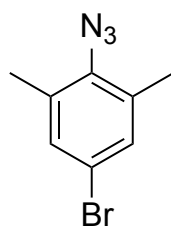


2-azido-1,3,5-trimethylbenzene (2.9). To a cooled mixture (0°C) of 2,4,6-trimethylaniline (**2.8**) (1.62 g, 12.0 mmol) in 20 ml of AcOH and H_2O (50:50, v/v) was added a saturated aqueous solution of NaNO_2 (1.29 g, 18.7 mmol). After consumption of the starting material (~ 1 h), a saturated aqueous solution of NaN_3 (2.79 g, 22.0 mmol) was added stepwise to the reaction mixture at 0°C . The resultant mixture was warmed to room temperature and stirred for 1 h. The

reaction mixture was diluted with 30 ml of H₂O and 30 ml of Et₂O, and solid Na₂CO₃ was slowly added until the pH of the aqueous phase reached 7. The phases were separated, and the resulting aqueous phase was extracted with an additional 2 × 30 ml of Et₂O. The combined organic phases were washed with 1 × 20 ml of distilled H₂O and 1 × 20 ml of brine. The resulting organic phase was dried over MgSO₄ and the heterogeneous mixture was filtered. The filtrate was concentrated *in vacuo* to obtain the desired mesitylazide (1.69 g, 87%); ¹H NMR (400 MHz, CDCl₃, ppm) δ 6.85 (d, *J* = 0.5 Hz, 2H), 2.34 (s, 6H), 2.27 (s, 3H).

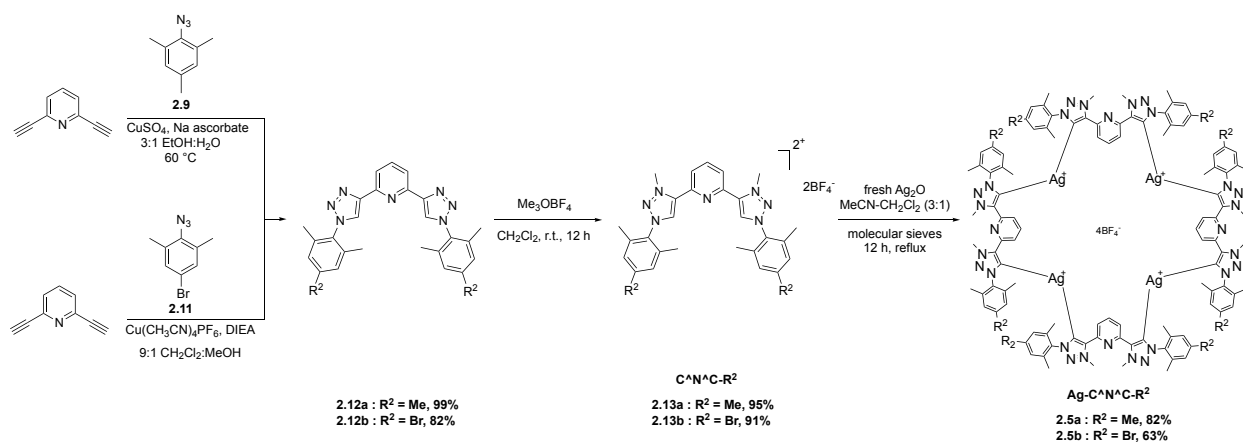


Scheme 2.3 Synthetic route for compound **2.11**.

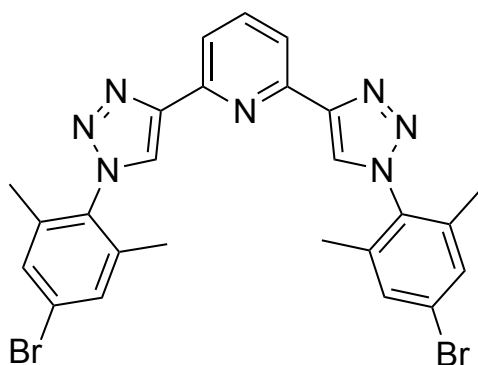


4-bromo-2,6-dimethylphenylazide (2.11). To a cooled mixture (0 °C) of 4-bromo-2,6-dimethylaniline (**2.10**) (1.00 g, 5.00 mmol) in a 50:50 *v/v* mixture of AcOH and H₂O (20 ml) was added a saturated solution of NaNO₂ (517 mg, 7.50 mmol). After the consumption of the starting material, a saturated solution of NaN₃ (1.91 g, 15.0 mmol) was added stepwise to the reaction mixture at 0 °C. The resulting mixture was warmed to room temperature and stirred for 1 h. The reaction mixture was diluted with 30 ml of H₂O and 30 ml of Et₂O, and solid Na₂CO₃ was slowly

added until the pH of the aqueous phase reached 7. The phases were separated, and then the resulting aqueous phase was extracted with an additional 2×30 ml of Et₂O. The combined organic phases were washed with 1×20 ml of distilled H₂O and 1×20 ml of brine. The organic phase was dried over MgSO₄ and the heterogeneous mixture was filtered. The filtrate was concentrated *in vacuo* to obtain the desired azide (1.05 g, 93%). ¹H NMR (400 MHz, CDCl₃, ppm) δ 7.16 (s, 2H), 2.33 (s, 6H); ¹³C{¹H} NMR (101 MHz, CDCl₃, ppm) δ 136.18, 134.13, 131.56, 118.67, 17.96.

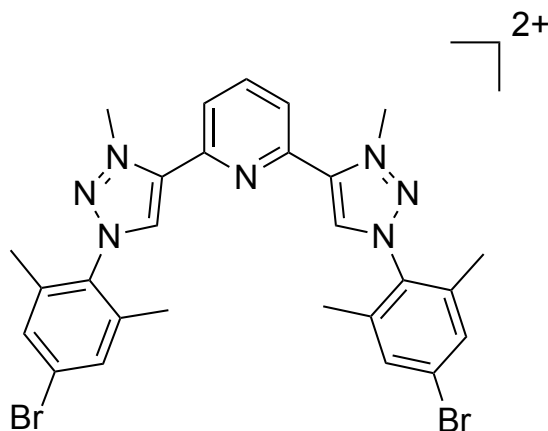


Scheme 2.4. Synthetic route for the transmetalation silver carbene complex (Ag-C^N^C-R²).

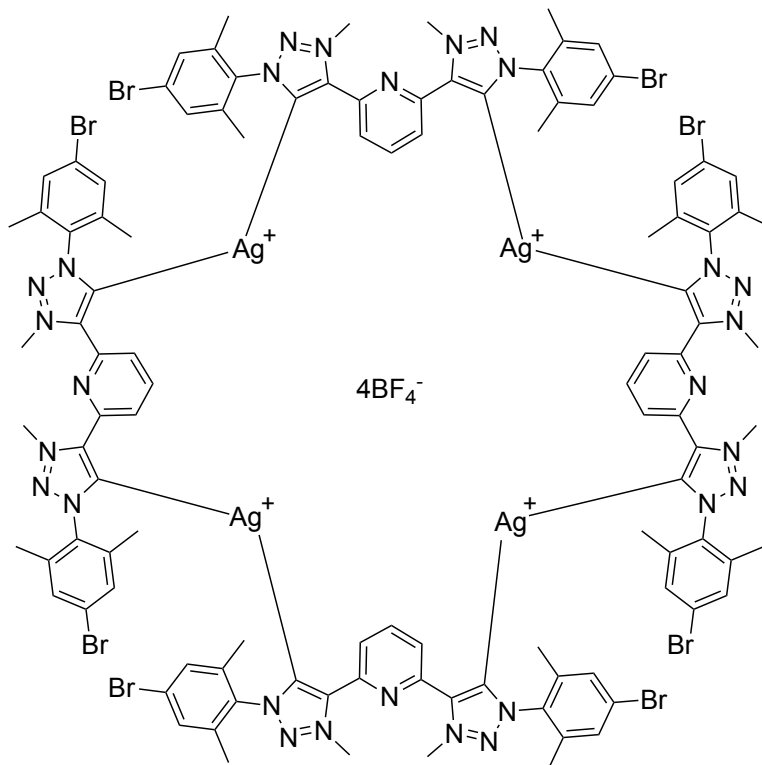


2,6-bis(1-(2,6-dimethyl-4-bromophenyl)-1H-1,2,3-triazol-4-yl)pyridine (2.12b). To a solution of **2.11** (822 mg, 3.64 mmol), 2,6-diethynylpyridine (191 mg, 1.50 mmol), and *N,N*-diisopropylethylamine (0.65 ml, 3.7 mmol) in CH₂Cl₂/MeOH (50 ml, 9:1 *v/v*) was added

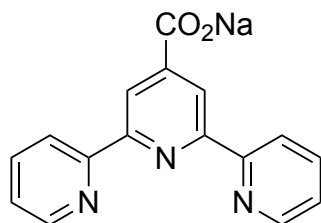
[Cu(MeCN)₄]PF₆ (85 mg, 0.23mmol). The mixture was stirred for 48 h and then concentrated under reduced pressure. The addition of 10 ml of EtOAc produced the product as a precipitate, which was collected by vacuum filtration and washed with EtOAc (5-10 ml) (yield = 717 mg, 82%). ¹H NMR (400 MHz, CDCl₃, ppm) δ 8.25 (s, 2H), 8.23 (s, 2H), 8.00 – 7.95 (m, 1H), 7.37 (s, 4H), 2.04 (s, 12H).



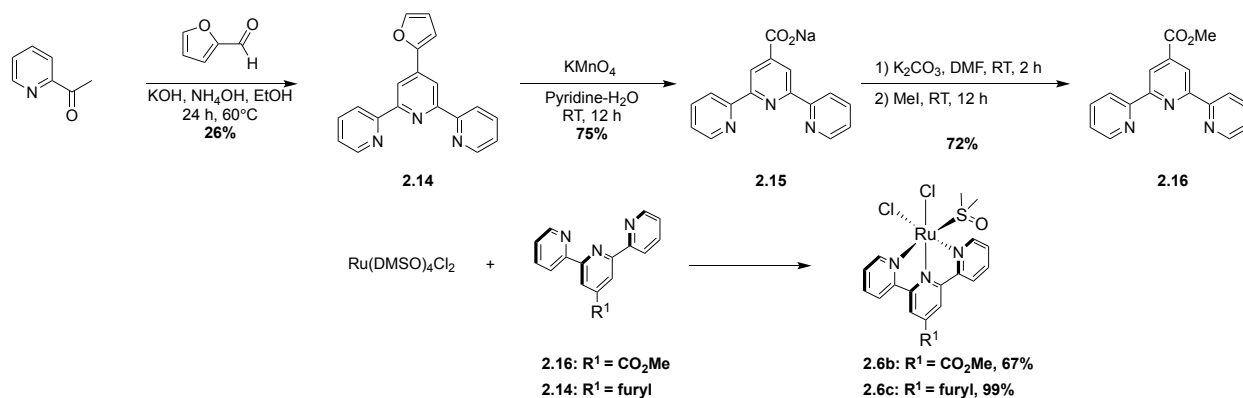
4,4'-(pyridine-2,6-diyl)bis(1-(2,6-dimethyl-4-bromophenyl)-3-methyl-1H-1,2,3-triazol-3-ium) tetrafluoroborate, C^NC-Br (2.13b). A 50-ml Schlenk flask containing dry CH₂Cl₂ (15 ml), **2.12b** (447 mg, 0.772 mmol) and trimethyloxoniumtetrafluoroborate (282 mg, 1.91 mmol) was stirred for 12 h at room temperature under a nitrogen atmosphere, and then evaporated to dryness to obtain a crude yellow oil. The excess oxonium salt was removed by suspending the crude mixture in MeOH prior to removing all the volatile species *in vacuo*. This procedure yielded a white microcrystalline powder (550 mg, 91%) that was used in the next step without further purification. ¹H NMR (400 MHz, CD₃CN, ppm): δ 9.04 (s, 2H), 8.43 – 8.36 (m, 1H), 8.19 (d, *J* = 8.0 Hz, 2H), 7.63 (s, 4H), 4.67 (s, 6H), 2.18 (s, 12H).



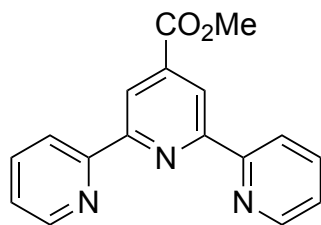
$\text{Ag}(\text{C}^{\wedge}\text{N}^{\wedge}\text{C})$ (2.5b). A 50-ml Schlenk flask containing **2.13b** (430 mg, 0.54 mmol) and dried silver(I)-oxide (281 mg, 1.21 mmol) in dry and degassed MeCN (20 ml) and CH_2Cl_2 (10 ml) in activated 4 Å molecular sieves was left at reflux under argon for 12 h in the dark. After being cooled to room temperature, the mixture was filtered over celite and concentrated *in vacuo*. The concentrated solution was dropped into Et_2O and the resulting precipitate was filtered and washed with Et_2O . The solid was dissolved in CH_2Cl_2 , filtered and precipitated from a concentrated CH_2Cl_2 solution into Et_2O to yield the product as light gray solid (277 mg, 63%) that was used without further purification. ^1H NMR (400 MHz, CD_3CN , ppm): δ 8.29 (d, $J = 7.9$ Hz, 2H), 8.03 – 7.98 (m, 1H), 7.48 (s, 4H), 4.46 (s, 6H), 2.13 (s, 12H).



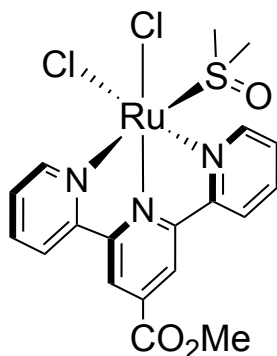
Sodium[2,2':6',2''-terpyridine]-4'-carboxylate (2.15). To a solution of **2.14**¹⁴⁴ (2.2 g, 7.4 mmol) in pyridine (30 ml) and H₂O (15 ml) was added KMnO₄ (7.1 g, 45 mmol) in stepwise portions and then stirred at room temperature for 48 h. Residual KMnO₄ was reduced by adding Na₂S₂O₃ dissolved in H₂O until the violet colour of the mixture disappeared. The solution was made basic by addition of NaOH (2M) and the resultant MnO₂ formed was filtered off. The solvent was removed from the filtrate *in vacuo*, and then reconstituted in NaOH (pH ~ 12). The resultant suspension was filtered and the white solid was collected. This purification process was repeated twice to yield the product as a gray microcrystalline solid (1.65 g, 75%). ¹H NMR (400 MHz, DMSO, ppm) δ 8.85 (s, 2H), 8.74 – 8.70 (m, 2H), 8.61 (d, *J* = 7.9 Hz, 2H), 7.99 (td, *J* = 7.7, 1.8 Hz, 2H), 7.46 (ddd, *J* = 7.5, 4.8, 1.1 Hz, 2H).



Scheme 2.5. Synthesis of Ruthenium terpy derivatives for transmetalation reaction.

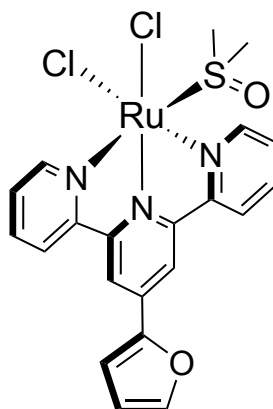


Methyl[2,2':6',2''-terpyridine]-4'-carboxylate (2.16). To a solution of **2.15** (250 mg, 0.83 mmol) in 15 ml DMF was added K_2CO_3 (315 mg, 2.28 mmol). After the mixture was stirred at room temperature for 2 h, MeI (0.25 ml, 4.0 mmol) was added dropwise under nitrogen. After an additional 12 h of stirring, the reaction was diluted with EtOAc and washed with H_2O . The filtrate was diluted with 30 ml of H_2O and extracted with 30 ml of EtOAc. The phases were separated, and the resulting aqueous phase was extracted with an additional 2×30 ml of EtOAc. The combined organic phases were washed with 3×20 ml of distilled H_2O and 3×20 ml of a saturated LiCl solution. The organic phase was dried with MgSO_4 prior to isolating the product as a white solid (175 mg, 72%). ^1H NMR (400 MHz, CDCl_3 , ppm) δ 8.99 (s, 2H), 8.74 (ddd, $J = 4.8, 1.7, 0.9$ Hz, 2H), 8.61 (dt, $J = 7.9, 1.0$ Hz, 2H), 7.86 (td, $J = 7.8, 1.8$ Hz, 2H), 7.35 (ddd, $J = 7.5, 4.8, 1.2$ Hz, 2H), 4.01 (s, 3H). $^{13}\text{C}\{^1\text{H}\}$ NMR (101 MHz, CDCl_3 , ppm) δ 165.97, 156.73, 155.63, 149.49, 139.88, 137.02, 124.27, 121.40, 120.52, 77.16, 52.74.

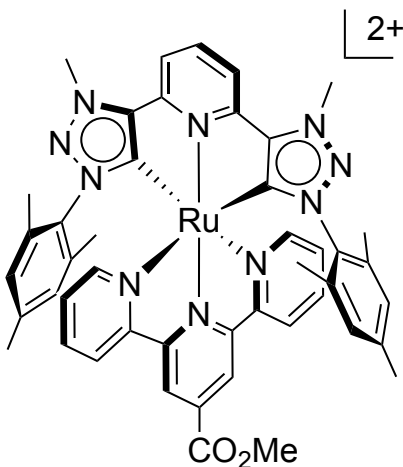


***cis*-Ru(terpy-CO₂Me)(DMSO)Cl₂ (2.6b).** To a round-bottom flask containing **2.16** (195 mg, 0.669 mmol) in 20 ml of EtOH was added *cis*-Ru(DMSO)₄Cl₂ (400 mg, 0.669 mmol). The

mixture was set to reflux and stirred for 24 h until a brown-red precipitate formed, and then the reaction mixture was left to cool to room temperature. The precipitate was collected by filtration and washed with EtOH to remove residual *cis*-Ru(DMSO)₄Cl₂ to obtain a brown-purple solid (250 mg, 67%). ¹H NMR (400 MHz, CD₃CN, ppm): δ 9.14 (dd, *J* = 5.5, 0.9 Hz, 2H), 8.73 (s, 2H), 8.45 (d, *J* = 8.0 Hz, 2H), 8.09 (td, *J* = 7.9, 1.6 Hz, 2H), 7.74 (ddd, *J* = 7.6, 5.5, 1.2 Hz, 2H), 4.02 (s, 3H), 2.58 (s, 6H).

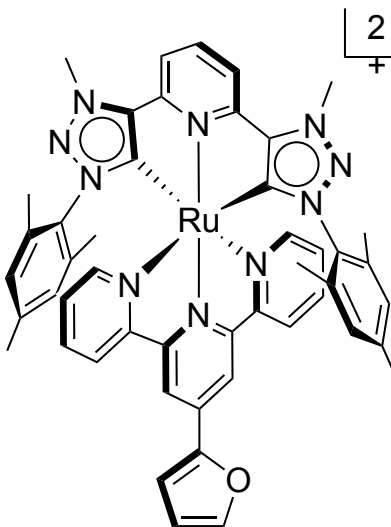


***cis*-Ru(terpy-furyl)(DMSO)Cl₂ (2.6c).** To a round bottom flask containing **2.14**¹⁴⁴ (550 mg, 1.84 mmol) in 20 ml of EtOH was added *cis*-Ru(DMSO)₄Cl₂ (908 mg, 1.89mmol). The reaction was stirred at reflux for 24 h until a red precipitate formed. After the reaction was cooled to room temperature, a red-violet precipitate was collected by filtration and washed with EtOH to remove unreacted *cis*-Ru(DMSO)₄Cl₂ to obtain the product as a red-purple solid (1.02 g, 99%). ¹H NMR (400 MHz, CD₃CN) δ 9.01 (d, *J* = 4.6 Hz, 2H), 8.52 (s, 2H), 8.43 (d, *J* = 8.0 Hz, 2H), 8.04 (td, *J* = 7.9, 1.4 Hz, 2H), 7.79 (d, *J* = 1.5 Hz, 1H), 7.71 – 7.63 (m, 2H), 7.38 (d, *J* = 3.4 Hz, 1H), 6.72 (dd, *J* = 3.4, 1.7 Hz, 1H). (The absence of the 2CH₃-proton signal of the DMSO ligand is attributed to the ligand exchange with deuterated MeCN NMR solvent (CD₃CN).)

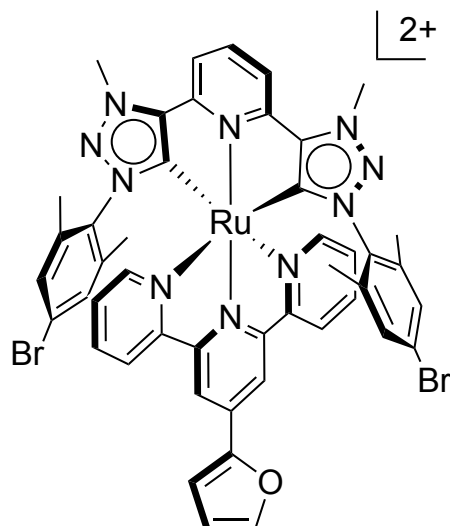


Ru(terpy-CO₂Me)(C^NC) (2.2). A 10-ml glass vial was charged with dry, deaerated CH₂Cl₂ (3 ml), *cis*-[Ru(terpy-CO₂Me)(DMSO)Cl₂] (**2.6b**) (35 mg, 0.064 mmol) and Ag(C^NC) (**2.5a**)¹¹⁹ (40 mg, 0.060 mmol) and capped prior to sparging with nitrogen. The mixture was stirred at 70 °C for 5 d in the dark and then cooled to room temperature. Excess ammonium tetrafluoroborate (220 mg) was then added to the mixture at room temperature followed by stirring for 1.5 h. The precipitate was then removed from the solution by vacuum filtration. Solvent was removed from the filtrate *in vacuo* to yield the solid. Fractionalized crystallization by vapor diffusion of Et₂O into a concentrated MeOH solution yielded the product as a dark red microcrystalline solid (22 mg, 35%). ¹H NMR (600 MHz, CD₃CN, ppm): δ 8.47 – 8.30 (m, 5H), 8.26 (dd, *J* = 8.8, 7.5 Hz, 2H), 8.21 – 8.15 (m, 2H), 7.93 – 7.88 (m, 2H), 7.55 (d, *J* = 4.9 Hz, 2H), 7.28 – 7.23 (m, 2H), 6.43 (s, 4H), 4.52 (s, 6H), 4.10 (s, 3H), 2.04 (s, 6H), 0.70 (s, 12H); ¹³C{¹H} NMR (151 MHz, CD₃CN, ppm) δ 183.04, 156.46, 153.17, 152.64, 151.54, 146.85, 140.52, 137.38, 136.34, 133.69, 133.61, 130.20, 128.34, 126.59, 123.45, 120.09, 118.94, 65.25, 52.77, 38.84, 19.81, 14.60, 14.52; HRMS (ESI-ToF, *m/z*): 957.2720 ([M-BF₄]⁺), C₄₆H₄₄BF₄N₁₀O₂Ru⁺

requires 957.2710. Anal Calcd for $C_{46}H_{44}B_2F_8N_{10}O_2Ru$: C, 52.94; H, 4.25; N, 13.42; Found: C, 52.90; H, 4.22; N, 13.38.



Ru(terpy-furyl)(C^NC) (2.3). A capped 10-ml glass vial containing dry, deaerated CH_2Cl_2 (3 ml), *cis*-[Ru(terpy-furyl)(DMSO)Cl₂] (**2.6c**) (35 mg, 0.064 mmol) and Ag(C^NC) (**2.5a**) (40 mg, 0.060 mmol) was sparged with nitrogen for 20 min and then stirred at 70 °C for 5 d in the dark. Excess ammonium tetrafluoroborate (220 mg) was then added to the mixture at room temperature followed by stirring for 1.5 h. The precipitate was then removed from the solution by vacuum filtration. Solvent was removed from the filtrate *in vacuo* to yield the solid. Fractionalized crystallization by vapor diffusion of Et₂O into a concentrated MeOH solution yielded the product as a dark red solid (35 mg, 55%). ¹H NMR (400 MHz, MeOD, ppm) δ 8.52 (d, *J* = 8.1 Hz, 2H), 8.40 – 8.33 (m, 5H), 8.00 – 7.94 (m, 2H), 7.91 (d, *J* = 1.2 Hz, 1H), 7.63 (d, *J* = 5.6 Hz, 2H), 7.47 (d, *J* = 3.5 Hz, 1H), 7.31 – 7.26 (m, 2H), 6.82 (dd, *J* = 3.5, 1.8 Hz, 1H), 6.48 (s, 4H), 4.72 (s, 6H), 0.83 (s, 12H). HRMS (MALDI, *m/z*): 965.2762 ([M-BF₄]⁺), $C_{46}H_{44}BF_4N_{10}O_1Ru^+$ requires 965.2786. Anal calcd for $C_{46}H_{44}B_2F_8N_{10}O_1Ru$: C, 54.82; H, 4.22; N, 13.32; Found: C, 54.30; H, 4.25; N, 13.25



Ru(terpy-furyl)(C^NC-Br)(2.4). A 10-ml glass vial containing dry, deaerated CH₂Cl₂ (3 ml), *cis*-[Ru(terpy-furyl)(DMSO)Cl₂] (**2.6c**) (33 mg, 0.060 mmol) and Ag(C^NC-Br) (**2.5b**) (62 mg, 0.077 mmol) was capped prior to an additional 20-min N₂ purge. The mixture was stirred at 70 °C for 5 d in the dark and then cooled to room temperature. Excess ammonium tetrafluoroborate (220 mg) was then added to the mixture at room temperature followed by stirring for 1.5 h. The precipitate was then removed from the solution by vacuum filtration. Solvent was removed from the filtrate *in vacuo* to yield the solid. Fractionalized crystallization by vapor diffusion of Et₂O into a concentrated MeOH solution yielded a dark red microcrystalline solid of **2.4** (29 mg, 48%). ¹H NMR (400 MHz, CD₃CN, ppm) δ 8.33 (d, *J* = 8.0 Hz, 2H), 8.26 – 8.15 (m, 5H), 7.89 (td, *J* = 8.0, 1.5 Hz, 2H), 7.83 (d, *J* = 1.3 Hz, 1H), 7.50 (d, *J* = 4.9 Hz, 2H), 7.38 (d, *J* = 2.9 Hz, 1H), 7.23 – 7.18 (m, 2H), 6.86 (s, 4H), 6.77 (dd, *J* = 3.5, 1.8 Hz, 1H), 4.54 (s, 6H), 0.79 (s, 12H); ¹³C{¹H} NMR (101 MHz, CD₃CN, ppm) δ 183.70, 156.82, 152.85, 144.57, 136.58, 136.30, 130.64, 126.50, 123.43, 118.93, 115.32, 38.92, 14.55. HRMS (MALDI, *m/z*): 1095.0685 ([M-BF₄]⁺), C₄₆H₃₈BBr₂F₄N₁₀O₁Ru⁺ requires 1095.0665. Anal Calcd for C₄₆H₃₈B₂Br₂F₈N₁₀O₁Ru: C, 46.77; H, 3.24; N, 11.86; Found: C, 46.90; H, 3.31; N, 11.78.

2.3.2 Characterization

Electrochemical measurements were performed under anaerobic conditions with a Princeton Applied Research VersaStat 3 potentiostat using dry solvents, Pt working and counter electrodes, Ag pseudoreference electrode, and 0.1 M NBu_4BF_4 supporting electrolyte. Electronic spectroscopic data were collected in MeCN solutions using a Cary 5000 UV-*vis* spectrophotometer (Varian). Steady-state emission spectra were obtained at room temperature using an Edinburgh Instruments FLS920 Spectrometer equipped with a Xe900 450W steady state xenon arc lamp, TMS300-X excitation monochromator, TMS300-M emission monochromator, Hamamatsu R2658P PMT detector and corrected for detector response. Lifetime measurements were obtained at room temperature and 77 K using an Edinburgh Instruments FLS920 Spectrometer equipped with Fianium SC400 Super Continuum White Light Source, Hamamatsu R3809U-50 Multi Channel Plate detector and data were analyzed with Edinburgh Instruments F900 software. Curve fitting of the data was performed using a non-linear least squares procedure in the F900 software. Absolute fluorescence quantum yield values were measured using an Edinburgh Instruments FLS92 calibrated integrating sphere S 3 system.

Chapter 3 : Stabilization of Ruthenium Sensitizers to TiO₂ surfaces through cooperative anchoring groups

3.1 Introduction

Based on the complexes developed in the previous Chapter it was observed that the molecular scaffold could be suitable for simultaneous binding through both the mesoionic carbene and terpy ligand. Simple molecular modification of the mesoionic carbene ligand and standard binding protocols through the terpy derivatives established for TiO₂ binding could lead to up to three binding sites for the complex. The Berlinguette group had become adept in constructing >7% efficient dye-sensitized solar cells (DSSC) based on decorated ruthenium metal complexes with visible-light-harvesting ligands (state-of-the-art cells were ~12% at the time 2012).¹⁴⁵⁻¹⁴⁷ The UV-vis spectra of the ruthenium compounds from the previous Chapter were not particularly impressive at absorbing light over the visible region. This property made them less than ideal as a light-harvesting chromophores, however the principle of simultaneous binding through both tridentate ligands would help the stability of DSSC by improving photodegradation due to ligand dissociation and hydrolysis from the surface. This motif offers advantageous binding geometry and addresses two major degradation pathways.

A series of ruthenium bistridentate complexes were designed with the intent to increase the stability of DSSC dyes via utilization of phosphonate and carboxylate binding groups. The results of this study were published in *Journal of the American Chemical Society (J. Am. Chem. Soc., 2013, 135, 1692–1695)* and form the bulk of Chapter 3.⁹⁷ I was first author and responsible for all of the synthesis and characterization of the compounds. Dr. Phil Schauer assisted me in the DRIFT analysis studies and in manuscript preparation. Brandon Fancy helped remake starting materials and Dr. Javier Borau-Garcia performed all the crystallographic analysis. I

worked in collaboration with my colleague Dr. Benjamin Schulze on a series of dyes exploring their potential in the DSSC that used a similar motif and those results were published in *Chemistry A European Journal* (*Chem. Eur. J.* 2013, 19, 14171 – 14180) and two articles in *Inorganic Chemistry* (*Inorg. Chem.*, **2014**, 53, 2083–2095 and *Inorg. Chem.*, **2014**, 53, 1637–1645).¹⁴⁸⁻¹⁵⁰ In these studies Dr. Schulze and I were responsible for constructing and testing all devices and relating performance to the molecular characterization data. Dr. Schulze was a visiting scientist in our lab and brought the synthesized dyes, while I constructed all the cells and tested all performances with his assistance over several weeks. I was involved in the preparation and writing of the manuscripts. The primary conclusion from the binding study was that using a combination of phosphonate and carboxylate anchoring groups showed, within the detection limits, no evidence of hydrolysis in aqueous media. Furthermore, that the carboxylate was shown to be critical for electron injection and thus *PCE*, although the overall achieved efficiencies (*PCE* = 0.2%) were somewhat unimpressive. Further work testing the ligand scaffold with Dr. Schulze in our three studies elucidated that poor device performances are likely attributed to enhanced recombination of injected electrons with oxidized dye molecules due to a dye regeneration issue with the electrolyte; however we were able to increase (*PCE* ~ 4%) efficiency by an order of magnitude over the dyes reported in the anchoring study (*PCE* ~ 0.3%).

3.2 Stabilization of Ruthenium Sensitizers to TiO₂ Surfaces Through Cooperative Anchoring Groups

Douglas G. Brown, Phil A. Schauer, Javier Borau-Garcia, Brandon F. Fancy, and Curtis P. Berlinguette*

3.2.1 Abstract

Cooperative binding of a *bis*(tridentate) ruthenium(II) complex to a TiO₂ surface through carboxylate and phosphonate groups is demonstrated to be an effective method for achieving a robust anchoring motif in aqueous media while maintaining efficient charge-transfer from the dye into the semiconductor. The realization of these complementary goals has broad implications for solar cells and (photo)electrocatalytic schemes.

3.2.2 Introduction

Among the suite of emerging photovoltaic (PV) technologies, the dye-sensitized solar cell (DSSC) is a promising option for penetration of the solar market. The long-term stability of the DSSC nonetheless remains a significant impediment to commercialization, due to issues with hermetic sealing of the liquid electrolyte and the consequent degradation and desorption of the dye.^{96,151-153} While recent advances in solid-state hole-transport materials (e.g., perovskites, polymers) have provided a viable pathway for bypassing liquid-phase electrolytes,^{154,155} charge-transport limitations have thus far confined performance to efficiencies of less than those of liquid electrolytes. The long-term stability of the sensitizer represents another critical problem.^{152,156} The current set of commercially relevant dyes that are related to [Ru(dcbpy)₂(NCS)₂] (dcbpy = 4,4'-dicarboxy-2,2'-bipyridine; **N3**) are susceptible to degradation through dissociation of the labile NCS⁻ ligands.¹⁵⁶ In recognition of these shortcomings, my research efforts (and others) have sought to replace these monodentate ligands with *chelating* bidentate and tridentate ligands without compromising device performance.^{122,157} A second key stability issue for conventional DSSCs is dye desorption from the TiO₂ surface caused by hydrolysis of the acids groups that bind the dye to the semiconductor, and/or competitive binding

with adventitious hydroxides. The electrolyte matrix in state-of-the-art devices thus requires rigorous exclusion of water to operate efficiently over prolonged periods of time. It would therefore be beneficial to use dyes with anchoring groups that are not compromised by water whilst maintaining efficient injection.

At least one carboxylate anchoring group is found within all of the high performance DSSC dyes in the literature because this substituent provide intimate electronic coupling between the dye and the TiO₂ semiconductor.⁹⁶ The aforementioned susceptibility of the carboxylate-TiO₂ linkage to hydrolysis is typically addressed by using aliphatic units to spatially “block” water/hydroxide from reaching the titania/carboxylate interface.^{158,159} Unfortunately, replacing the carboxylic acid group with alternate, more robust chemical functionalities (*e.g.* -B(OH)₂, -NO₂, -OH, -P(O)(OH)₂, -S(O)₂(OH), *etc.*) often introduces problems relating to dye aggregation and/or interfacial electronic phenomena.¹⁶⁰ The phosphonate functionality, for example, has received attention as an alternative to the carboxylate moiety owing to the five- to ten-fold increase in binding affinity for TiO₂, but the charge-injection times are compromised.¹⁶¹⁻¹⁶⁸

I therefore set out to take advantage of the efficient electron injection mediated by a carboxylate linker while simultaneously exploiting the phosphonate functionalities for increased surface binding stability. The underlying basis of this simple strategy is that the carboxylate moiety needs only to be positioned on the ligand that is involved in charge-transfer to the TiO₂, while the phosphonate moieties can be installed on an opposing side of the ligand that does not need to participate directly in the injection process. Four model complexes (Figure 3.1) were prepared containing a carboxylate anchoring group (**3.1** and **3.2**) or phosphonate groups (**3.3**), and a motif bearing both moieties (**3.4**) to demonstrate this strategy. It was found that the cooperative binding modes of **3.4** exhibit a significantly greater stability on TiO₂ relative to **N3**,

while also producing a higher efficiency in the DSSC relative to **3.1-3.3**. I contend this strategy will find broad use in a myriad of sensitization and catalytic applications where molecules are attached to semiconducting surfaces.

3.2.3 Results

Complexes **3.1-3.4** were each synthesized in a manner analogous to a previously published route⁸¹ with the final products isolated in moderate yields. The UV-*vis* absorption spectra of the corresponding ester derivatives that are denoted **3.1'-3.4'** (Figure 3.1), respectively, each reveal a metal-to-ligand charge-transfer (MLCT) band centered at *ca.* 460 nm with extinction coefficients on the order of $1.0 \times 10^4 \text{ M}^{-1} \text{ cm}^{-1}$ (Table 3.1). The frontier orbitals determined by DFT calculations indicate that the HOMO is predominantly of metal character (*ca.* 60%) with the balance of electron density residing more on the mesoionic carbene unit than the terpyridine ligand (See Appendix). The LUMOs of complexes **3.1'** and **3.2'** are clearly delocalized over the carboxy-terpyridine ligand, whereas the LUMO of **3.3'** is localized to the mesoionic carbene ligand due to the less electron-withdrawing (non-carboxy) terpyridine ligand. The orbital picture is not as clear in the case of **3.4'**, wherein the LUMO and LUMO+1 are calculated to be within 0.01 eV of each other and have alternate delocalization over the mesoionic carbene and carboxy-terpyridine ligands, respectively. Modeling the corresponding acid derivative, **3.4**, the unoccupied frontier orbitals exhibit a greater separation in energy (0.1 eV) with a LUMO localized to the polypyridyl ligand. These calculations indicate that complexes **3.1**, **3.2** and **3.4** are poised for electron injection through the anchoring carboxylate moieties.

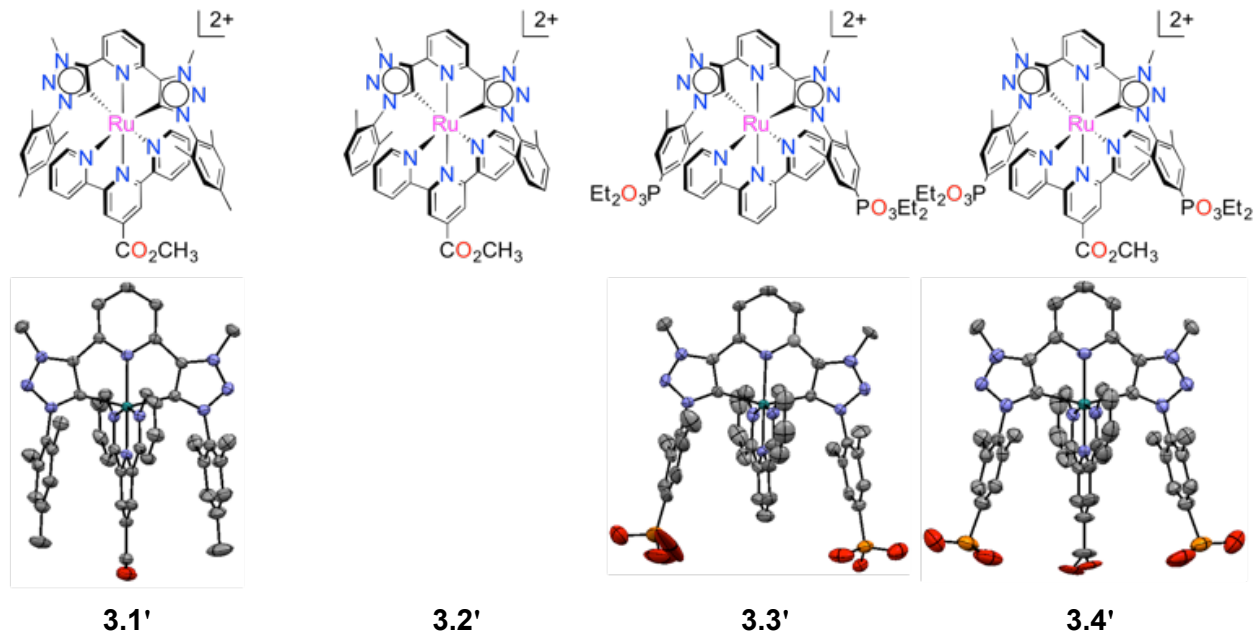


Figure 3.1 Ruthenium(II) complexes bearing carboxylate (**3.1** and **3.2**), phosphonate (**3.3**) and both (**3.4**) anchoring groups (counterion = BF_4^- in all cases). Single-crystal X-ray diffraction structural depictions of the ester derivatives **3.1'**, **3.3'** and **3.4'** are shown to illustrate that the phosphonate and/or carboxylate functional groups are geometrically positioned for simultaneous surface binding. Ellipsoids are shown at a 50% probability. Atom colors are given for carbon (grey), nitrogen (blue), oxygen (red), phosphorous (orange) and ruthenium (teal). Hydrogen atoms, anions, methylcarboxylate and diethylphosphonate ester linkages are omitted for clarity. See appendix for crystallographic data. Reprinted with permission from *J. Am. Chem. Soc.*, 2013, *135* (5), pp 1692–1695. Copyright 2017 American Chemical Society.

Table 3.1. Photophysical data for ester precursors 3.1'-3.4'.

	3.1'	3.2'	3.3'	3.4'
$\lambda_{\text{abs}}(\text{nm})^{a,b}$	472	469	458	461
$\epsilon(\times 10^4 \text{ M}^{-1} \text{ cm}^{-1})$	1.0	1.0	1.0	1.0
$\lambda_{\text{em}}(\text{nm})^c$	688	649	647	694
$\tau(\mu\text{s})^c$	1.72	7.38	6.02	2.12

^aMeasured in MeCN at 298 K. ^bMaximum absorption of lowest energy MLCT band. ^cMeasured in deaerated MeCN at 298 K. Reprinted with permission from *J. Am. Chem. Soc.*, 2013, 135 (5), pp 1692–1695. Copyright 2017 American Chemical Society.

The electrochemical and emission properties of **3.1'-3.4'** were measured to ensure that the ground- and excited-state energy levels were appropriately suited for electron injection and dye regeneration in the DSSC. Cyclic voltammograms recorded on the complexes in MeCN solutions revealed single reversible metal-based oxidation waves at 1.2-1.3 V vs. NHE (values indicated in Figure 3.2), with deviations commensurate with the number and positions of the acid groups. Square-wave voltammetry of the complexes bound to TiO₂ confirmed that the metal-based oxidative redox couples (See Appendix) were positively shifted relative to the relevant one-electron couple of the iodide-based electrolyte (*ca.* 0.8 V vs NHE for I⁻/I₂⁻)¹⁶⁹ and thus appropriately positioned for dye regeneration. The energy of the emitting state is found to be more negative than -0.70 V vs NHE for **3.1-3.3** (Figure 3.2), which is adequate for effective electron injection into TiO₂.⁹⁶ Complex **3.4** was determined to have an excited-state oxidation potential at -0.61 V, which may not be sufficiently negative to mediate injection into TiO₂. I

postulate that the long excited-state lifetime of the complex may render more efficient injection; experiments are underway to assess this scenario.

The photovoltaic performance parameters of devices containing each of the dyes bound to TiO₂ and iodide-based electrolytes were measured under simulated sunlight (Table 3.2). The absolute PCEs are not remarkable, which was expected due to the poor spectral coverage of each of the dyes, but the *trends* in the data provide indirect information about how charge collection is affected by the structures of the dyes. Devices sensitized by **3.4**, for example, exhibit a modest PCE of 0.2%, but the output is still much greater than that produced by **3.1** and **3.2**, and two orders of magnitude higher than that measured for **3.3**. The low PCE for **3.3** is likely due to the poorly positioned orbital character of the LUMO, which resides on the carbene fragment remote to the surface. The incident photon-to-current efficiency (IPCE) data followed the same trend. This data clearly shows that the phosphonate linkers attached to the carbene ligand do not facilitate meaningful light-induced charge transfer into the substrate despite energetics that are more conducive to the process. Spectrophotometric monitoring of dye uptake onto mesoporous TiO₂ substrates indicated similar dye loadings for **3.2** and **3.3** and enhanced dye loading for complex **3.4** (particularly rapid binding was observed for the dyes bearing the –PO₃[–] units), but the differences in data may be due to slightly lower surface coverage of **3.1-3.3** relative to that of **3.4** (which is also supported by the open-circuit voltages). Dye loading for **3.1** is particularly poor, which we attribute to the *para*-methyl groups of the mesityl moiety sterically interacting with the TiO₂ surface, thereby hindering formation of strong bidentate carboxylate linkages (*vide infra*). Notwithstanding, the dye with multiple anchoring groups does provide the best PCE of the series, providing convincing evidence that charge injection is mediated by the carboxylate moiety even with the phosphonates present.

We set out to confirm the nature of the surface attachment of the dyes by interrogating the binding modes through diffuse reflectance infrared fourier transform spectroscopy (DRIFTS) experiments. The spectra for dyes attached to TiO₂, denoted **3.1-3.4/TiO₂**, are presented in Figure 3.3 (an expansion of this data is provided in the appendix); data for **3.4** in a KBr powder (denoted **3.4/KBr**) is also provided as a benchmark. The spectrum of **3.4/TiO₂** clearly indicates the absence of $\gamma(\text{C-OH})$ and $\gamma(\text{C=O})$ stretching modes at 1200 cm⁻¹ and 1720 cm⁻¹, respectively, that are present for **3.4/KBr**, but does feature the characteristic carboxylate $\gamma_{\text{s}}(\text{CO}_2)$ and $\gamma_{\text{as}}(\text{CO}_2)$ modes at 1395 cm⁻¹ and 1630 cm⁻¹, respectively. The 235 cm⁻¹ difference between the symmetric and asymmetric carboxylate modes is consistent with a bidentate chelating/bridging attachment to the TiO₂ surface.^{162,170-173} Also evident from the spectrum of **3.4/KBr** are the $\gamma(\text{P-OH})$ (935 cm⁻¹) and $\gamma(\text{P=O})$ (1235 cm⁻¹) stretching modes, which are replaced in **3.4/TiO₂** with $\gamma_{\text{s}}(\text{PO}_3)$ (870 cm⁻¹) and $\gamma_{\text{as}}(\text{PO}_3)$ (1050 cm⁻¹) vibrations.^{162,174} The spectrum of **3.1/TiO₂** reveals similar $\gamma_{\text{s}}(\text{CO}_2)$ and $\gamma_{\text{as}}(\text{CO}_2)$ stretching modes to that observed for **3.4/TiO₂**, although the stretch at *ca.* 1700 cm⁻¹ is interpreted as a $\gamma(\text{C=O})$ mode thus confirming poor carboxylate binding for some proportion of the adsorbed dye molecules (which is corroborated with the poor dye loading and desorption studies). The carboxylate modes of **3.2/TiO₂** are analogous to those of **3.4/TiO₂**, whereas the phosphonate modes of **3.3/TiO₂** in the *ca.* 900-1100 cm⁻¹ range deviate to a fair extent offering little resolution of differing phosphonate-titania binding motifs for **3.3** and **3.4** (*vide infra*). Nonetheless, because the carboxylate and phosphonate binding modes measured for **3.4/TiO₂** were observed for **3.2/TiO₂** and **3.3/TiO₂**, respectively, and deviate from that of **3.4/KBr**, we conclude that all three acid groups of **3.4** do indeed bind to TiO₂ in a cooperative fashion.

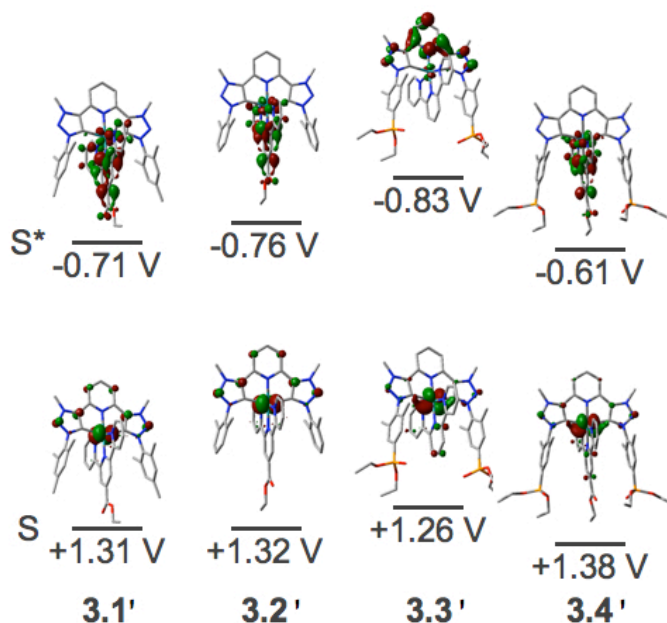


Figure 3.2. Energy level diagram for complexes **3.1'-3.4'**. The ground-state energy (S) corresponds to the oxidative redox couple determined by cyclic voltammetry in 0.1 M NBu₄BF₄/MeCN (internal standard: [Fc]⁺/[Fc]⁰ = +0.63 V vs NHE); the excited-state energy (S^{*}) corresponds to S + E₀₋₀ (E₀₋₀ = intersection point of the absorption and emission curves, where the latter is normalized to the lowest energy ¹MLCT band; see Appendix); HOMO and LUMO molecular orbitals (0.05 a.u.) of the singlet states are plotted as representations of S and S^{*}, respectively. (The nearly isogenic LUMO+1 for **3.4'** is shown because it is a better representation of the LUMO of **3.4**). Reprinted with permission from *J. Am. Chem. Soc.*, 2013, *135* (5), pp 1692–1695. Copyright 2017 American Chemical Society.

The dye loading of the complexes on titania was inferred from relative differences in UV-Vis absorption spectra (See appendix). In solution complexes **3.1'-3.4'** have essentially identical molar extinction coefficients ($1.0 \times 10^4 \text{ M}^{-1} \text{ cm}^{-1}$), and thus differences in absorption intensity for the dyed substrates **3.1-3.4/TiO₂** (on identical TiO₂/FTO anodes) may be correlated directly to

the dye loading. The dye-loading for the series follows the trend **3.1** < **3.2** < **3.3** < **3.4**. The similar footprints on the surface for each of the dyes indicate that the acid groups do influence the extent of dye loading. The low dye loading of **3.1** can be rationalized by the *para*-methyl substituents of the mesityl moiety bound to the carbene ligand providing a steric impediment to dye attachment to the surface. This conclusion is corroborated by the two-fold higher dye loading of **3.2**, in which the *para*-methyl groups are replaced by hydrogen atoms. The higher loading for **3.3** relative to **3.2** is presumably due to the presence of at least two surface-binding moieties in comparison to the single carboxylate functionality of **3.1** and **3.2**, while the dye-loading for the triply-binding **3.4** is the highest among the series. While **3.4**, which features both phosphonate and carboxylate binding groups, exhibits a two-fold or greater dye-loading relative to that of **3.1-3.3**, these differences do not fully account for the relative differences in *PCEs*. For reference a test device with no dye was constructed and had a *PCE* of 0.00001%.

Table 3.2. Photophysical and photovoltaic data obtained for the title complexes under AM1.5 conditions.

	3.1	3.2	3.3	3.4	N3
V_{oc} (V)	0.33	0.14	0.16	0.41	0.61
J_{sc} (mA/cm ²)	0.09	1.2	0.12	0.97	10.7
Fill Factor	0.46	0.36	0.35	0.50	0.59
<i>PCE</i> (%)	0.01	0.07	0.007	0.2	3.9

Current-voltage curves recorded under AM1.5 conditions on square titania anodes with an active area of 0.88 cm² (12 μm active) and E50 electrolyte (details in Experimental section). Reprinted

with permission from *J. Am. Chem. Soc.*, 2013, 135 (5), pp 1692–1695. Copyright 2017 American Chemical Society.

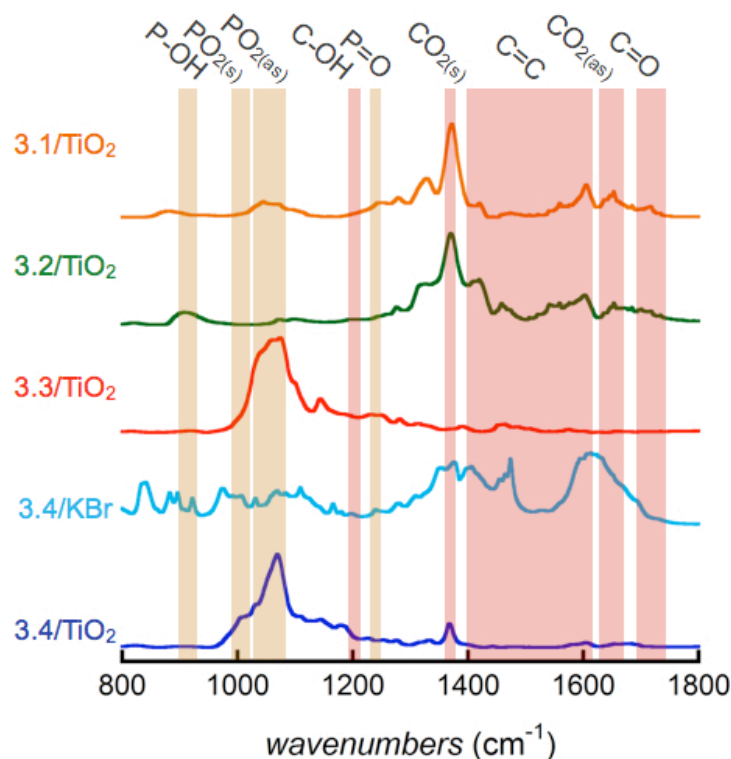


Figure 3.3. Kubelka-Munk DRIFTS spectra of **3.1-3.4/TiO₂** and **3.4/KBr**. Subscripts “s” and “as” represent symmetric and asymmetric, respectively. Reprinted with permission from *J. Am. Chem. Soc.*, 2013, 135 (5), pp 1692–1695. Copyright 2017 American Chemical Society.

Surface stability studies were carried out in the absence of Γ/I_3^- and in aqueous solution. The temporal stabilities of **3.1-3.4/TiO₂** submerged in water (in the dark) were measured by spectrophotometric monitoring of the respective MLCT bands to examine the benefit of the cooperatively binding phosphonate and carboxylate groups (Figure 3.4). It was found that *ca.* 80% of **1** desorbed from the surface within the first hour, although a slower rate of desorption was measured thereafter. This rapid desorption indicates a very weakly bound dye, plausibly due

to poor carboxylate binding on account of the mesityl methyl groups. Complex **3.2**, which enabled the carboxylate anchoring group to bind more strongly than **3.1**, showed *ca.* 55% surface desorption within 2 h. The rate of desorption for **3.3** was slower than that of **3.2**, yet still only half the original surface coverage was measured after 4 h. I had anticipated that a higher fraction of **3.3** would be maintained on the surface, although similar desorption rates at neutral pH have been documented for related systems bearing two phosphonate groups.^{164,165,168} It was therefore rewarding to find that **3.4/TiO₂** revealed no evidence of dye desorption over the same period of time. Indeed, the fraction of **3.4** on the surface was found to remain essentially static over 20 days under said conditions. This data indicates that the cooperative action of the three anchoring groups has a profound effect on stabilizing the dyes to the surface. In contrast, substrates stained with **N3** led to a loss of *ca.* 50% surface coverage within 2 h.

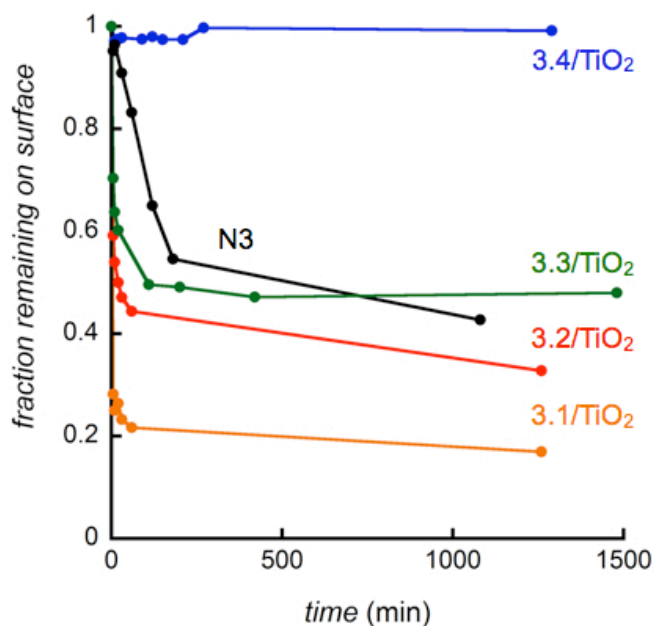


Figure 3.4. Temporal stability (pH 7.0) of **3.1-3.4/TiO₂** submerged in water. Data for **N3** is also shown so as to highlight the enhanced stability engendered by the cooperatively binding

anchoring groups of **3.4**. Reprinted with permission from *J. Am. Chem. Soc.*, 2013, *135* (5), pp 1692–1695. Copyright 2017 American Chemical Society.

This study demonstrates a simple molecular design strategy for exploiting the favorable properties of distinctive anchoring groups. The placement of carboxylates about the ligand responsible for electron injection and strongly binding phosphonates to the opposing ligand achieve both efficient charge injection and a robust dye/TiO₂ motif. This widely applicable strategy has far-reaching implications in the sensitization of semiconducting materials - particularly in aqueous media. Future studies will be focused on demonstrating this strategy in the context of (photo)electrocatalytic schemes (e.g., artificial photosynthesis) and to develop more strongly absorbing dyes in order to achieve higher PCEs in the DSSC.

3.3 Dye sensitized solar cell optimization and performance studies from collaboration

In this study I investigated the photophysical and electrochemical, as well as cell performances, of a series of dyes that looked at the viability of mesoionic carbene ligands in the DSSC. My initial investigation in Section 3.2 yielded poor performances in terms of cell efficiency with a recorded maximum of 0.2%, however it was unclear if this was an inherent design flaw in the ligand scaffold or the consequence of poor cell construction/conditions. As was stated in Section 3.1, I worked in collaboration in constructing test cells for several series of dyes that were divided into 3 separate papers, but one particular series probed the viability for DSSC of the mesoionic carbene ligand in great detail. The next series of dyes **3.5-3.7** shown in Figure 3.5 were synthesized along with their electrochemistry and photophysical properties characterized. Cyclic voltammetry was used to determine the ground state energy potential and

the excited states were determined by the intersection of the absorption and emission spectra with the later normalized to the lowest energy absorption. The results of this analysis were then compared to the conduction band edge of titania and the Γ/I_3^- electrolyte potential.

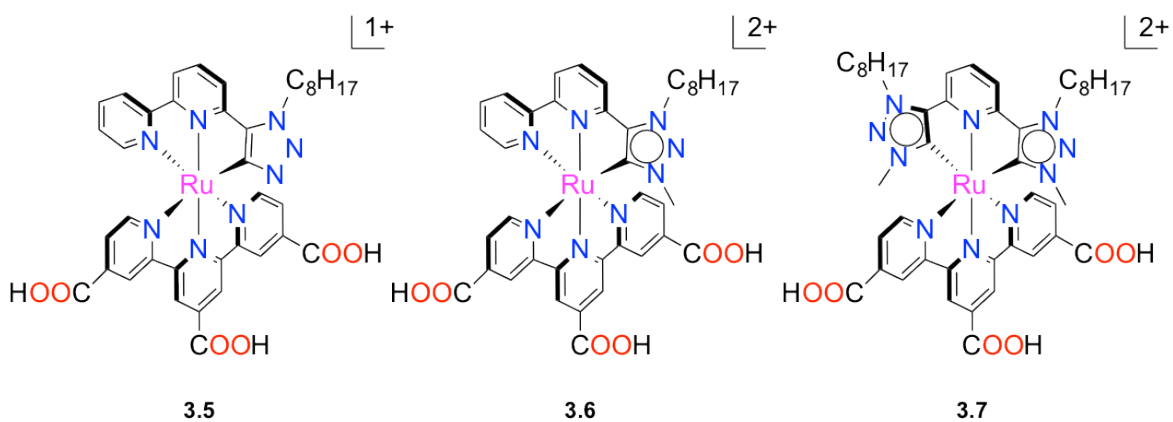


Figure 3.5 Series of dyes tested in the DSSC for device performance

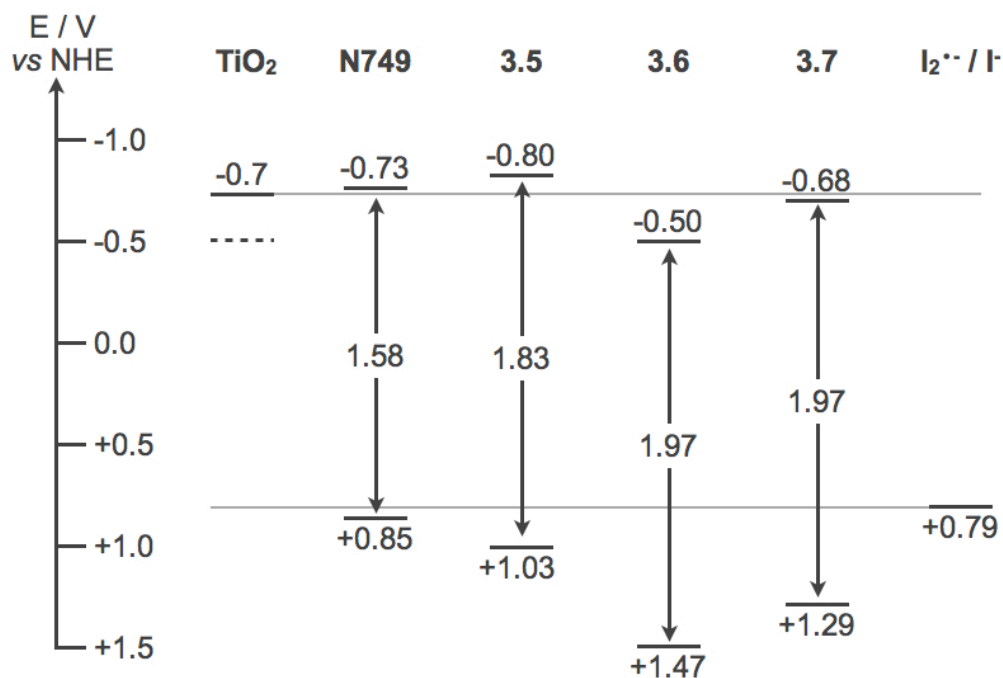


Figure 3.6 Comparison of the excited-state and ground state redox potentials (values refer to the NHE scale) with the relevant redox potential of the electrolyte and the conduction band edge (solid line) as well as the appropriate position of the Fermi level (dashed line) of TiO₂. Ground states determined by cyclic voltammetry. Excited states determined at the intersection of the absorption and emission spectra with the latter being normalized with respect to the lowest-energy absorption. Adapted with permission from *Inorg. Chem.*, 2014, 53 (4), pp 2083–2095. Copyright 2017 American Chemical Society.

The dyes were then tested under a variety of electrolyte conditions and optimized to yield modest solar cell performances under AM1.5 conditions, however still inferior to **N749** (Table 3.3). An increased lithium iodide concentration relative to **N749** was used in order to lower the conduction band of the titania to facilitate electron injection as some of the dyes had low-lying

excited states (Figure 3.6). Dye **3.6** suffered from injection problems as the excited state redox potential was well below the titania conduction band. Dyes **3.5** and **3.7** did not show any obvious design flaws and the poor performance was attributed to dye regeneration problems. In conclusion, ruthenium complexes featuring mesoionic carbene ligands do not seem to be well suited for the DSSC. A combination of poor light harvesting and regeneration are hindering *PCE*.

Table 3.3. Selected DSSC Data for the Ru(II) Complexes Measured under AM1.5 Light Conditions

Dye	$c(\text{Li}^+)/\text{M}$	V_{OC}/V	$J_{\text{SC}}/\text{mAcm}^{-2}$	FF	$PCE/\%$
3.5	1	0.44	5.0	0.61	1.4
3.6	1	0.38	1.9	0.61	0.5
3.7	1	0.42	3.7	0.61	1.0
N749	0.1	0.69	11.6	0.62	5.1

Adapted with permission from *Inorg. Chem.*, 2014, 53 (4), pp 2083–2095. Copyright 2017 American Chemical Society.

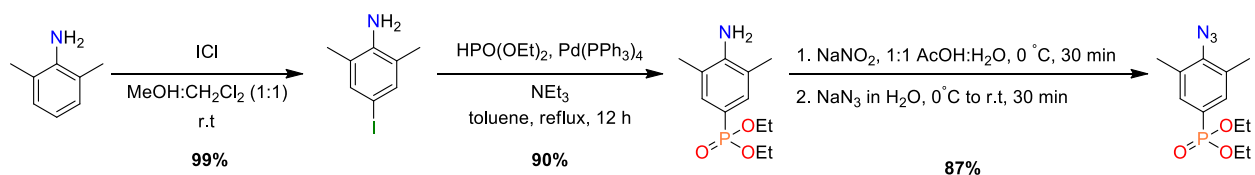
3.4 Experimental Details

3.4.1 Synthesis

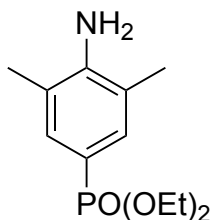
All manipulations were performed using analytical grade solvents (without stabilizer): chloroform (CHCl_3), toluene, dichloromethane (CH_2Cl_2), ethylacetate (EtOAc), acetonitrile (MeCN), ether (Et_2O), methanol (MeOH), hexanes and dimethylformamide (DMF). The compounds 4-iodo-2,6-dimethylaniline,¹⁷⁵ 2,6-diethynylpyridine,¹⁴² 2-azido-1,3,5-

trimethylbenzene,⁸¹ 2',6'-bis(1-mesityl-1,2,3-triazol-4-yl)pyridine,¹¹⁹ C[^]N[^]C-CH₃,¹¹⁹ Ag-C[^]N[^]C-CH₃,¹¹⁹ Ru(terpy)Cl₂DMSO,⁸¹ Ru(terpy-CO₂Me)Cl₂DMSO⁸¹ and **3.1**⁸¹ were synthesized according to literature procedures, whilst all remaining reagents were purchased from commercial suppliers and used as received. All reactions were performed in oven-dried flasks and were monitored by thin layer chromatography (TLC) on aluminum-backed sheets pre-coated with silica 60 F254 adsorbent (0.25 mm thick; Merck, Germany). Purification by column chromatography was carried out using silica (Silicycle: Ultrapure Flash Silica). ¹H and ¹³C NMR spectra were recorded at 400 MHz and 600 MHz, on Bruker Avance 400 MHz, Bruker Avance II 400 MHz, Bruker Avance III 400 MHz and Bruker Avance III 600 MHz instruments at 298 K. Chemical shifts (δ) are reported in parts per million (ppm) from low to high field and referenced to residual non-deuterated solvent. Elemental analysis (EA) and electrospray ionization (ESI) mass spectrometry data were collected at the University of Calgary using Perkin Elmer Model 2400 series II Elemental Analyzer and Agilent 6520 Q-ToF Mass Spectrometers, respectively.

Safety Comment. *Sodium azide is very toxic and personal protection precautions must be taken!* As low molar mass organic azides are potential explosives, care must be taken during their handling. All azide experiments were conducted with ice chilled aqueous solutions of sodium nitrate and sodium azide and added dropwise behind a blast shield.



Scheme 3.1 Synthesis of azido phosphonate

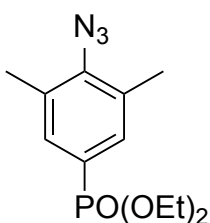


Synthesis of diethyl (4-amino-3,5-dimethylphenyl)phosphonate (3.8). To a solution of 4-iodo-2,6-dimethylaniline¹⁷⁵ (3.00 g, 12.1 mmol) in degassed anhydrous toluene (12 ml) was added diethyl phosphite (8.0 mL, 62 mmol), Et₃N (6.0 mL, 43 mmol) and Pd(PPh₃)₄ (1.4 g, 1.2 mmol). The reaction mixture was refluxed under nitrogen and, after 12 h, the precipitate was filtered and washed with EtOAc. The filtrate was diluted with water (30 mL) and extracted with EtOAc (3 × 30 mL). The combined organic phases were subsequently washed with water (3 × 20 mL) and brine (3 × 20 mL), dried over MgSO₄ and the solvent evaporated to afford a yellow oil. The crude reaction mixture was purified by column chromatography on silica (gradient elution with hexanes/EtOAc from 100% hexanes to 100% EtOAc) to obtain the pure product as a yellow oil (2.95 g, 90%). ¹H NMR (400 MHz, CDCl₃, ppm) δ 7.30 (d, *J*=13.3 Hz, 2H), 6.05 (bs, 2H), 4.07 – 3.92 (m, 4H), 2.12 (s, 6H), 1.24 (t, *J*= 7.1 Hz, 6H); ¹³C {¹H} NMR (101 MHz, CDCl₃, ppm) δ 146.63 (d, *J*= 3.2 Hz), 131.97 (d, *J*= 11.1 Hz), 128.58 (d, *J*= 12.3 Hz), 121.51 (d, *J*= 16.5 Hz), 115.53, 113.57, 61.84 (d, *J*= 5.2 Hz), 17.38, 16.24 (d, *J*= 6.6 Hz).

General procedure for conversion of amine to azide.

To a cooled mixture (0 °C) of the **amine** in 1:1 v/v AcOH:H₂O (20 mL) was added a saturated aqueous solution of NaNO₂ (1.5-2 eq.). After complete consumption of the starting material (30-60 min), a saturated aqueous solution of NaN₃ (1.5-2 eq) was added drop-wise to the reaction mixture at 0 °C, and the resulting mixture subsequently warmed to room temperature and stirred

for a further 30-60 min. The reaction mixture was diluted with water (30 mL) and Et₂O (30 mL), and solid Na₂CO₃ was slowly added until the pH of the aqueous phase was approximately neutral. The phases were separated, and the aqueous phase extracted with additional Et₂O (2 × 30 mL). The combined organic phases were washed with water (20 mL) and brine (20 mL), dried over MgSO₄ and evaporated to dryness by rotary evaporation. The product thus obtained was subsequently utilised without further purification.

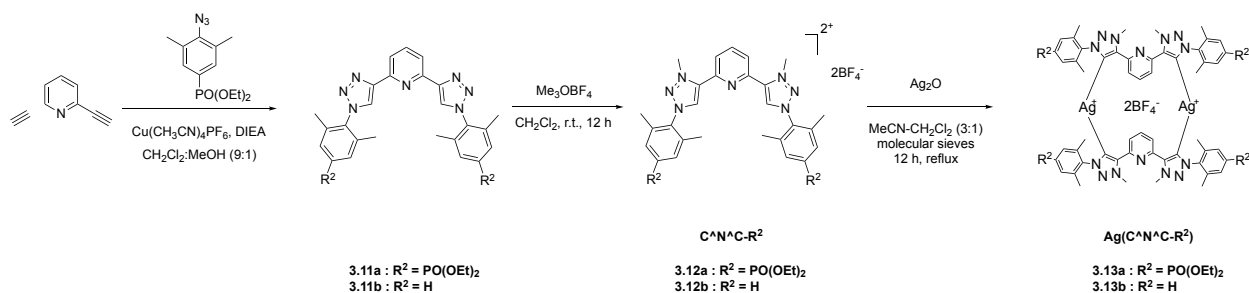


Diethyl(4-azido-3,5-dimethylphenyl)phosphonate (3.9). Diethyl(4-amino-3,5-dimethylphenyl)phosphonate (3.1 g, 12 mmol), NaNO₂ (1.67 g, 24.1 mmol) and NaN₃ (3.06 g, 24.1 mmol) afford **3.9** as a yellow oil (2.9 g, 86%). ¹H NMR (400 MHz, CDCl₃, ppm) δ 7.45 (d, *J* = 13.4 Hz, 2H), 4.22 – 3.97 (m, 4H), 2.39 (d, *J* = 0.5 Hz, 6H), 1.31 (td, *J* = 7.1, 0.3 Hz, 6H); ¹³C {¹H}NMR (101 MHz, CDCl₃, ppm) δ 141.01 (d, *J* = 3.9 Hz), 132.51 (d, *J* = 10.2 Hz), 132.39, 132.27 (d, *J* = 9.9 Hz), 128.66 (d, *J* = 12.2 Hz), 62.34 (d, *J* = 5.4 Hz), 18.30, 16.45 (d, *J* = 6.5 Hz).



2-Azido-1,3-dimethylbenzene (3.10). 2,6-Dimethylaniline (3.04 g, 25.0 mmol), NaNO₂ (2.59 g, 37.5 mmol) and NaN₃ (4.73 g, 37.2 mmol) afford **3.10** as a yellow oil (2.49 g, 68%). ¹H NMR

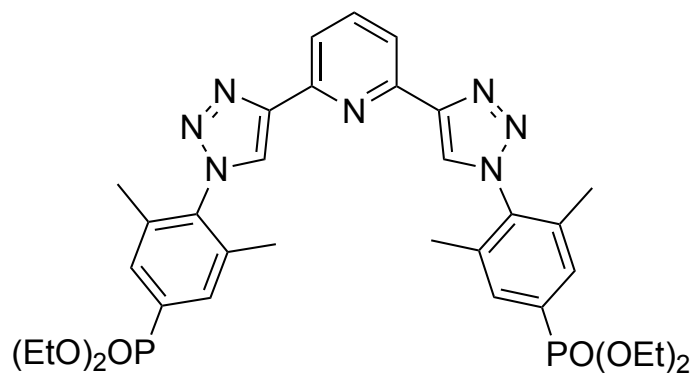
(400 MHz, CDCl₃, ppm) δ 7.14 (m, 3H), 2.52 (s, 6H); ¹³C{¹H} NMR (101 MHz, CDCl₃, ppm) δ 136.93, 131.98, 128.83, 125.63, 17.95.



Scheme 3.2. Synthesis of the transmetallating reagent (Ag-C^NC-R²)

General Procedure for copper-catalyzed cyclization reaction

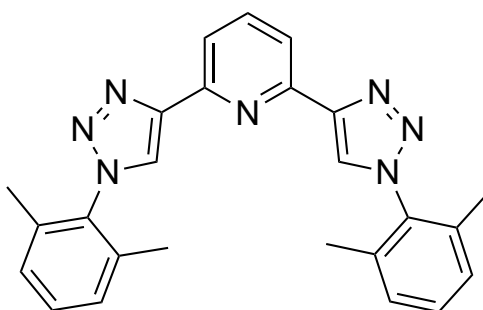
To a solution of the **azide** (2 eq.), 2,6-diethynylpyridine (1 eq.) and *N,N*-diisopropylethylamine (~2 eq.) in 9:1 v/v CH₂Cl₂/MeOH (50 mL) was added [Cu(CH₃CN)₄]PF₆ (0.2 eq.). The resulting mixture was stirred at room temperature for 48 h, followed by removal of solvent under reduced pressure to yield a residue requiring further purification as detailed below.



2,6-Bis(1-(2,6-dimethyl-4-phosphonyl phenyl)-1H-1,2,3-triazol-4-yl)pyridine (3.11a).

Compound **3.9** (1.20 g, 4.24 mmol), 2,6-diethynylpyridine (0.300 g, 2.07 mmol) and *N,N*-

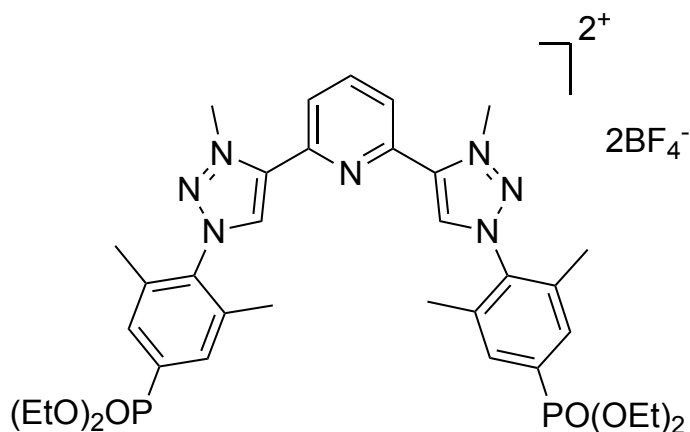
diisopropylethylamine (1.00 mL, 5.74 mmol). The residue was suspended in EtOAc (5-10 mL), sonicated for 5-10 min to yield the pure product as a white solid that was collected by vacuum-filtration (1.22 g, 85%). ^1H NMR (400 MHz, CDCl_3 , ppm) δ 8.26 (s, 2H), 8.25 (d, $J = 7.8$ Hz, 2H), 7.98 (t, $J = 7.9$ Hz, 1H), 7.66 (d, $J = 13.4$ Hz, 4H), 4.35 – 4.02 (m, 8H), 2.12 (s, 12H), 1.36 (t, $J = 7.1$ Hz, 12H). $^{13}\text{C}\{^1\text{H}\}$ NMR (101 MHz, CDCl_3 , ppm) δ 149.89, 148.68, 138.25, 136.28 (d, $J = 15.9$ Hz), 131.97 (d, $J = 10.0$ Hz), 131.72, 123.90, 119.92, 62.67 (d, $J = 5.6$ Hz), 17.67, 16.50 (d, $J = 6.4$ Hz). HRMS (ESI-ToF, m/z): 694.2642 ($[\text{M}+\text{H}]^+$), $\text{C}_{33}\text{H}_{42}\text{N}_7\text{O}_6\text{P}_2^+$ requires 694.2666.



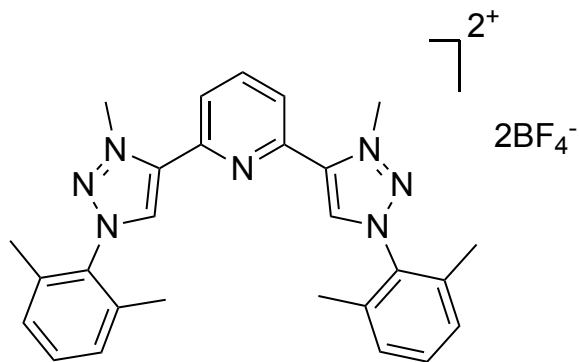
2,6-bis(1-(2,6-dimethylphenyl)-1H-1,2,3-triazol-4-yl)pyridine (3.11b). Compound 3.7 (0.972 g, 6.60 mmol), 2,6-diethynylpyridine (0.502 g, 3.46 mmol) and *N,N*-diisopropylethylamine (1.2 mL, 6.9 mmol). The residue was filtered through a silica plug (2.5 cm) with 1:1 v/v EtOAc: CH_2Cl_2 (1:1) and the resulting solution was evaporated to dryness to afford a white solid (1.39 g, 95%). ^1H NMR (400 MHz, CDCl_3 , ppm) δ 8.26 (s, 2H), 8.25 (d, $J = 7.9$ Hz, 2H), 7.97 (t, $J = 7.9$ Hz, 1H), 7.36 (t, $J = 7.6$ Hz, 2H), 7.20 (d, $J = 7.7$ Hz, 4H), 2.07 (s, 12H). $^{13}\text{C}\{^1\text{H}\}$ NMR (101 MHz, CDCl_3) δ 150.09, 148.41, 138.02, 135.96, 135.50, 130.21, 128.93, 128.56, 124.12, 119.57, 77.16, 17.51. HRMS (ESI-ToF, m/z): 422.2084 ($[\text{M}+\text{H}]^+$), $\text{C}_{25}\text{H}_{24}\text{N}_7^+$ requires 422.2088.

General procedure for selective methylation.

A 50 mL Schlenk flask was charged with dry CH₂Cl₂ (15 mL), triazole **3.11** and [Me₃O]BF₄ (2.1 eq.), and the mixture stirred under nitrogen for 12 h at room temperature. The resulting reaction mixture was evaporated to dryness to obtain a yellow oil. To remove unreacted oxonium salt, the crude mixture was suspended in MeOH and all volatiles were removed *in vacuo*. The residue was then dissolved in a minimal amount of MeCN (~ 5 mL) and added dropwise to a large volume of Et₂O (~ 100 mL) to obtain a solid product.



4,4'-(pyridine-2,6-diyl)bis(1-(2,6-dimethyl-4-phosphonyl benzyl)-3-methyl-1H-1,2,3-triazol-3-ium) tetrafluoroborate, C^NC-PO₃Et₂ (3.11a**).** Compound **3.11a** (1.00 g, 1.45 mmol) and Me₃O•BF₄ (0.559 g, 3.78 mmol) afford a white solid that was used without further purification (1.19 g, 91%). ¹H NMR (400 MHz, CD₃CN) δ 9.06 (s, 2H), 8.41 (dd, *J* = 8.3, 7.7 Hz, 1H), 8.21 (d, *J* = 8.0 Hz, 2H), 7.79 (d, *J* = 13.2 Hz, 4H), 4.69 (s, 6H), 4.23 – 4.09 (m, 8H), 2.26 (s, 12H), 1.34 (t, *J* = 7.0 Hz, 12H). ¹³C{¹H} NMR (101 MHz, CD₃CN) δ 143.45, 141.35, 140.58, 132.53 – 132.20 (m), 131.82, 127.36, 41.55, 16.65, 15.57–15.34 (m).

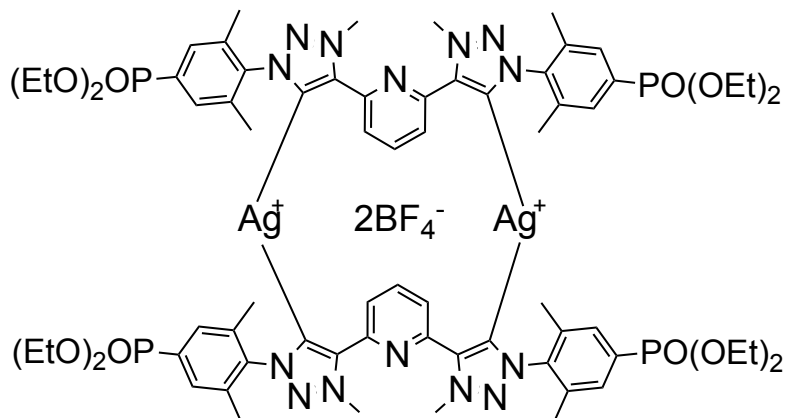


4,4'-(pyridine-2,6-diyl)bis(1-(2,6-dimethylphenyl)-3-methyl-1H-1,2,3-triazol-3-ium)

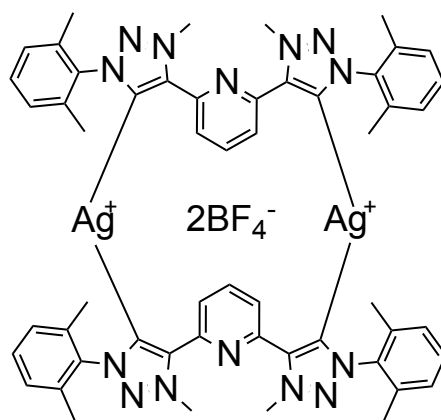
tetrafluoroborate, C⁺N⁺C-H (3.12b). Compound **3.11b** (1.30 g, 3.08 mmol) and [Me₃O]BF₄ (1.00 g, 6.76 mmol) afford a residue that was further suspended in EtOAc and filtered to afford a white solid (1.81 g, 94%). ¹H NMR (400 MHz, CD₃CN) δ 9.09 (s, 2H), 8.41 (dd, *J* = 8.4, 7.5 Hz, 1H), 8.24 (d, *J* = 8.0 Hz, 2H), 7.65 – 7.53 (m, 2H), 7.47 – 7.37 (m, 4H), 4.71 (s, 6H), 2.21 (s, 12H). ¹³C{¹H} NMR (101 MHz, CD₃CN) δ 144.64, 142.16, 141.55, 136.26, 134.74, 133.43, 132.99, 130.34, 128.23, 118.35, 42.41, 17.51.

General procedure for formation of the silver carbene complex.

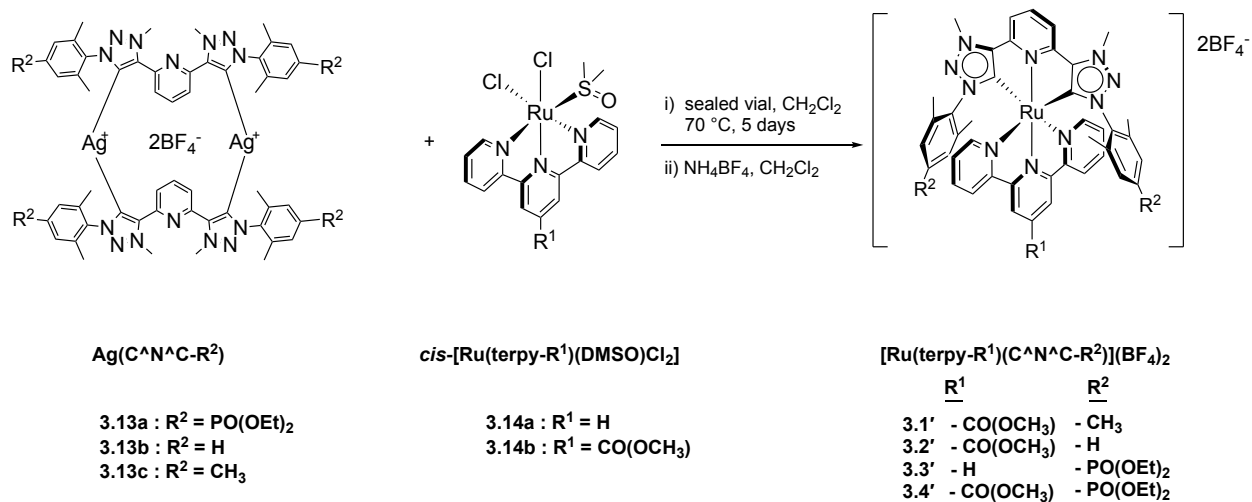
A 50-mL Schlenk flask was charged with dry degassed CH₂Cl₂ (20 mL), methylated product **3.12**, freshly prepared¹⁷⁶ Ag₂O (2 eq.) and activated 4 Å molecular sieves. The resulting mixture was protected from light and refluxed under nitrogen for 12 h. After cooling to room temperature, the reaction mixture was filtered through celite and the solvent evaporated. The residue was redissolved in a minimum volume of MeCN (~ 5 mL) and precipitated by drop-wise addition to stirred Et₂O (~ 100 mL), vacuum-filtration affording the solid product which was utilised without further purification.



Ag-C^NC-PO₃Et₂ (3.13a). Compound **3.12a** (1.0 g, 1.1 mmol) and Ag₂O (0.39 g, 1.7 mmol) affords **3.13a** as a gray solid (1.0 g, 100%). ¹H NMR (400 MHz, CD₃CN, ppm) δ 8.16 (d, *J* = 7.9 Hz, 2H), 7.93 (t, 7.9, 1H), 7.73 (d, *J* = 13.3 Hz, 4H), 4.46 (s, 6H), 4.28 – 4.18 (m, 8H), 1.83 (s, 12H), 1.38 (t, *J* = 7.1 Hz, 12H). HRMS (ESI-ToF, *m/z*): 828.1957 ([M-2BF₄]²⁺), C₇₀H₉₀Ag₂N₁₄O₁₂P₄²⁺ requires 828.1952.



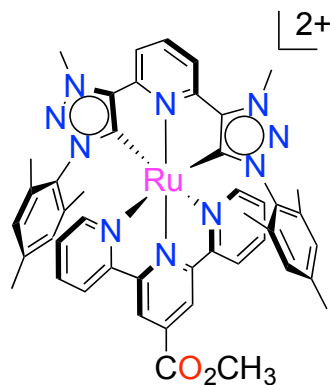
Ag-C^NC-H (3.13b). Compound **3.12b** (0.83 g, 1.3 mmol) and Ag₂O (0.55 g, 2.4 mmol) affords **3.13b** as a white solid (680 mg, 80%). ¹H NMR (400 MHz, CD₃CN, ppm) δ 8.20 (d, *J* = 7.8 Hz, 2H), 7.95 (t, *J* = 8.0 Hz, 1H), 7.48 (t, *J* = 7.5 Hz, 2H), 7.22 (s, 4H), 4.45 (s, 6H), 1.38 (s, 12H). ¹³C{¹H} NMR (151 MHz, CD₃CN) δ 170.98, 169.79, 148.76, 147.60, 139.80, 139.34, 135.27, 131.85, 129.88, 125.64, 40.57, 17.56. HRMS (ESI-ToF, *m/z*): 1198.2804 ([M-BF₄]⁺), C₅₄H₅₄Ag₂BF₄N₁₄⁺ requires 1198.2818.



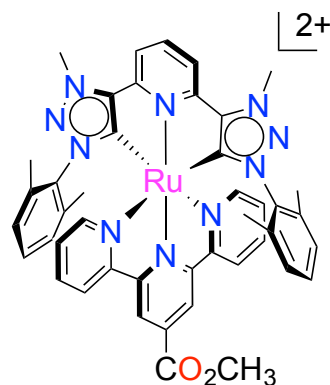
Scheme 3.3. Synthesis of mesoionic carbene complexes

General procedure for transmetalation complexation

A 20-mL glass vial was charged with dry degassed CH₂Cl₂ (10 mL), *cis*-[Ru(terpy-R¹)(DMSO)Cl₂] (2 eq.) and Ag-C^NC-R² (1 eq.), purged with nitrogen gas for 20 min. then sealed and covered with foil to exclude ambient light. The vessel was placed in a 70°C oil-bath for five days, then cooled to room temperature and treated with excess NH₄BF₄ (5 eq.). After stirring for a further 90 min the suspension was filtered, the residue washed with additional CH₂Cl₂ and the resulting dark-red solution evaporated to dryness. The crude product was purified by vapor-diffusion crystallization (MeCN/Et₂O).

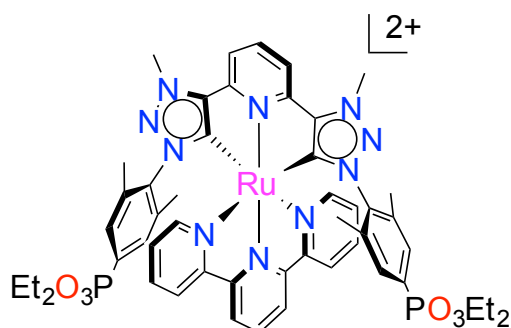


Ru(terpy-CO(OCH₃))(C[^]N[^]C-CH₃) (R¹ = CH₃; R² = CO(OCH₃)) (3.1'). *cis*-[Ru(terpy-CO(OCH₃))(DMSO)Cl₂] (57.2 mg, 0.106 mmol) and **3.10c**¹¹⁹ (44.1 mg, 32.8 μmol) afford **3.1'** (24 mg, 35%). ¹H NMR (600 MHz, CD₃CN, ppm) δ 8.47 – 8.30 (m, 5H), 8.26 (dd, *J* = 8.8, 7.5 Hz, 2H), 8.21 – 8.15 (m, 2H), 7.93 – 7.88 (m, 2H), 7.55 (d, *J* = 4.9 Hz, 2H), 7.28 – 7.23 (m, 2H), 6.43 (s, 4H), 4.52 (s, 6H), 4.10 (s, 3H), 2.04 (s, 6H), 0.70 (s, 12H); ¹³C{¹H} NMR (151 MHz, CD₃CN, ppm) δ 183.04, 156.46, 153.17, 152.64, 151.54, 146.85, 140.52, 137.38, 136.34, 133.69, 133.61, 130.20, 128.34, 126.59, 123.45, 120.09, 118.94, 65.25, 52.77, 38.84, 19.81, 14.60, 14.52; HRMS (ESI-ToF, *m/z*): 957.2720 ([M-BF₄]⁺), C₄₆H₄₄BF₄N₁₀O₂Ru⁺ requires 957.2710. Anal Calcd for C₄₆H₄₄B₂F₈N₁₀O₂Ru: C, 52.94; H, 4.25; N, 13.42; Found: C, 52.90; H, 4.22; N, 13.38

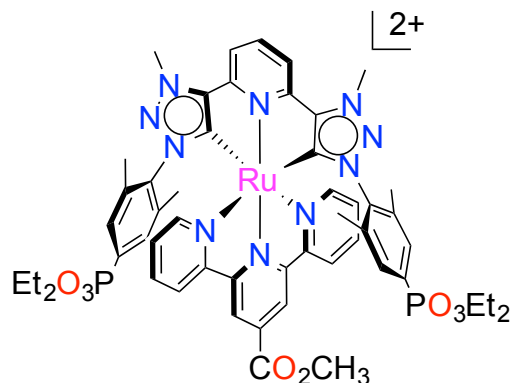


Ru(terpy-CO(OCH₃))(C[^]N[^]C-H) (R¹ = CO(OCH₃); R² = H) (3.2'). *cis*-[Ru(terpy-CO(OCH₃))(DMSO)Cl₂] (93.2 mg, 0.172 mmol) and **3.10b** (101 mg, 0.0784 mmol) afford **3.2'**

(19 mg, 12%). ^1H NMR (400 MHz, CD_3CN) δ 8.33 – 8.29 (m, $J = 7.9$ Hz, 2H), 8.29 – 8.18 (m, 4H), 7.95 – 7.87 (m, 2H), 7.58 (d, $J = 4.9$ Hz, 2H), 7.30 – 7.24 (m, 2H), 6.91 (t, $J = 7.7$ Hz, 2H), 6.63 (d, $J = 7.7$ Hz, 4H), 4.53 (s, 6H), 4.10 (s, 3H), 0.76 (s, 12H). $^{13}\text{C}\{^1\text{H}\}$ NMR (101 MHz, CD_3CN) δ 183.56, 157.47, 154.12, 153.76, 152.54, 148.00, 138.43, 137.46, 137.11, 135.13, 131.10, 130.35, 128.90, 127.69, 124.47, 121.17, 120.07, 66.29, 39.92, 15.63. HRMS (ESI-ToF, m/z): 418.1197 ($[\text{M}-2\text{BF}_4]^{2+}$), $\text{C}_{44}\text{H}_{40}\text{N}_{10}\text{O}_2\text{Ru}^{2+}$ requires 418.12004. Anal Calcd for $\text{C}_{44}\text{H}_{40}\text{B}_2\text{F}_8\text{N}_{10}\text{O}_2\text{Ru}\cdot\text{H}_2\text{O}$: C, 51.13; H, 4.10; N, 13.55; Found: C, 51.08; H, 3.79; N, 13.76



Ru(terpy)C^NC-PO₃Et₂ (R¹ = H; R² = PO₃Et₂) (3.3'). *cis*-[Ru(terpy-H)(DMSO)Cl₂] (11.8 mg, 24.4 μmol) and **3.10a** (22.9 mg, 12.4 μmol) afford **3.3'** (12.9 mg, 43%). ^1H NMR (600 MHz, CD_3CN) δ 8.27 – 8.18 (m, 3H), 8.17 (ddd, $J = 8.1, 1.3, 0.8$ Hz, 2H), 7.87 (ddd, $J = 8.1, 7.5, 1.5$ Hz, 2H), 7.77 (d, $J = 8.1$ Hz, 2H), 7.53 (ddd, $J = 5.6, 1.5, 0.8$ Hz, 2H), 7.45 (dd, $J = 9.7, 6.4$ Hz, 1H), 7.21 (ddd, $J = 7.4, 5.6, 1.3$ Hz, 2H), 7.07 – 7.01 (dt, $J = 13.2, 0.6$ Hz, 4H), 4.54 (s, 6H), 4.15 – 4.01 (m, 8H), 1.39 – 1.32 (dt, $J = 7.0, 0.4$ Hz, 12H), 0.85 (d, $J = 0.6$ Hz, 12H); $^{13}\text{C}\{^1\text{H}\}$ NMR (151 MHz, CD_3CN) δ 183.87, 157.69, 153.86, 153.66, 152.80, 148.48, 140.27, 137.67, 137.40, 135.96 (d, $J = 15.8$ Hz), 132.72, 131.77 (d, $J = 9.9$ Hz), 127.45, 124.16, 122.11, 119.97, 63.28 (d, $J = 5.7$ Hz), 16.80 (d, $J = 6.2$ Hz), 15.69. HRMS (ESI-ToF, m/z): 525.1437 ($[\text{M}-2\text{BF}_4]^{2+}$), $\text{C}_{50}\text{H}_{56}\text{N}_{10}\text{O}_6\text{P}_2\text{Ru}^{2+}$ requires 525.1462. Anal Calcd for $\text{C}_{50}\text{H}_{56}\text{B}_2\text{F}_8\text{N}_{10}\text{O}_6\text{Ru}\cdot\text{H}_2\text{O}$: C, 48.13; H, 4.69; N, 11.23; Found: C, 48.38; H, 4.68; N, 11.20



Ru(terpy-CO(OCH₃))(C^NC-PO₃Et₂) (R¹ = CO(OCH₃); R² = PO₃Et₂) (3.4'). *cis*-[Ru(terpy-CO(OCH₃))(DMSO)Cl₂] (42 mg, 78 μmol) and **3.10a** (52 mg, 30 μmol) afford **3.4'** (21 mg, 22%). ¹H NMR (600 MHz, CD₃CN, ppm) δ 8.36 – 8.28 (m, 5H), 8.26 – 8.23 (m, 2H), 7.97 – 7.91 (m, 2H), 7.65 – 7.60 (m, 2H), 7.33 – 7.28 (m, 2H), 7.03 (d, *J* = 13.2 Hz, 4H), 4.56 (s, 6H), 4.15 – 3.96 (m, 8H), 1.34 (dt, *J* = 7.3, 3.6 Hz, 12H), 0.84 (d, *J* = 0.4 Hz, 12H); ¹³C{¹H}NMR (151 MHz, CD₃CN, ppm) δ 183.19, 164.58, 157.26, 154.18, 153.99, 152.44, 148.32, 140.01, 139.98, 138.61, 137.73, 136.07, 135.97, 133.40, 133.01, 132.98, 132.17, 131.80, 131.73, 131.55, 131.48, 127.94, 124.70, 124.67, 121.00, 120.30, 118.36, 63.34, 63.30, 53.82, 40.09, 16.79, 16.75, 15.68; HRMS (ESI-ToF, *m/z*): 1201.2961 ([M-BF₄]⁺), C₅₂H₅₈BF₄N₁₀O₈P₂Ru⁺ requires 1201.2976. Anal Calcd for C₅₂H₅₈B₂F₈N₁₀O₈Ru•H₂O: C, 47.83; H, 4.63; N, 10.73; Found: C, 47.76; H, 4.56; N, 10.74

General procedure for saponification

The ester complexes were each refluxed in a mixture of DMF:H₂O:Et₃N (1:1:3 v/v) for 3 days, with evaporation of solvent quantitatively affording the saponified product. Saponification was confirmed by monitoring the disappearance of ¹H-NMR spectroscopic resonances attributable to the ester alkyl chains.

3.4.2 Physical Methods

Electrochemical measurements were performed under anaerobic conditions with a Princeton Applied Research VersaStat 3 potentiostat using dry solvents, Pt working and counter electrodes, a Ag pseudoreference electrode, and 0.1 M NBu_4BF_4 supporting electrolyte. Electronic spectroscopic data were collected in MeCN solutions using a Cary 5000 UV-vis spectrophotometer. Steady-state emission spectra were obtained at room temperature using an Edinburgh Instruments FLS920 Spectrometer equipped with a Xe900 450W steady state xenon arc lamp, TMS300-X excitation monochromator, TMS300-M emission monochromator, Hamamatsu R2658P PMT detector and corrected for detector response. Lifetime measurements were obtained at room temperature using an Edinburgh Instruments FLS920 Spectrometer equipped with Fianium SC400 Super Continuum White Light Source, Hamamatsu R3809U-50 Multi Channel Plate detector and data were analyzed with Edinburgh Instruments F900 software. Curve fitting of the data was performed using a non-linear least squares procedure in the F900 software. The instrument was controlled and analyzed by the program “Resolutions pro”. FT-IR data was collected on a Varian 7000 FT-IR instrument with a diffuse reflectance accessory, and all data is reported as Kubelka Munk and manipulated within the program.

Cell Fabrication. Photoanodes were prefabricated by Dyesol, Inc. (Australia) with a screen-printable TiO_2 pastes (18-NRT and WER4-O, Dyesol™). The active area of the TiO_2 electrode is 0.88 cm^2 with a thickness of $12 \mu\text{m}$ (18-NRT) on fluorine-doped tin-oxide (FTO; TEC8 ($8 \Omega \text{ cm}^{-2}$)). TiO_2 substrates were treated with $\text{TiCl}_{4(\text{aq})}$ (0.05 M) at $70 \text{ }^\circ\text{C}$ for 30 min and subsequently rinsed with H_2O and EtOH and dried prior to heating. The electrodes were heated to $450 \text{ }^\circ\text{C}$ for

20 min under ambient atmosphere and allowed to cool to 80 °C before dipping into the dye solution. The anode was soaked overnight for 16 h in a MeOH solution containing dye (~0.25 mM). The stained films were rinsed copiously with MeOH and dried. The cells were fabricated using Pt-coated counter-electrode (FTO TEC-15 ($15 \Omega \text{ cm}^{-2}$)) and sealed with a 30 μm Surlyn (Dupont) gasket by resistive heating. An MeCN based electrolyte solution: (**E50**: 1.0M lithium iodide, 0.6 M butylmethylimidazolium iodide, 0.06 M I_2 , 0.1 M guanidinium thiocyanate and 0.5 M *tert*-butylpyridine in MeCN) was introduced to the void via vacuum backfilling through a hole in the counter electrode. The hole was sealed with an aluminum-backed Bynel foil (Dyesol). After sealing, silver bus bars were added to all cells.

Dye Desorption Studies. Photoanodes of **3.1-3.4/TiO₂** were prepared according to the method described in the cell fabrication section. The dye soaked films were desorbed with pH 7 deionized water. The UV-vis absorption intensity of the ¹MLCT band centered at approximately 460 nm was monitored as a function of time.

DRIFTS Studies. Photoanode substrates were prepared on a 0.28 cm² active area (12 μm), in the fashion as described above. Prior to acquisition of spectra the samples were heated at 120 °C for 24 h.

Cell Characterization. Photovoltaic measurements were recorded with a Newport Oriel solar simulator (Model 9225A1) equipped with a class A 150 W xenon light source powered by a Newport power supply (Model 69907). The light output (area = 5 cm × 5 cm) was calibrated to AM 1.5 using a Newport Oriel correction filter to reduce the spectral mismatch in the region of

350-700 nm to less than 1.5%. The power output of the lamp was calibrated to 1 Sun (100 mW cm^{-2}) using a certified Si reference cell. Neutral density filters were used to achieve lamp outputs between $10\text{-}100 \text{ mW cm}^{-2}$. The current-voltage ($I\text{-}V$) characteristic of each cell was obtained by applying an external potential bias to the cell and measuring the generated photocurrent with a Keithley digital source meter (Model 2400). All cells were measured with a mask size of 0.88 cm^2 . IPCE measurements were performed on a QEX7 Solar Cell Spectral Response Measurement System from PV Instruments, Inc. The system was calibrated with a photodiode that was calibrated against NIST standard I755 with transfer uncertainty less than 0.5% between 400-1000 nm and less than 1% at all other wavelengths. All measurements were made in AC mode at 10 Hz chopping frequency under a bias light. The system was calibrated and operated in Beam Power mode.

Chapter 4 : Molecular Heterogeneous Ruthenium water oxidation catalysis

4.1 Introduction

Chapter 3 demonstrated the efficacy of utilizing a cooperative binding motif to enhance water stability of ruthenium compounds to titania surfaces while maintaining a high level of electronic communication. This enhancement led to the idea to investigate molecular ruthenium complexes for heterogeneous catalytic water oxidation. Our lab had been studying ruthenium catalytic water oxidation for half a decade (2008-2013),^{102,177-181} however appending them to surfaces was a new avenue. The principle was not novel in device architecture as T.J. Meyer in 2009 had reported appending a ruthenium polypyridyl complex to titania using a phosphonate group, however the archetypical design of these heterogeneous systems requires acidic conditions in order to maintain the catalyst on the surface and hinder catalyst desorption as well as oxidatively stable ligands.¹⁰³⁻¹⁰⁶ Previously utilizing cooperative binding had afforded ruthenium complexes that exhibit excellent stability in neutral pH, and thus I endeavoured to explore a heterogeneous molecular water oxidation catalyst that could operate under neutral pH or more ambitiously in salt water conditions. Heterogeneous systems are advantageous for their higher catalytic activity, smaller catalyst loading and separation efficiency, however they are more difficult to study mechanistically and catalyst desorption is a major concern. Another major shortcoming of using heterogeneous catalysts versus homogeneous ones, is that it is more difficult to investigate heterogeneous systems due to catalyst loading issues which relate to active sites become more difficult to reproduce/control and isolation of catalytic intermediates.¹⁸² Therefore, homogeneous water oxidation catalysis has been more extensively studied mechanistically using a myriad of ruthenium complexes that exhibit water oxidation catalysis.^{177,183,184} The following details my findings and remains unpublished to date. I studied

the potential of this motif first in homogenous and then in heterogeneous catalytic water oxidation.

4.2 Results and Discussion

There exists a considerable amount of research on ruthenium polypyridyl complexes in the context of catalytic water oxidation^{34,184,185}, however investigation of appending molecular catalysts to a surface has only more recently emerged as a promising way to improve the economic viability of these systems. Meyer and coworkers laid the foundation for molecular heterogeneous water oxidation using a $[\text{Ru}(\text{Mebimpy})(\text{bpy})-(\text{OH}_2)]^{2+}$ [Mebimpy = 2,6-bis(1-methylbenzimidazol-2-yl)-pyridine] with phosphonate anchoring groups under acidic conditions (Figure 4.1). They reported that electrocatalytic water oxidation was sustained on a surface-bound complex. In these types of mono-metallic surface bound systems at acidic pH the rate determining step involves O-O bond formation and the accessibility of Ru^{V} oxo ($\text{Ru}=\text{O}$) as being the critical mechanistic steps.^{186,187}

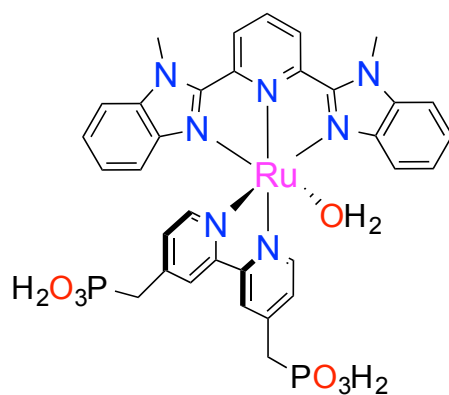


Figure 4.1. Surface-bound $[\text{Ru}(\text{Mebimpy})(4,4'-((\text{HO})_2\text{OPCH}_2)_2\text{bpy})(\text{OH}_2)]^{2+}$ [Mebimpy = 2,6-bis(1-methylbenzimidazol-2-yl)pyridine; bpy = 2,2'-bipyridine] by Meyer and coworkers.

Investigating the potential of the mesoionic carbene ligand scaffold to have the right electronics for water oxidation was paramount in determining the feasibility of this complex before endeavouring to append them to a surface (Figure 4.2). Catalyst **4.1** was proposed and synthesized using a similar synthetic protocol from that of previous mesoionic carbene chemistry (Scheme 4.1).^{81,97} The initial plan was to synthesize this compound which would be expanded into a larger series if the proof-of-concept was successful.

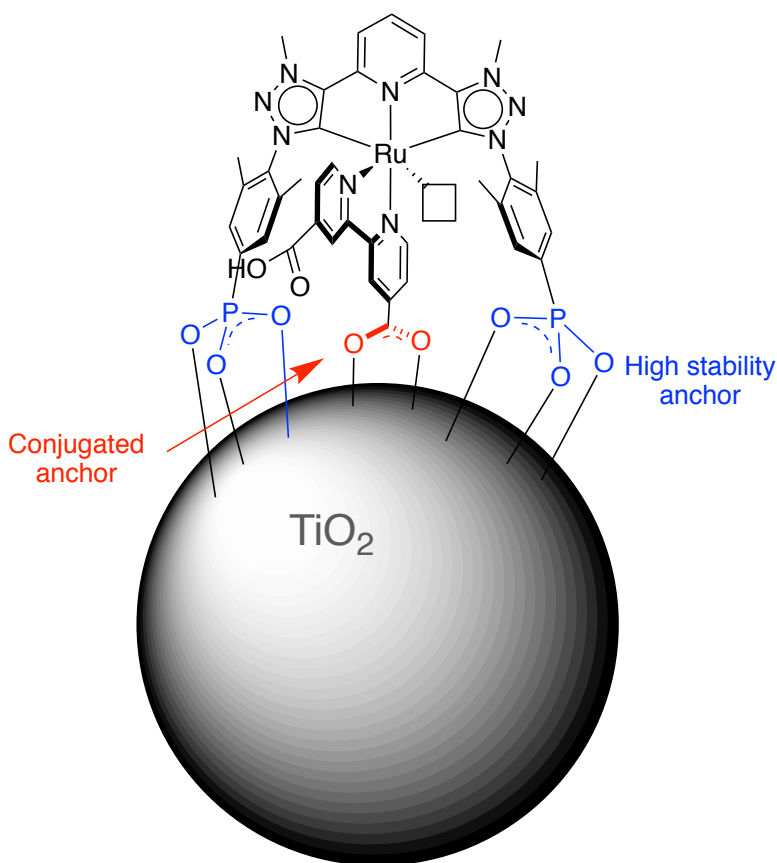
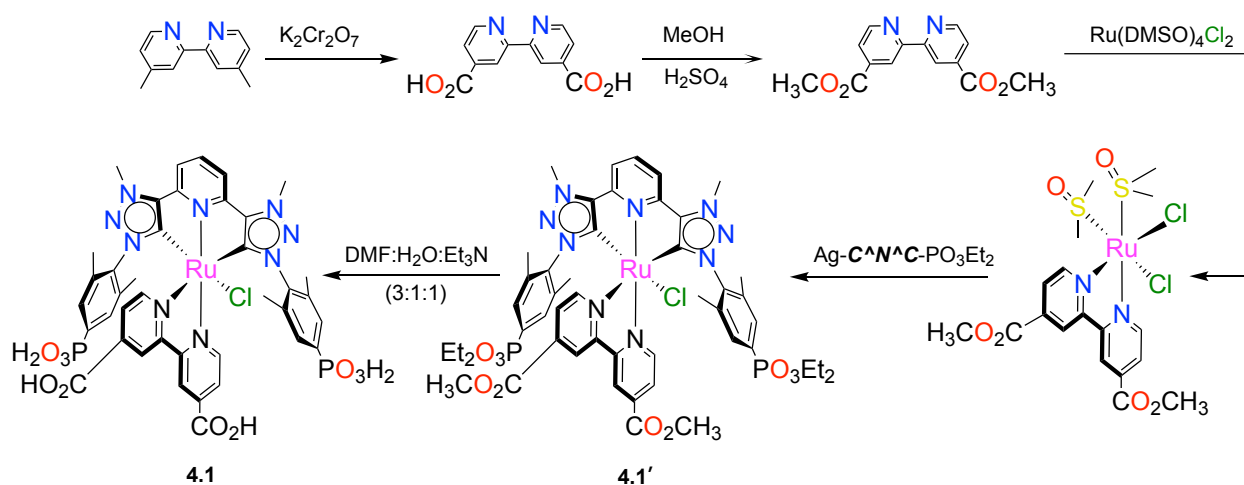


Figure 4.2. Molecular Ruthenium complex **4.1** for heterogeneous molecular water oxidation.

Mesoporous titania has been shown to be an excellent substrate for binding with acid-linked ruthenium compounds and due to its porous structure can afford a large working surface

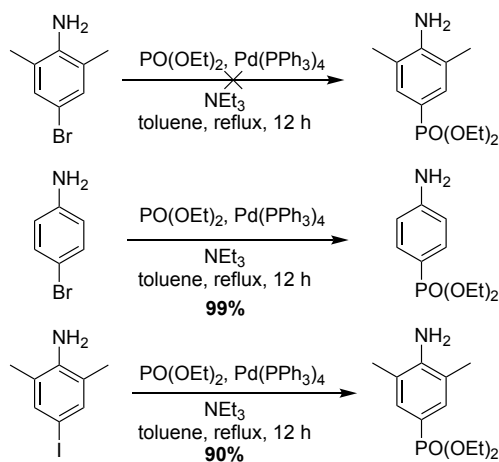
when replacing a dye coated titania substrate for the working electrode in a 3-electrode electrochemical cell.



Scheme 4.1. Synthetic approach to synthesizing the water oxidation catalyst **4.1**.

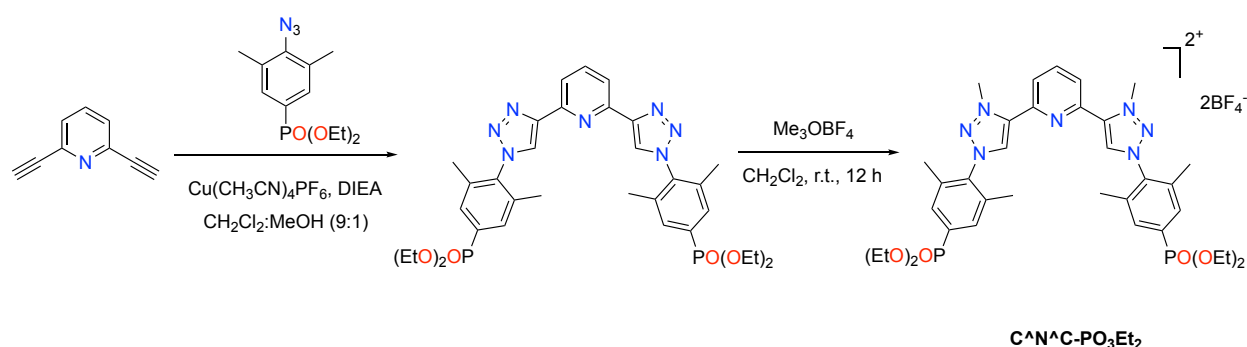
Complex **4.1** was synthesized by oxidation of 4,4'-dimethyl-2,2'-bipyridine with potassium dichromate in sulfuric acid, as previously reported by Morgan *et al* in a 92% yield.¹⁸⁸ The diacid was practically insoluble in all organic solvents and was esterified using standard procedures to the methyl ester.¹⁸⁹ Tetrakis(dimethylsulfoxide)dichlororuthenium(II) was synthesized from $\text{RuCl}_3 \cdot n\text{H}_2\text{O}$ after a brief reflux in DMSO and isolation of a yellow solid by addition of acetone. This ruthenium precursor was chosen over the classical $\text{RuCl}_3 \cdot n\text{H}_2\text{O}$ metalation conditions of polypyridines as it is a softer approach and does not require the reduction of the metal during metalation. Metalation of a stoichiometric equivalent of 4,4'-dimethoxycarbonyl-2,2'-bipyridine with $\text{Ru}(\text{DMSO})_4\text{Cl}_2$ yields both the *cis* and *trans* isomers, which can be easily separated by silica gel column chromatography, however both demonstrated reactivity in forming the target complex and so were combined and used as a mixture in the transmetalation step with the silver precursor ligand ($\text{Ag-C}^{\wedge}\text{N}^{\wedge}\text{C-PO}_3\text{Et}_2$). Studies conducted in

Chapter 2 and 3 utilized a library of substituted azides starting from the chemistry developed by Schulze *et al.* from 2,4,6-trimethylaniline that later underwent the copper-catalyzed cyclization or so called “click” reaction to yield 2',6'-bis(1-mesityl-1,2,3-triazol-4-yl)pyridine.⁸⁰ Synthesis of the 2,6-*bis*(1-(2,6-dimethyl-4-phosphonyl benzyl)-1*H*-1,2,3-triazol-4-yl)pyridine could only be accomplished under the synthesis outlined in Chapter 3. Scheme 4.2 shows that the attempts to synthesize diethyl (4-amino-3,5-dimethylphenyl)phosphonate from the widely accessible (4-bromo-2,6-dimethylaniline) directly via palladium-catalyzed cross coupling reactions were unsuccessful. Electronic effects play a critical role in the ability of substrates to cross couple, as the synthesis of diethyl (4-aminophenyl)phosphonate undergoes cross-coupling with diethyl phosphonate and 4-bromoaniline quite easily. The σ -donating ability of the two methyl groups must sufficiently deactivate/depolarize the bromine-carbon bond from Pd insertion, therefore it was necessary to use the more reactive precursor 4-iodo-2,6-dimethylaniline, synthesized from the iodation of 2,6-dimethylaniline using ICl (Scheme 4.2).¹⁷⁵



Scheme 4.2. Cross-coupling reactions with diethyl phosphonate and different aromatic halogens.

Furthermore, cross-coupling after the “click” reaction proved ineffective as it led to a mixture of mono- and bi-phosphonated products that were inseparable. Formation of the azido compounds was performed through nitrosation of the aromatic amine group into the diazonium salt in AcOH/H₂O mixture with NaNO₂ followed by rapid conversion to the azido with dropwise addition of NaN₃. The “click” reaction proved to be most effective with a Cu(CH₃CN)₄PF₆ catalyst as the copper source; general procedures for CuSO₄ and sodium ascorbate proved unsuccessful. In order to block potential coordination of the nitrogen in the triazole ring to the ruthenium precursor selective methylation using Meerwein’s salt ([Me₃O]BF₄) was effective.



Scheme 4.3. Copper catalyzed cyclization reaction and methylation with Meerwein’s salt.

Freshly prepared Ag₂O was required to prepare the silver(I) precursor (Ag-C^NC-PO₃Et₂).¹⁷⁶ MALDI-ToF MS measurements revealed a series of cyclic compounds of 1:1, 2:2 and 3:3 fragments (Ag:C^NC-PO₃Et₂) and was consistent with previous reports of this type of framework. Synthesis of the final compounds in Figure 4.3 was performed by transmetalation of the silver precursor with both Ru(DMSO)₄Cl₂ and Ru(bpy-COOCH₃)(DMSO)₂Cl₂. The former was attempted in an effort to avoid the use of a high-pressure bomb during synthetic protocol, which required dichloromethane at 70 °C for ~ 4 days. Ester **4.1'** was synthesized successfully

by first transmetalating $\text{Ru}(\text{DMSO})_4\text{Cl}_2$ under reflux, but the desired product was only a minor product in a mixture. The process was higher yielding by transmetalation of $\text{Ru}(\text{bpy-COOCH}_3)(\text{DMSO})_2\text{Cl}_2$. The acid **4.1** could be obtained by simple saponification protocol under reflux for 3 days in $\text{DMF}:\text{H}_2\text{O}:\text{Et}_3\text{N}$ (3:1:1 v/v).

$\text{Ru}(\text{bpy-COOCH}_3)(\text{terpy})\text{Cl}$ was synthesized using established chemistry and used as a benchmark for comparison in the electrochemical and spectroscopic characterization. Both compounds in Figure 4.3 were synthesized and characterized as the chloro species, which has been shown to undergo ligand exchange to the aqua complex in the presence of water.

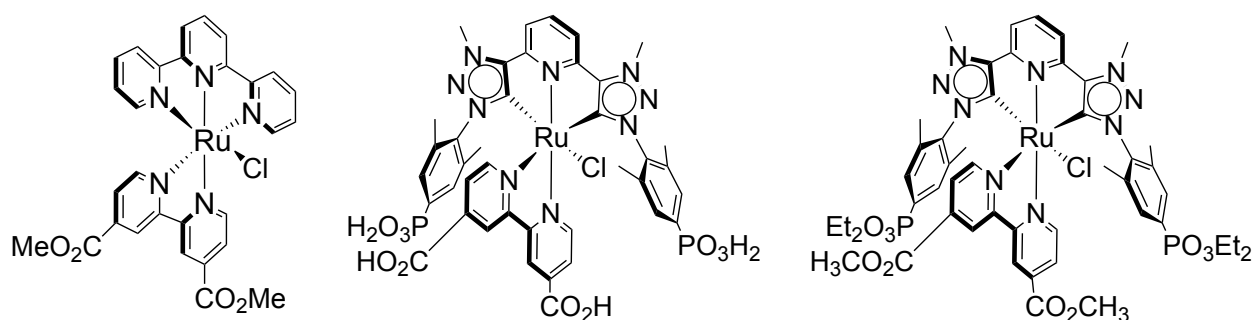


Figure 4.3. Water oxidation catalyst $\text{Ru}(\text{bpy-COOCH}_3)(\text{terpy})\text{Cl}$, **4.1** and **4.1'** synthesized for solution testing.

4.2.1 Electrochemical and UV-vis Spectroscopic Characterization

The UV-vis absorption data was tested in a variety of solvents (Figure 4.4). The UV-vis absorption data for the ester in aqueous solution showed two absorption maxima at 433 nm and 529 nm with extinction coefficients of $12300 \text{ M}^{-1}\text{cm}^{-1}$ and $8900 \text{ M}^{-1}\text{cm}^{-1}$, respectively. The absorption spectra are solvent-sensitive and shifts from DCM, MeCN and H_2O of the low energy MLCT transition of approximately 15 nm are the most notable change. This solvatochromic

behavior is attributed to the effect the different dielectric constants have on stabilization of the ground and excited states. Saponification of the ester complex yielded the acid compound **4.1** that exhibited a slight blue shift of the low energy MLCT band for the less π donating carboxylic and phosphonic acid moieties, which raises the LUMO energy at neutral pH (Figure 4.4b).

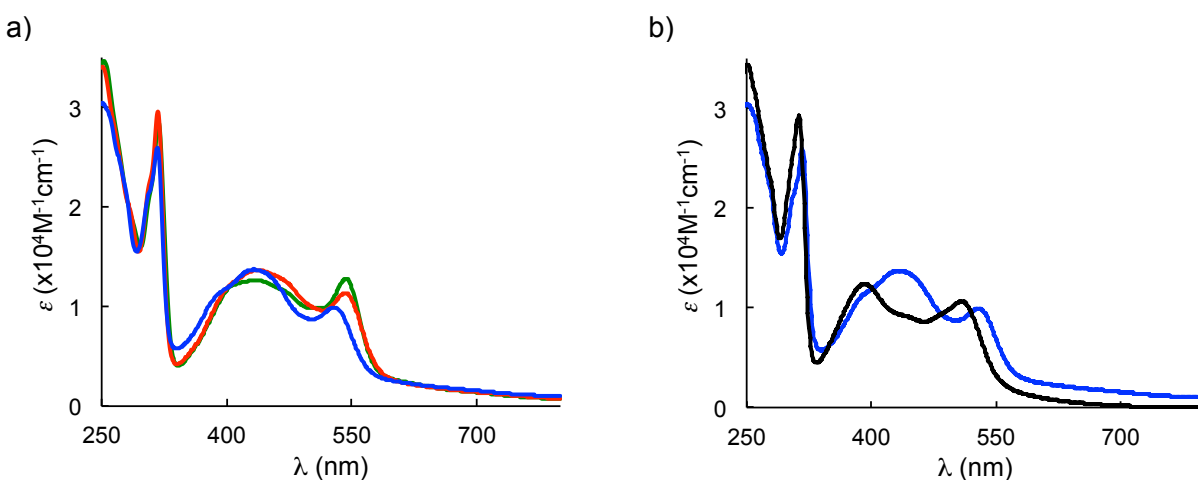


Figure 4.4. UV-vis absorption spectra for a) **4.1'** in H₂O (blue), MeCN (red) and DCM (green) and b) **4.1'** (blue) and **4.1** (black) in H₂O.

Temporal stability studies were conducted to determine the robustness of the system for molecular heterogeneous water oxidation. The two complexes studied were dip-coated onto titania substrates (details in Experimental Section) and submerged in different solutions in the dark and spectrophotometrically monitored by their lowest energy MLCT absorption intensity. Under acidic conditions (pH 4) **4.1/TiO₂** remained completely bound to the surface within error over a 2 h period, however in neutral pH it suffered catastrophic desorption within the first 10 min losing almost 70% of the surface coverage. Surprisingly, it only slightly outperformed the Ru(bpy-COOCH₃)(terpy)Cl that does not possess the phosphonate anchoring groups with a 90%

loss in 20 min. It may be that the vacant site contributed to a weakening of the binding properties of this motif.

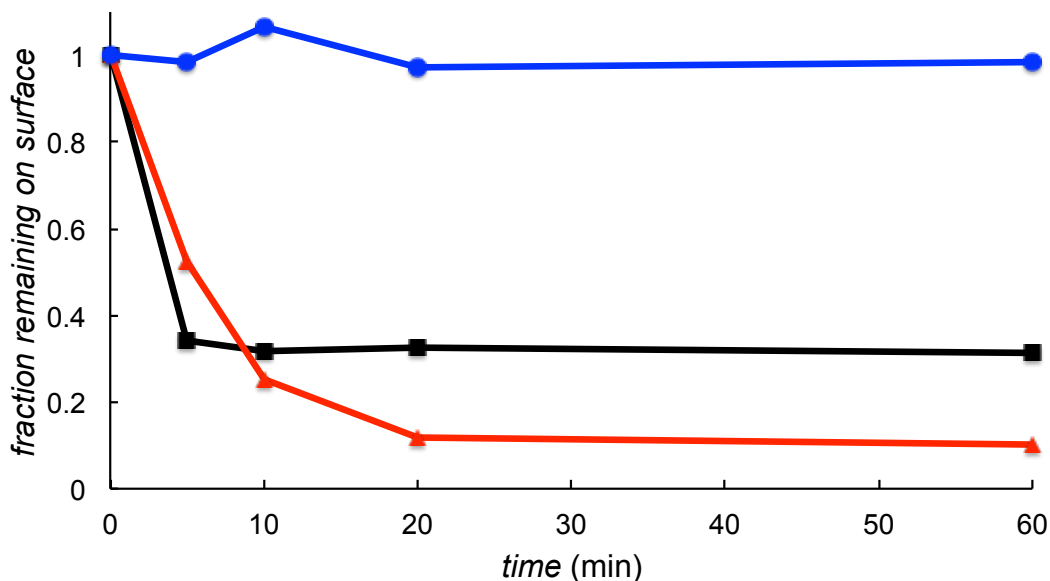


Figure 4.5. Temporal study of Ru(bpy-COOCH₃)(terpy)Cl (red), **4.1**/TiO₂ (black) bound to titania and submerged in neutral water over the period of 1 h. Temporal study of **4.1**/TiO₂ (blue) in pH 4 Britton-Robinson buffer.

Figure 4.6 shows that the binding modes of TiO₂ bound catalyst **4.1** (**4.1**/TiO₂) using diffuse reflectance infrared fourier transform (DRIFT) and reveals that not all anchoring –OH groups were attached. There was clear evidence of the presence of both C–OH stretching at 1150 cm⁻¹ and P–OH stretching at 860 cm⁻¹. Previous studies (see Chapter 3) showed little to no intensity in these regions for successfully anchored ruthenium complexes. The DRIFT analysis of **4.1**/TiO₂ showed little intensity in the P=O and C=O regions suggesting that binding occurred to some degree through each anchoring group, but it was not as tightly bound as **3.4** by evidence of the –OH stretching still present.

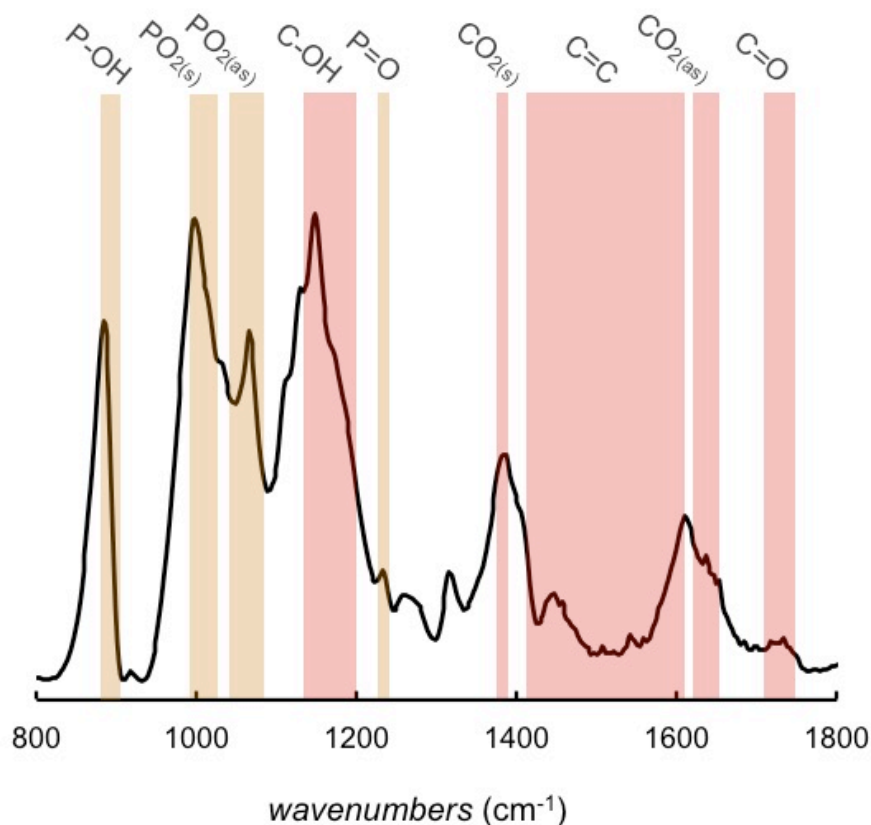


Figure 4.6. Kubelka-Munk DRIFTS spectra of **4.1**/TiO₂. Subscripts “s” and “as” represent symmetric and asymmetric, respectively.

Figure 4.7 shows partial binding of **4.1** to the titania surface with the exact geometry of the complex unknown. I speculate that if both carboxylic acid groups were bound then perhaps the phosphonate groups would only experience partially binding due to the distance they would be from the surface (Figure 4.7a). Another potential geometry consistent with the IR signals would involve a partial anchoring of the four anchoring groups (Figure 4.7b) and both geometries would be susceptible to hydrolysis in the presence of water due to the hydrogen bonding available with the –OH groups.

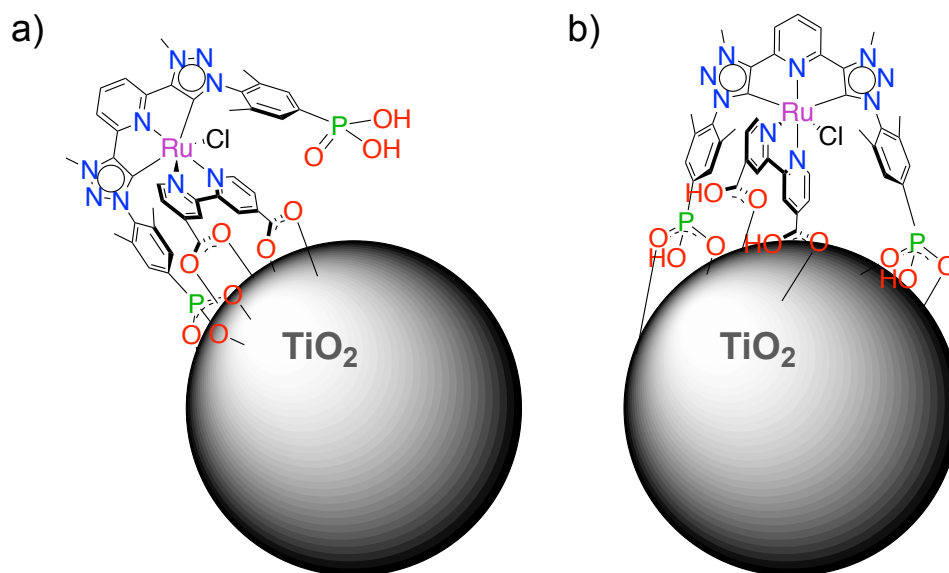


Figure 4.7 Proposed binding geometries for catalyst **4.1** to titania substrate when a) both carboxylate groups are bound and b) all groups are partially bound.

The electrochemical behaviour was probed by investigating the cyclic voltammetry (CV) of the complexes. Both the ester and the acid (**4.1'** and **4.1**) were studied under a variety of solvents as in some cases it was difficult to characterize **4.1** under standard electrochemical conditions due to solubility issues. In Figure 4.8, the CV of **4.1'** showed a reversible oxidation wave at 0.70 V (all potentials reported *vs* NHE) that was assigned as a Ru(III/II) redox couple in MeCN. This represented a ~50 mV anodic shift moving from compound **3.4'** with a terpy-COOCH₃ fragment to a Ru complex with bpy-COOCH₃ and chloro ligands. Interestingly, the next anodic redox process did not occur for over ~1V. The Ru (IV/III) couple has previously shown to be unobservable at low pH in some related complexes, which is attributed to kinetic PCET issues at the electrode surface.^{45,116-118} The second quasi-reversible oxidation wave at 1.76 V was therefore tentatively assigned to the Ru(V/IV) redox couple. For comparison, Meyer's compound (Figure 4.1) showed a Ru(III/II) couple at ~0.67 V and a Ru(V/IV) couple at ~1.67 V

in pH 5 acetate buffer. Meyer reported that the Ru(VI/III) was only observed at a pH of 14 with a slow scan rate 10mVs^{-1} . The CV evidence of the accessibility of the Ru^V oxidation state in **4.1'** was critical for water oxidation and I was ecstatic to see it at a reasonable potential. A ligand based irreversible reduction was evident at -0.84 V .

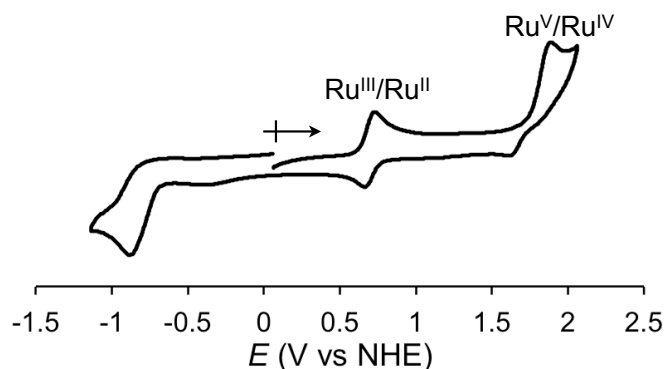


Figure 4.8. Cyclic voltammograms of **4.1'** measured in deaerated MeCN using a platinum working electrode with a TBABF₄ electrolyte (0.1 M) at 100 mVs^{-1} . Reference electrode Ag/Ag⁺. Referenced using ferrocene reported vs NHE (+0.62 V). Relevant redox couples are listed.

4.2.2 Catalytic water oxidation experiments

To explore the potential of this Ru(V/VI) couple water oxidation a series of CVs were conducted by spiking MeCN with varying amounts of H₂O and monitoring for the presence of water oxidation. A solution of **4.1'** in deaerated MeCN spiked with 100 μL of water (MeCN/100H₂O) revealed two new oxidative waves at 1.77 V and 2.07 V at a scan rate of 10 mVs^{-1} (Figure 4.9a). Analysis of the MeCN/100H₂O blank showed the presence of a peak at $\sim 2.03\text{ V}$, which suggests the oxidative wave is attributed to water oxidation by the platinum electrode at high potentials.¹⁰⁷ Increasing the concentration of the spiked water showed a

significant enhancement in the catalytic peak at ~ 1.75 V (Figure 4.9b). This increase in the catalytic peak is significantly more than the increase of the background current in the absence of **4.1'**. Furthermore, return of the cathodic scan shows that the intensity of the **4.1'** reduction peak at ~ 0.65 V remains unchanged after oxidation over all spiked concentrations, suggesting that it does not decompose (Figure 4.10b).

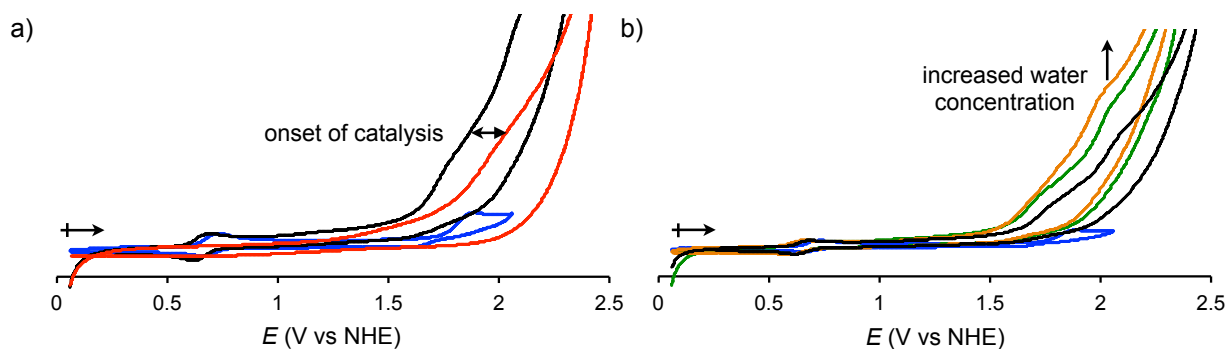


Figure 4.9. Cyclic voltammograms of **4.1'** with different amounts of spiked H_2O measured in deaerated MeCN using a platinum working electrode with a TBABF₄ electrolyte (0.1 M) at 10 mVs^{-1} . Reference electrode Ag/Ag⁺. Referenced using ferrocene reported vs NHE (+0.62 V). a) MeCN/100H₂O (red), **4.1'** in MeCN/100H₂O (black) and **4.1'** in MeCN (blue). b) **4.1'** in MeCN (blue), in MeCN/100H₂O (black), in MeCN/150H₂O. (green) and in MeCN/200H₂O (orange).

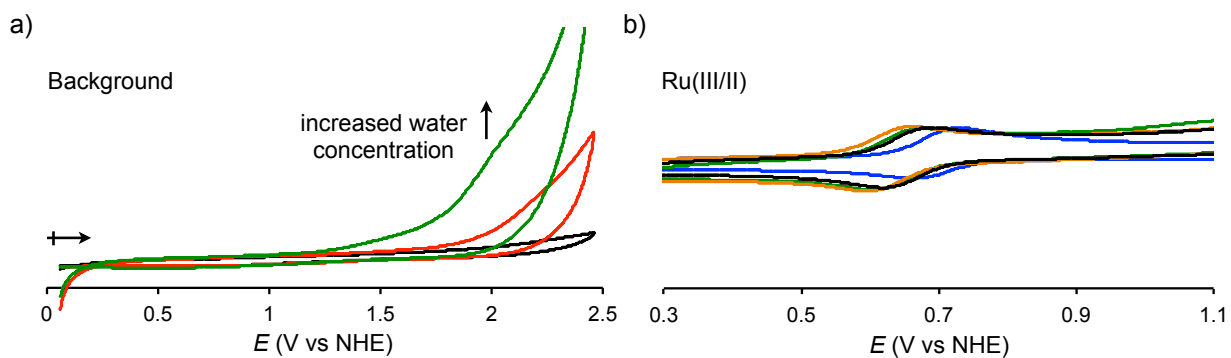


Figure 4.10 Cyclic voltammograms with different amounts of spiked H₂O measured in deaerated MeCN using a platinum working electrode with a TBABF₄ electrolyte (0.1 M) at 10 mVs⁻¹. Reference electrode Ag/Ag⁺. Referenced using ferrocene reported vs NHE (+0.62 V). a) Background MeCN (black), MeCN/50H₂O (red) and MeCN/100H₂O (green). d) Zoomed in version of graph Figure 4.9b (4.1') (see for details).

Figure 4.11 shows that in MeCN/200H₂O ester 4.1' has anodic (E_{pa}) and cathodic (E_{pc}) peak currents that vary with the square root of scan-rate ($R = 0.99$) which is consistent with a diffusion limited step.

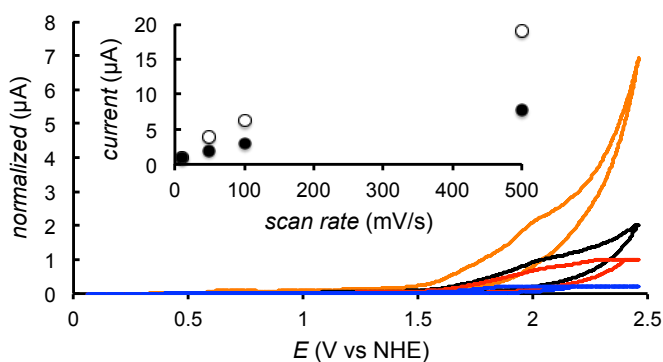


Figure 4.11. Cyclic voltammograms of 4.1' at scan rates 10 mVs⁻¹ (black), 50 mVs⁻¹ (green), 100 mVs⁻¹ (orange) and 500 mVs⁻¹ (blue) measured in deaerated MeCN/200H₂O using a platinum working electrode with a TBABF₄ electrolyte (0.1 M). 10 mVs⁻¹. Reference electrode Ag/Ag⁺.

Referenced using ferrocene reported *vs* NHE (+0.62 V). Inset shows E_{pc} (•) and E_{pa} (°) peak currents of Ru(III/II) couple plotted *vs* scan rate.

4.1 was tested at pH 4 ($\text{CH}_3\text{CO}_2\text{H}/\text{CH}_3\text{CO}_2\text{Na}$ buffer 0.1 M, 10 mVs^{-1}) and showed a reversible oxidation at 0.44 V (*vs* Ag/Ag^+) (Figure 4.12a) for the Ru (III/II) couple, which was similar to $\text{Ru}(\text{bpy}-\text{COOCH}_3)(\text{terpy})\text{Cl}$ at 0.44 V. When bound to titania **4.1/TiO₂** the Ru(III/II) couple shifted cathodically to 0.48 V (Figure 4.12b). Interestingly, when both **4.1** and $\text{Ru}(\text{bpy}-\text{COOCH}_3)(\text{terpy})\text{Cl}$ were bound to titania, and at slow scan rate, a second reversible oxidation was observed. The **4.1/TiO₂** reversible oxidation as $\sim 0.84 \text{ V}$ was attributed to the Ru(IV/III) couple. There was no observable decomposition in CV of **4.1/TiO₂** cycling over the two reversible oxidation events.

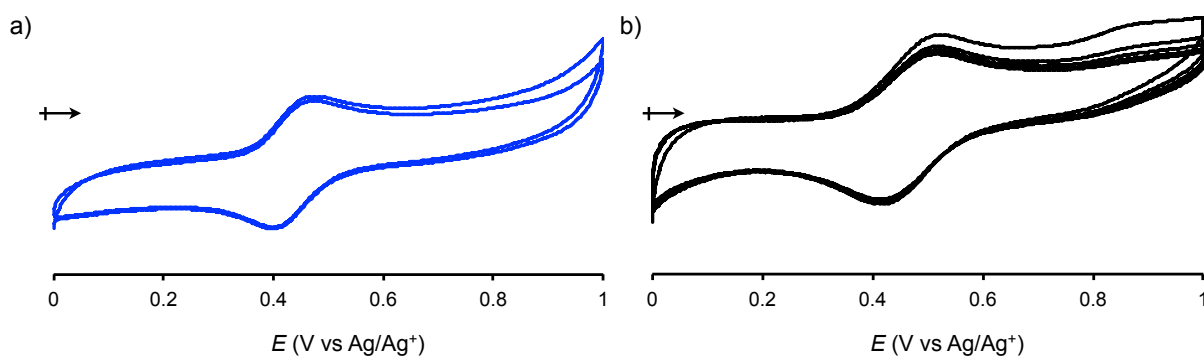


Figure 4.12. Cyclic voltammograms in acetate buffer (0.1 M) at pH 4 of a) **4.1** in solution with glass carbon working electrode and b) **4.1/TiO₂** bound to titania as working electrode. Scan rate 10 mVs^{-1} . Reference electrode Ag/Ag^+ .

The surface loading (in mol/cm²) was calculated for **4.1**/TiO₂ from UV-vis measurements using the expression described in the Chapter 1 ($\Gamma=A(\lambda)/[(10^3\varepsilon(\lambda))]$) with $\lambda_{\text{max}}=509$ nm, and $\varepsilon_{\text{max}}= 1.06 \times 10^4 \text{ M}^{-1}\text{cm}^{-1}$ from **4.1** in H₂O (Figure 4.13a).¹¹⁵ Saturation coverage was determined after 24 h of dip-coating to be $\Gamma = 2.75 \times 10^{-8} \text{ mol/cm}^2$ for **4.1**/TiO₂. Comparison with Ru(terpy)(bpy-CO₂H)Cl/TiO₂ with $\lambda_{\text{max}}=500$ nm, and $\varepsilon_{\text{max}}= 1.6 \times 10^4 \text{ M}^{-1}\text{cm}^{-1}$ in H₂O showed a coverage of $\Gamma = 1.68 \times 10^{-8} \text{ mol/cm}^2$ (Figure 4.13b). These surface coverage values were about half as much as the reported average for Meyer's compound ($\Gamma = 5.3 \times 10^{-8} \text{ mol/cm}^2$).¹⁰³

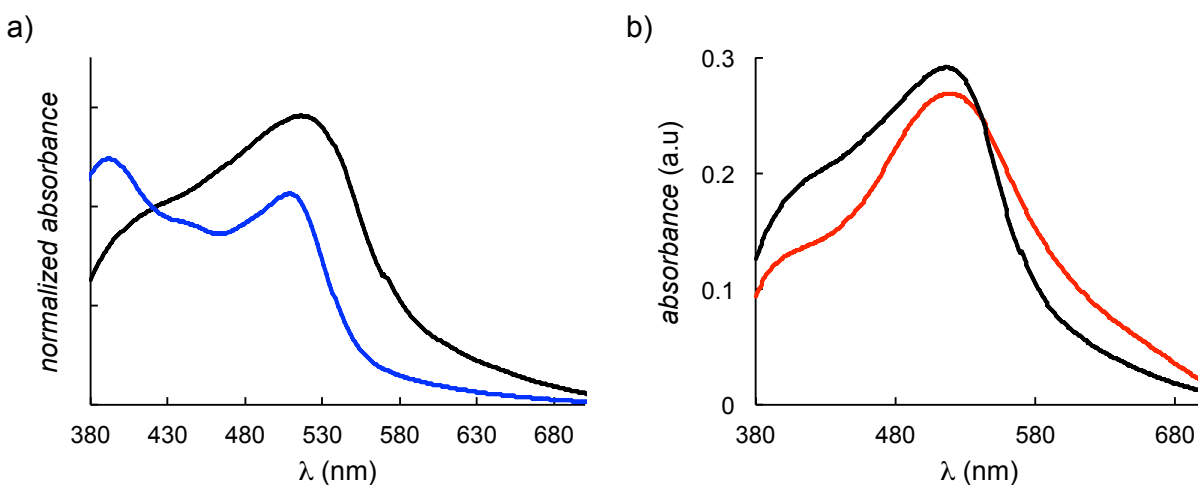


Figure 4.13. UV-vis spectra of a) **4.1** (blue) in H₂O and **4.1**/TiO₂ (black) and b) **4.1**/TiO₂ (black) and Ru(terpy)(bpy-CO₂H)Cl/TiO₂ (red)

CVs of surface bound **4.1**/TiO₂ showed a peak current for the Ru(III/II) couple that varied linearly with the square root of the scan rate (Figure 4.14). This is consistent with other surface anchored compounds that are diffusion-limited by electron transfer to and from the surface couple.¹¹⁵

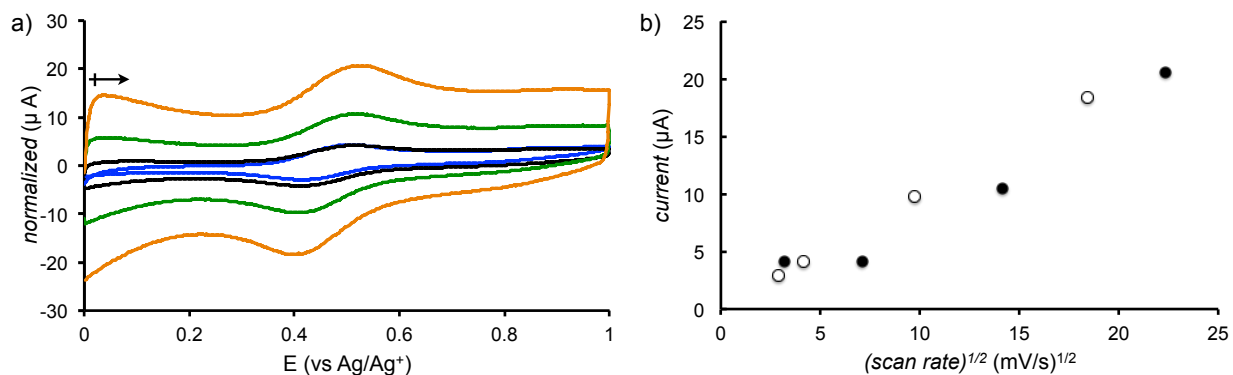


Figure 4.14. Cyclic voltammograms of **4.1/TiO₂** a) at scan rates 10 mVs⁻¹ (blue), 50 mVs⁻¹ (black), 200 mVs⁻¹ (green) and 500 mVs⁻¹ (orange) and b) shows E_{pc} (●) and E_{pa} (○) peak currents of Ru(III/II) couple plotted vs square root of scan rate. Measured in acetate buffer (0.1 M) at pH 4. Reference electrode Ag/Ag⁺.

Catalyst **4.1/TiO₂** was also tested against the bare TiO₂ substrate and the onset of catalysis occurred at a lower potential of ~1.28 V compared to ~1.6 V for bare TiO₂ (Figure 4.15a) in pH 4 acetate buffer. The surface bound water oxidation catalyst **4.1/TiO₂** had a higher onset of catalysis than the solution based catalyst **4.1** (~1.2 V) as the titania substrate affected the catalytic performance based on the overpotential required for water oxidation by ~100 mV (Figure 4.15b). Multiple scans over the potential window for **4.1/TiO₂** showed no change in the CV and therefore no observable decomposition lending evidence towards a stable system for heterogeneous water oxidation (Figure 4.15c). A determination of the available sites that were electroactive at scan rates of 100 mVs⁻¹ and 10 mVs⁻¹ based on peak current measurements were 1.0% and 2.5% respectively (Figure 4.15d). Ru(bpy-CO₂H)(terpy)Cl showed a 1.0% electroactivity at 100 mVs⁻¹. Meyer reported an activity of 8.0% at 10 mVs⁻¹. The poor

electroactivity of catalyst **4.1/TiO₂** was perhaps related to poor anchoring of the catalysts.

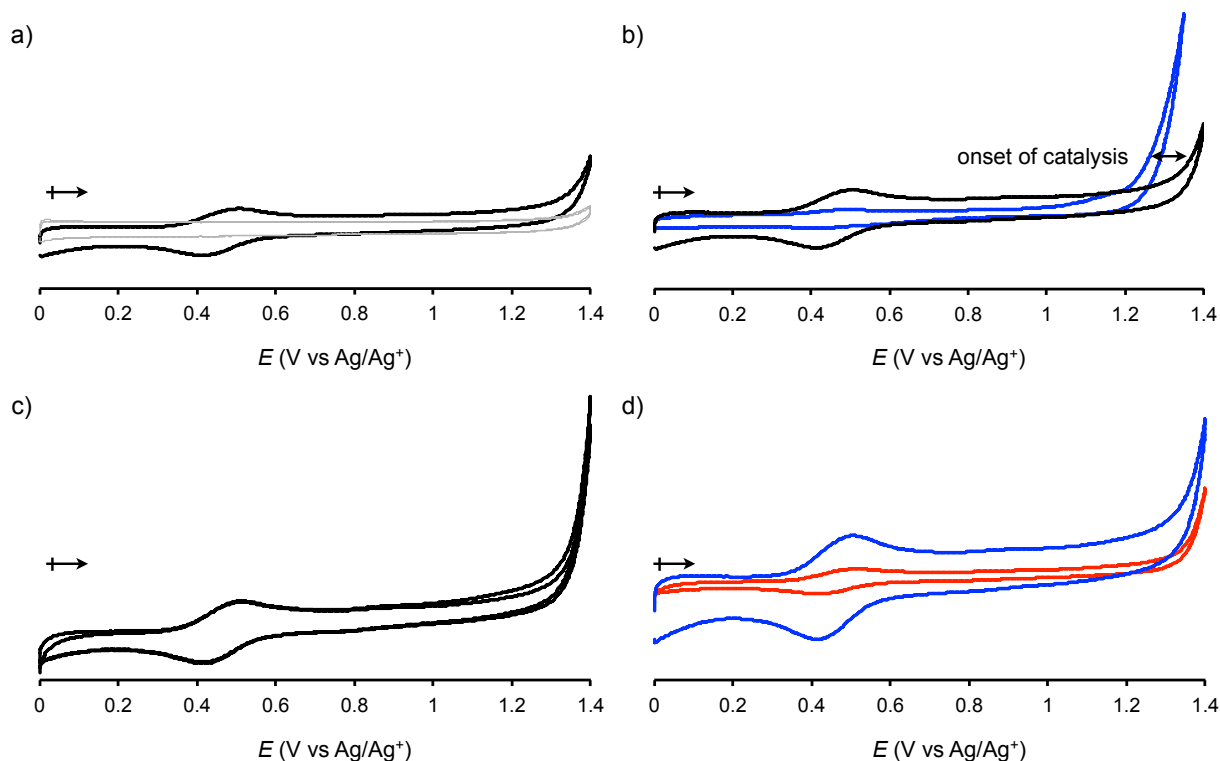


Figure 4.15. Cyclic voltammograms of a) **4.1/TiO₂** (black) and bare TiO₂ (gray); b) **4.1/TiO₂** (black) and **4.1** (blue); c) Multiscans of **4.1/TiO₂**; d) **4.1/TiO₂** at 10 mVs⁻¹ (red) and 100 mVs⁻¹ (blue). Measured in acetate buffer (0.1 M) at pH 4. Scan rate at 10 mVs⁻¹ unless otherwise stated.

Maintaining an applied potential at 1.3 V at pH 4 resulted in sustained electrocatalytic water oxidation (Figure 4.16b) of **4.1/TiO₂** with a current density of $\sim 4.0 \mu\text{A}/\text{cm}^2$. Catalysis was sustained for 600 s corresponding to a turnover frequency (TOF) of 0.0004 s^{-1} . Water oxidation was very slow because of the rate-limiting cross-surface electron transfer through the TiO₂ as previously reported.¹¹⁵ Catalyst **4.1/TiO₂** did generate a higher current density than the

comparative $\text{Ru}(\text{bpy-CO}_2\text{H})(\text{terpy})\text{Cl}/\text{TiO}_2$ compound ($\sim 1.67 \mu\text{A}/\text{cm}^2$) however both underperformed in comparison to Meyer's phosphonate compound with $\text{TOF} = 0.004 \text{ s}^{-1}$.

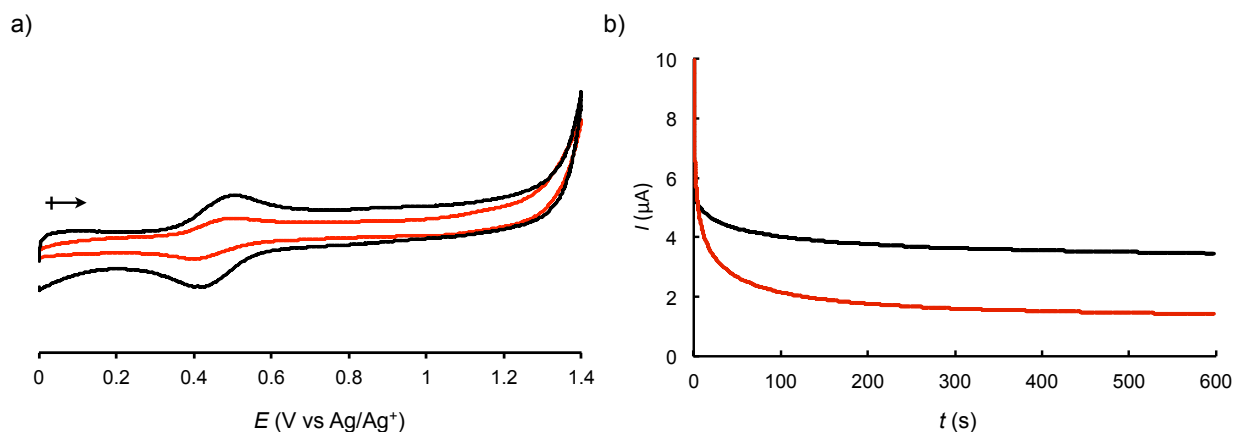


Figure 4.16. Cyclic voltammograms of **4.1**/ TiO_2 (black) and $\text{Ru}(\text{bpy-CO}_2\text{H})(\text{terpy})\text{Cl}/\text{TiO}_2$ (red) taken at a) 10 mVs^{-1} in acetate at pH 4.0; reported vs. Ag/Ag^+ and b) Sustained catalysis at 1.3 V.

4.3 Summary

Compounds **4.1'**, **4.1** and **4.1**/ TiO_2 were characterized and showed similarities in electrochemical and spectroscopic properties to dyes investigated in previous Chapters. The critical Ru^{V} oxidation state was determined to be accessible in MeCN for **4.1'** and upon addition of water demonstrated catalytic water oxidation. The compounds showed remarkable electrochemical stability (no evidence of decomposition) upon multiple oxidative and reductive sweeps around multiple oxidation states (III/II and V/VI). The Ru (IV/III) redox couple was unobservable in **4.1'** and **4.1** likely due to kinetic PCET process at the electrode as previously reported.¹¹⁶ The Ru(IV/III) couple was evident when bound to titania **4.1**/ TiO_2 at a slow scan rate. Surface coverage of **4.1**/ TiO_2 appeared to be approximately half of what has been previously reported.¹⁰³ The temporal stability studies showed that the acid complex **4.1** was only

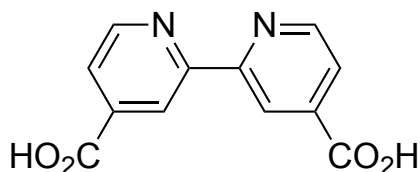
stable in acidic media pH 4 and hydrolyzed rapidly in neutral water. Electrocatalytic water oxidation was achieved for all compounds tested. Based on variable-scan-rate CV experiments, the process was determined to be diffusion limited in both **4.1/TiO₂** and **4.1'**.¹⁰⁴

4.4 Conclusions

Meyer had inspired an investigation of the cooperative binding motif in the context of heterogeneous molecular water oxidation. The motif had previously showed it afforded a unique combination of maintaining good electronic communication through the carboxylate linkers while garnering extra stability through utilizing phosphonate linkers. Synthesizing the compounds from established protocols yielded prototype compounds **4.1'**, **4.1** and **4.1/TiO₂**. **4.1** was intended to be a top performer for the future construction of a series with modifications based on anchoring groups to be tested. Unfortunately, **4.1/TiO₂** was rather unimpressive at oxidizing water and even less impressive at staying bound to the titania surface. This strategy does not seem to be viable for water oxidation and the project was not taken any further.

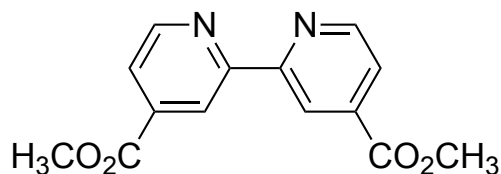
4.5 Experimental Details

4.5.1 Synthesis



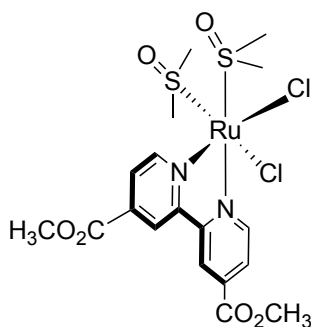
2,2'-Bipyridine-4,4'-dicarboxylic acid. 4,4'-Dimethyl-2,2'-bipyridine (5.00 g, 27.1 mmol) was added to a stirring solution of concentrated sulfuric acid (125 mL) at *r.t.*. Potassium dichromate

(24.0 g, 81.6 mmol) was then added to the clear solution in small portions, which caused the solution to become opaque and deep green and the temperature was maintained at 75+/-5°C. Occasional cooling in a ice bath was necessary during the addition of potassium dichromate. After the addition of all dichromate, the reaction was stirred until the reaction temperature cooled to *r.t.*. The reaction mixture was poured into 800 mL of ice water and filtered. The solid was washed with water until the filtrate was colourless and allowed to dry. The resulting yellow solid was then further purified by refluxing in 50% nitric acid (170 mL) for 4 h. The solution was then poured over ice, diluted with water (1 L) and cooled on ice. The precipitate was filtered, washed with water, then MeOH and dried to yield a fine white solid (5.59 g, 84%). ¹H NMR (400 MHz, D₂O, ppm) δ 8.76 (d, *J* = 5.0 Hz, 2H), 8.49 – 8.28 (m, 2H), 7.85 (dd, *J* = 4.9, 1.6 Hz, 2H) HRMS (ESI, *m/z*): 244.0485, C₁₂H₈N₂O₄ requires 244.0484. ¹H NMR data is in agreement with that previously reported.¹⁸⁸



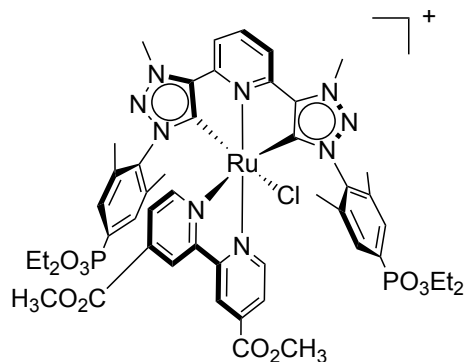
4,4'-Dimethoxycarbonyl-2,2'-bipyridine. 2,2'-Bipyridine-4,4'-dicarboxylic acid (5.56 g, 22.8 mmol) in methanol (100 mL) was added concentrated sulfuric acid (12 mL) and refluxed for 60 h. The solution was then poured into water (250 mL) forming a white slurry. The pH of the slurry was brought to 8 with 25% (w/w) aqueous sodium hydroxide. The product was then extracted with chloroform, dried over NaSO₄, filtered and evaporated at *r.t* to yield the white product (5.56 g, 91%). It was used without further purification. ¹H NMR (400 MHz, CDCl₃,

ppm) δ 8.92 (d, $J = 1.5$ Hz, 2H), 8.81 (d, $J = 5.0$ Hz, 2H), 7.91 (dd, $J = 5.0$, $J = 1.5$ Hz 2H), 4.05 (s, 6H). $^{13}\text{C}\{^1\text{H}\}$ NMR (101 MHz, CDCl_3 , ppm) δ 167.1, 154.5, 139.2, 123.1, 120.6, 55.4. ^1H NMR data is in agreement with that previously reported.¹⁸⁸

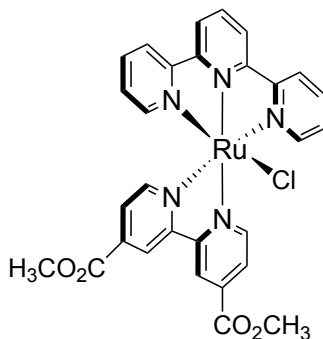


Dichlorobis(dimethyl sulfoxide) [4,4'-(Dimethoxycarbonyl)-2,2'-bipyridine]ruthenium(II).

$\text{Ru}(\text{DMSO})_4\text{Cl}_2$ (515 mg, 1.06 mmol) was dissolved in CHCl_3 (12 mL) and the yellow mixture brought to reflux. A solution of 4,4'-(dimethoxycarbonyl)-2,2'-bipyridine (287 mg, 1.05 mmol) dissolved in CHCl_3 (10 mL) was added drop-wise to the reaction, which turned the mixture red, and refluxed for 15 h. The solvent was removed and the residue was purified by column chromatography on silica ($\text{CH}_2\text{Cl}_2/\text{MeOH}$; 98:2) to obtain a brown solid that was a mixture of the *cis*- and *trans*- isomers (420 mg, 66%). *cis* isomer. ^1H NMR (400 MHz, CDCl_3 , ppm) δ 10.06 (d, $J = 5.7$ Hz, 1H), 9.86 (d, $J = 5.7$ Hz, 1H), 8.80 (s, 1H), 8.73 (s, 1H), 8.12 (dd, $J = 5.7$ and 1.5 Hz, 1H), 7.99 (dd, $J = 5.7$ and 1.5 Hz, 1H), 4.54 (s, 6H), 3.53 (s, 6H), 3.23 (s, 3H), 2.74 (s, 3H). *trans* isomer. ^1H NMR (400 MHz, CDCl_3 , ppm) δ 9.92 (d, $J = 5.7$ Hz, 2H), 8.66 (s, 2H), 8.05 (dd, $J = 5.7$ and 1.5 Hz, 2H), 4.54 (s, 6H), 3.06 (s, 12H). HRMS (ESI-ToF, m/z): 600.9573 ($[\text{M}+\text{H}]^+$), $\text{C}_{18}\text{H}_{24}\text{Cl}_2\text{N}_2\text{O}_6\text{RuS}_2^+$ requires 600.9575. ^1H NMR data is in agreement with that previously reported.⁸⁰



Ru(bpy-(CO(OCH₃)))(C[^]N[^]C-PO₃Et₂)Cl. To a dry flask containing Ru(bpy-(CO(OCH₃)))(DMSO)₂Cl₂ (114 mg, 0.190 mmol) and Ag-(C[^]N[^]C-PO₃Et₂) (149 mg, 0.180 mmol) was added dry nitrogen-purged dichloromethane (12 mL). The reaction was heated in a Schlenk flask at 70°C for 24 h. The reaction was then brought to dryness by a rotary evaporator. The crude reaction mixture was then purified by silica gel column chromatography (MeCN:H₂O, 4:0.4)). The impurities eluted out first, while the product band did not move. Upon addition of NaCl to the eluent the product band eluted out. The dark red product was isolated (179 mg, 82%). ¹H NMR (400 MHz, CD₃OD, ppm) δ 9.62 (d, *J* = 6.1 Hz, 1H), 8.52 (d, *J* = 1.4 Hz, 1H), 8.24 (d, *J* = 1.4 Hz, 1H), 8.20 (d, *J* = 3.1 Hz, 1H), 8.18 (s, 1H), 8.15 (d, *J* = 5.8 Hz, 1H), 8.03 (d, *J* = 6.0 Hz, 1H), 7.55 (dd, *J* = 6.0, 1.8 Hz, 1H), 7.47 (dd, *J* = 6.1, 1.8 Hz, 1H), 7.21 (d, *J* = 13.4 Hz, 2H), 7.04 (d, *J* = 13.6 Hz, 2H), 4.72 (s, 6H), 4.27 – 4.02 (m, 11H), 4.01 (s, 3H), 1.40 (dt, *J* = 14.4, 7.1 Hz, 12H), 0.89 (s, 12H). HRMS (ESI-ToF, *m/z*): 1130.2442 C₄₉H₅₇ClN₉O₁₀Ru⁺ requires 1130.2436 Anal Calcd for C₄₉H₅₇BF₄ClN₉O₁₀Ru•H₂O: C,47.64; H, 4.81; N, 10.20; Found: C,47.76; H, 4.56; N,10.74



Chloro(4,4'-(Dimethoxycarbonyl)-2,2'-bipyridine)(2,2':6',2''-terpyridine) ruthenium(II)

Chloride. To a flask containing Ru(terpy)Cl₃ (100 mg, 227 μmol) and 4,4'-(Dimethoxycarbonyl)-2,2'-bipyridine (60 mg, 220 μmol) dissolved in MeOH (7 mL) was added dropwise 4-ethylmorpholine (0.5 mL) and the reaction mixture brought to reflux for 24 h. The product was isolated. ¹H NMR (400 MHz, DMSO, ppm) δ 10.27 (d, *j* = 6.0 Hz, 1H), 9.26 (s, 1H), 9.0 (s, 1H), 8.88 (d, *J* = 8.0 Hz, 2H), 8.70 (d, *J* = 8.0, 2 H), 8.43 (dd, *J* = 5.6 Hz), 8.29 (t, *J* = 8.4 Hz, 1H), 8.08 (t, *J* = 7.6 Hz, 2H), 7.65 (m, 3H), 7.45 (m, 2H), 7.35 (t, *J* = 6.8 Hz, 2H), 4.03 (s, 3H). ¹H NMR data is in agreement with that previously reported.¹⁷⁷ HRMS (ESI-ToF, *m/z*): 642.0478 C₂₈H₂₅Cl₂N₅O₄Ru⁺ requires 642.0482

General procedure for saponification

The ester complexes were each refluxed in a mixture of DMF:H₂O:Et₃N (3:1:1 v/v) for 3 days, with evaporation of solvent quantitatively affording the saponified product. Saponification was confirmed by monitoring the disappearance of ¹H-NMR spectroscopic resonances attributable to the ester alkyl chains.

4.5.2 *Physical Methods*

Electrochemistry. Electrochemical measurements were performed under anaerobic conditions with a Princeton Applied Research VersaStat 3 potentiostat using dry solvents, Pt or glassy carbon working electrode and a Pt counter electrodes, a Ag pseudoreference electrode, and 0.1 M NBu₄BF₄ or acetate supporting electrolyte.

Dye Desorption Studies. Titania covered substrates of **4.1/TiO₂** and Ru(terpy)(bpy-CO₂H)(Cl)/TiO₂ were prepared by dip coating in ethanolic solution for 24 h in the dark. The dye soaked films were desorbed with pH 7 deionized water and in pH 4 buffer in the dark. The UV-vis absorption intensity of the ¹MLCT band centered at approximately 500 nm was monitored as a function of time over 1 h. Electronic spectroscopic data were collected in MeCN, DCM and H₂O solutions using a Cary 5000 UV-vis spectrophotometer.

DRIFTS Studies. Titania substrates were prepared on a 0.88 cm² active area (12 μm), in the fashion as described above. Prior to acquisition of spectra the samples were heated at 120 °C for 24 h. The instrument was controlled and analyzed by the program “Resolutions pro”. FT-IR data was collected on a Varian 7000 FT-IR instrument with a diffuse reflectance accessory, and all data is reported as Kubelka Munk and manipulated within the program.

Chapter 5 : Conclusions and future Directions

5.1. Conclusions

This thesis provides an investigation into mesoionic carbene *bis*tridentate ruthenium complexes with a systematic study of the photophysical properties and their application in the DSSC and heterogeneous molecular water oxidation catalyst. The unique nature of the geometry and electronics of this ligand had previously not been reported in these applications.

Chapter 2 described the study of *bis*tridentate ruthenium complexes, which when bearing terpy ligands, have historically shown poor excited state lifetimes due to the thermally accessible deactivating 3MC state.^{44,47} This state lies much closer in energy to the emissive 3MLCT state for $Ru(terpy)_2$ than for $Ru(bpy)_3$ analogs, as a result of the weak ligand field strength of a tridentate ligand affording a strained octahedral environment.⁷⁴ Efforts to improve the lifetimes of *bis*tridentate ruthenium complexes containing terpy fragments is desirable because it allows the extensive synthetic protocols of terpy frameworks in supramolecular assemblies with a ligand environment that promotes vectorial electron transfer in said assemblies.^{95,121} Furthermore, the *bis*tridentate system circumvents the isomerization complications of a *tris*bidentate system. In moving from $Ru(terpy)_2$ with an excited-state lifetime at room temperature on the picosecond timescale to a scaffold that replaces a single terpy ligand for the a 2,6-bis(1-(2,4,6-trimethylbenzyl)-1H-1,2,3-triazol-4-yl)pyridine (C^N^C), the lifetime improves to the nanosecond time regime.⁸¹ Furthermore, the excited-state electron density resides on the terpy fragment, which is important if this is the intended site for electron transfer events. By installation of an EDG on the terpy fragment and an EWG on the C^N^C fragment the excited state electron density switches to the C^N^C and improves the lifetime by another order of magnitude. These room

temperature lifetimes are among the highest ever recorded for a ³MLCT state of a ruthenium *bis*tridentate system with a terpy fragment (2.0-7.9 μs).

The C[^]N[^]C framework was further expanded to include a series of anchoring groups to explore the unique geometry of the mesityl moieties and their use in binding to TiO₂ was described in Chapter 3. This framework allowed tethering of both ligands to TiO₂ as a means to improve stability and a synthetic handle to employ a combination of anchoring groups chosen for enhanced stability and electronic communication within a DSSC.¹⁹⁰ The anchoring groups investigated were the -CO₂H and -PO₃H₂. The carboxylate anchoring group is ubiquitous in the DSSC realm and has higher electron-injection efficiencies than phosphonate anchors; however, it suffers from stability issues in the presence of H₂O and consequently requires rigorously anhydrous device manufacturing.¹⁹¹⁻¹⁹² Conversely, the phosphonate anchoring group has demonstrated greater stability in aqueous conditions. These characteristics led to the compound in Figure 5.1 that was designed with a combination of both anchoring groups. The -PO₃H₂ were appended to the remote C[^]N[^]C ligand farthest from the TiO₂ and the carboxylate -CO₂H to the terpy fragment responsible for electron injection. Computational results showed the LUMO resided on the terpy fragment, which is an important design element for effective electron injection in the DSSC. This cooperative anchoring approach produced a test cell DSSC that was impervious to dye hydrolysis and demonstrated that the combination of anchoring groups was required for maximum *PCE* (0.2%).⁹⁷

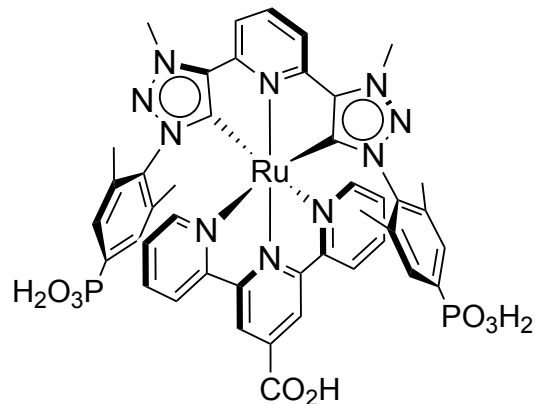


Figure 5.1 Top performing dye from Chapter 3 that illustrated cooperative binding approach using carboxylate and phosphonate anchoring groups.

This enhanced stability of cooperative binding was explored in the context of water oxidation in Chapter 4. Ruthenium polypyridyl complexes are well known to catalytically split H_2O and procedures for heterogenization are important in industrial processing.^{193,194} These procedures use anchoring groups in the same way dyes anchor to TiO_2 in the DSSC. Surface bound complexes bearing carboxylates are usually unstable and hydrolyze in the presence of H_2O and phosphonates are unstable under basic conditions.¹⁹⁵ The $\text{C}^{\wedge}\text{N}^{\wedge}\text{C}-\text{PO}_3\text{H}_2$ ligand scaffold had never been reported in the application of catalytic water oxidation and the catalyst in Figure 5.2 was shown to be capable of catalytically splitting water in solution. Once bound to the TiO_2 the complex showed a significantly lower catalytic activity than in free solution, but remained bound to the surface during catalysis at pH 4. Temporal stability studies revealed a complex that was not stable under neutral pH, which was attributed to incomplete binding of the anchoring groups to the TiO_2 surface.

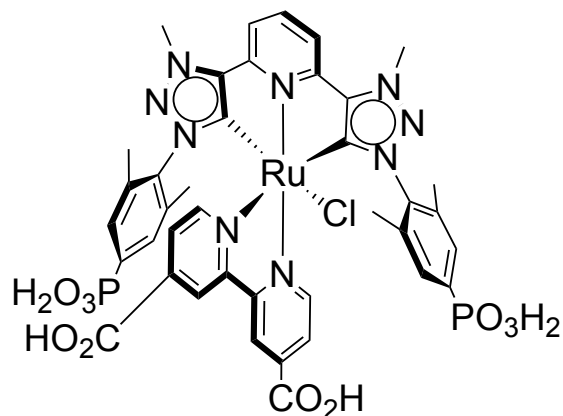


Figure 5.2 Water oxidation catalyst from Chapter 4.

5.2. Future Directions

The photophysics of the C^NC platform offers a new avenue for bistridentate ruthenium complexes possessing long-lived ³MLCT states with excellent redox stability. During the early work into investigating these compounds in Chapter 3, it was noticed that an orange coloured dip-coated TiO₂ substrate became clear upon reduction of the substrate. During continuous oxidation and reduction of the substrates the colour could be regained or removed. This property could make these complexes useful in testing their application in electrochromic devices. Lowering the LUMO π* ligand orbital shifts the absorption spectrum from the visible into the IR. TiO₂ absorbs in the UV, such that a device would appear clear or frosted-white due to the mesoporous TiO₂. This electrochromic effect has been shown in organic polymer films.¹⁹⁶ The true novelty of electrochromics would be if you could design this effect to operate within the DSSC framework. A device that operates as a window in two modes: 1) reduction of the dye and the window becomes transparent and operates as a classical window and 2) regeneration of the dye and the window operates as a DSSC (Figure 5.3). A so-called “smart material” that switches between the modes with the application of a potential bias. The chosen electrolyte

would need to be tailored to become completely oxidized in mode 1 and then be able to re-establish DSSC operation in mode 2 by a potential bias. In theory, a less mechanistically complicated cobalt based electrolyte ($\text{Co}(\text{bpy})_3^{2+/3+}$)^{197,198} could be capable ($E_{1/2} \sim 0.6 \text{ V}$ (vs NHE)).

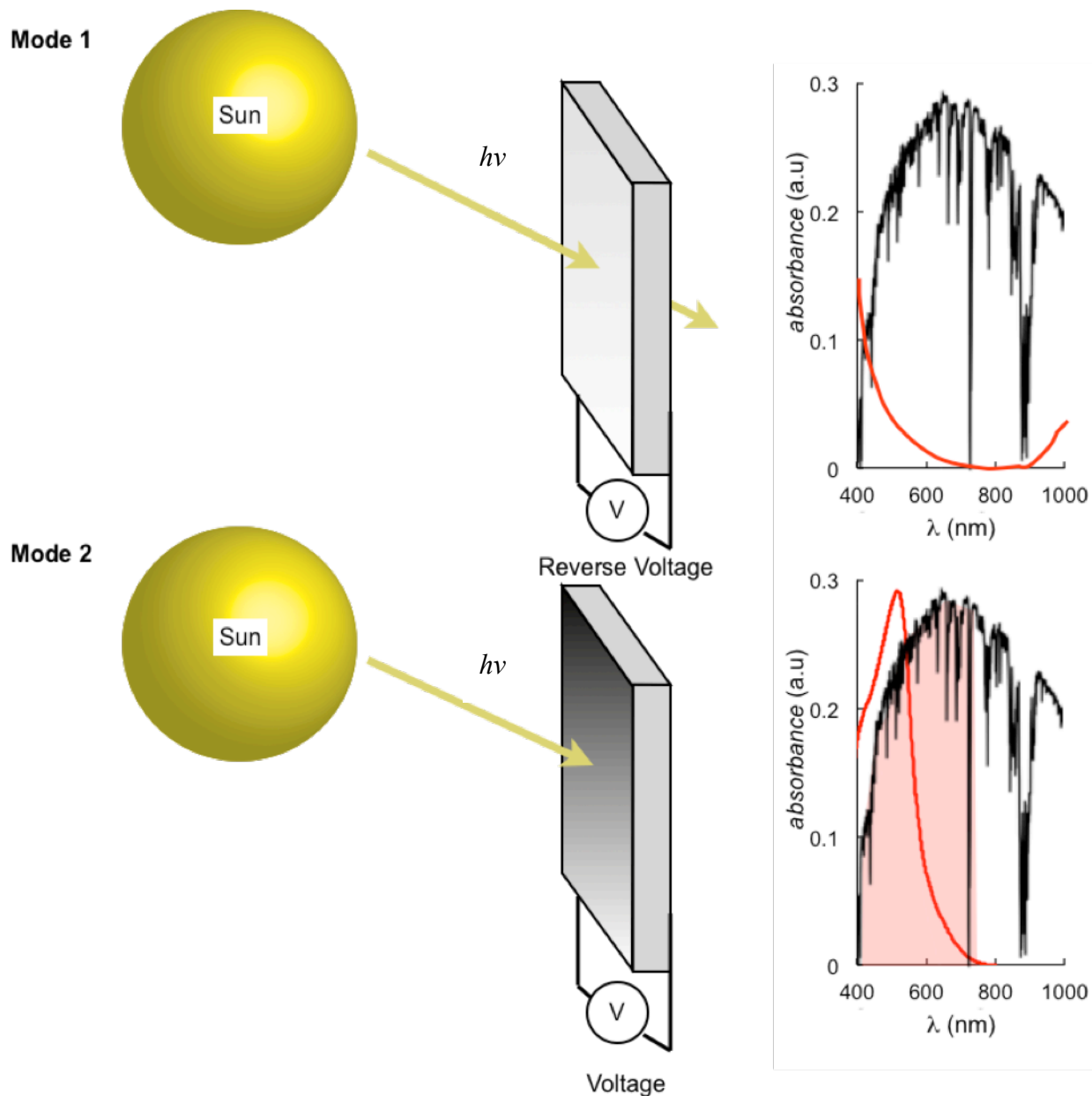


Figure 5.3. Two operational modes of smart window with solar spectrum overlaid with absorption spectrum of 4.1/TiO₂ and predicted transparent mode 1 window.

Over the better part of the last three decades, research into light-harvesters for the DSSC has been dominated by either ruthenium complexes or more recently organic molecules and porphyrins.¹⁹⁹ Staying with the d^6 metals, iron could potentially be used as a substitute for ruthenium and is abundant and cost effective for wide scale utilization. Unfortunately, these complexes suffer from extremely short lived MLCT states and are deactivated by the MC states in the 100 fs regime.²⁰⁰⁻²⁰⁷ There has been reports of ultrafast electron injection into TiO_2 by anchored Fe complexes.^{208,209} In 2015, the seminal paper by Tobias *et al.* demonstrated a N-heterocyclic carbene (NHC) ligand that used the same strategy described in Chapter 2 to prolong the excited state lifetimes of $^3\text{MLCT}$ states through destabilizing the ^3MC state.²¹⁰ They reported a near unity electron-injection efficiency with complexes that exhibited lifetimes in ~ 10 ps time regime, but contend that longer lifetimes are required for most applications. Figure 5.4 shows a proposed complex utilizing the $\text{C}^{\wedge}\text{N}^{\wedge}\text{C}$ scaffold for prolonging the excited state lifetime of iron polypyridyl complexes for application in the DSSC.

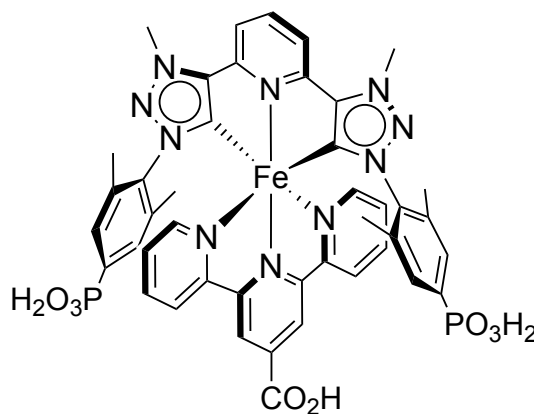


Figure 5.4 Proposed $\text{Fe}(\text{terpy-CO}_2\text{H})(\text{C}^{\wedge}\text{N}^{\wedge}\text{C-PO}_3\text{H}_2)$ complex

Appendix 1

1.1. Experimental Details and Supporting Information for Chapter Two (*J. Am. Chem. Soc.*, 2012, 134, 12354–12357)

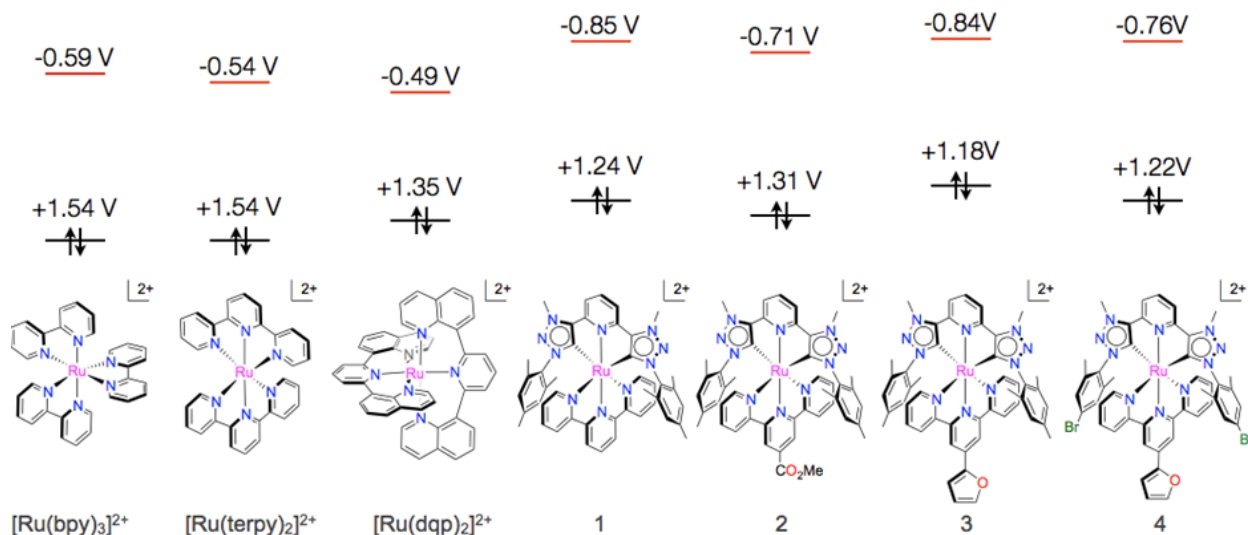


Figure A1.1 Energies (reported vs NHE) of HOMOs (black) and LUMOs (red) of benchmark complexes and **2.1-2.4**. The energies of the lowest excited states are approximated as $E_{1/2,ox} + E_{0-0}$. Adapted with permission from *J. Am. Chem. Soc.*, 2012, 134 (30), pp 12354–12357. Copyright 2017 American Chemical Society.



Title: Bis(tridentate) Ruthenium–
Terpyridine Complexes Featuring
Microsecond Excited-State
Lifetimes

Author: Douglas G. Brown, Nawaporn
Sanguantrakun, Benjamin
Schulze, et al

Publication: Journal of the American
Chemical Society

Publisher: American Chemical Society

Date: Aug 1, 2012

Copyright © 2012, American Chemical Society

LOGIN

If you're a **copyright.com**
user, you can login to
RightsLink using your
copyright.com credentials.
Already a **RightsLink** user or
want to [learn more?](#)

PERMISSION/LICENSE IS GRANTED FOR YOUR ORDER AT NO CHARGE

This type of permission/license, instead of the standard Terms & Conditions, is sent to you because no fee is being charged for your order. Please note the following:

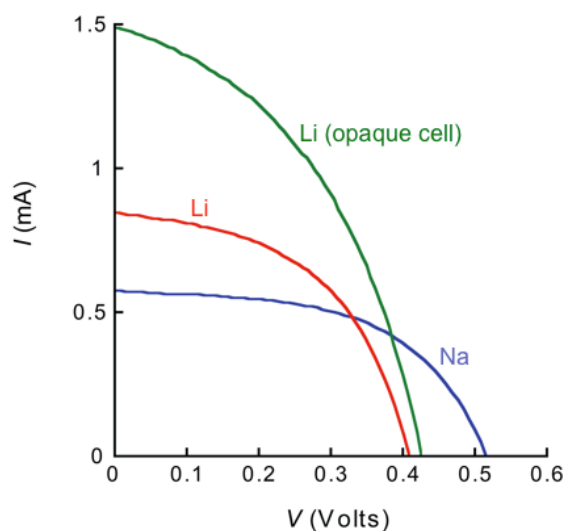
- Permission is granted for your request in both print and electronic formats, and translations.
- If figures and/or tables were requested, they may be adapted or used in part.
- Please print this page for your records and send a copy of it to your publisher/graduate school.
- Appropriate credit for the requested material should be given as follows: "Reprinted (adapted) with permission from (COMPLETE REFERENCE CITATION). Copyright (YEAR) American Chemical Society." Insert appropriate information in place of the capitalized words.
- One-time permission is granted only for the use specified in your request. No additional uses are granted (such as derivative works or other editions). For any other uses, please submit a new request.

1.2. Experimental Details and Supporting Information for Chapter Three (*J. Am. Chem. Soc.*, 2013, 135, 1692–1695)

Table A1.1 Photophysical and electrochemical data for **3.1-3.4/TiO₂**.

	3.1	3.2	3.3	3.4
λ_{abs} (nm) ^a	467	488	462	463
E_{ox} (V) ^b	1.17	1.61	1.18	1.21
E_{ox}^* (V) ^{b,c}	-0.85	-0.47	-0.91	-0.78
E_{0-0} (eV) ^d	2.02	2.07	2.09	1.99

^a The lowest energy ¹MLCT absorption maxima. ^b Measured with 0.1 M NBu₄BF₄ in MeCN using the dye-dipped FTO/TiO₂ substrate as working electrode and the [oFc]⁺/[oFc]⁰ redox couple as an internal standard (0.29 V vs NHE). ^c Calculated as $E_{\text{ox}}^* = E_{\text{ox}} - E_{0-0}$. ^d Determined by the intersection point of the absorption and emission curve of corresponding esters, where the latter is normalized to the lowest energy ¹MLCT band. Reprinted with permission from *J. Am. Chem. Soc.*, 2013, 135 (5), pp 1692–1695. Copyright 2017 American Chemical Society.

**Figure A1.2** Current–voltage curves recorded under AM1.5 conditions for complex **3.4** with electrolyte **E45** (blue) and **E50** (red) and opaque cell with **E50** (green). **E45** electrolyte is

identical to **E50** except that 1.0 M LiI is replaced by 0.6 M NaI. The opaque cell contained an opaque 12 μm titania film of large and small nanoparticles. The decreased voltage consequent of the lithium-based **E50** electrolyte compared to the sodium-based **E45** electrolyte is compensated by a higher current. Use of the opaque titania layer increased cell efficiency by 50% and demonstrates that device efficiency is limited by inherently poor light-harvesting of the dye. Reprinted with permission from *J. Am. Chem. Soc.*, 2013, 135 (5), pp 1692–1695. Copyright 2017 American Chemical Society.

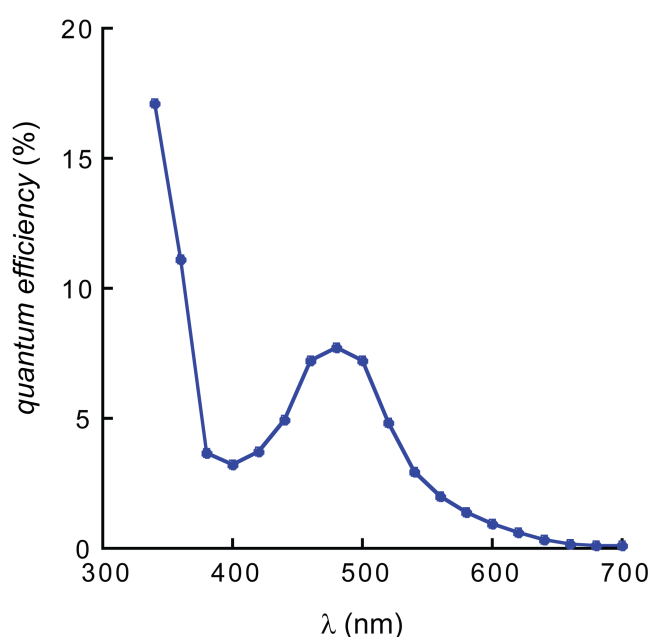


Figure A1.3 IPCE data for **3.4** absorbed to a mesoporous TiO_2 substrate. Measurement conditions: AM1.5 with a 0.88 cm^2 active area. An opaque cell was used that contained an opaque 12 μm titania film of large and small nanoparticles. Reprinted with permission from *J. Am. Chem. Soc.*, 2013, 135 (5), pp 1692–1695. Copyright 2017 American Chemical Society.

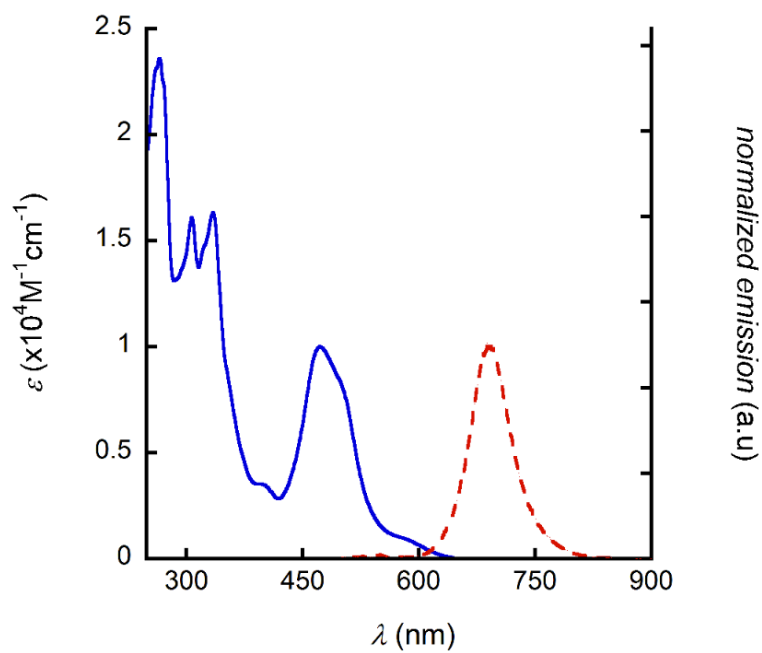


Figure A1.4 Complex **3.1'** absorbance and emission spectra in CH_3CN ($\lambda_{\text{exc}} = 470$ nm).

Reprinted with permission from *J. Am. Chem. Soc.*, 2013, *135* (5), pp 1692–1695. Copyright

2017 American Chemical Society.

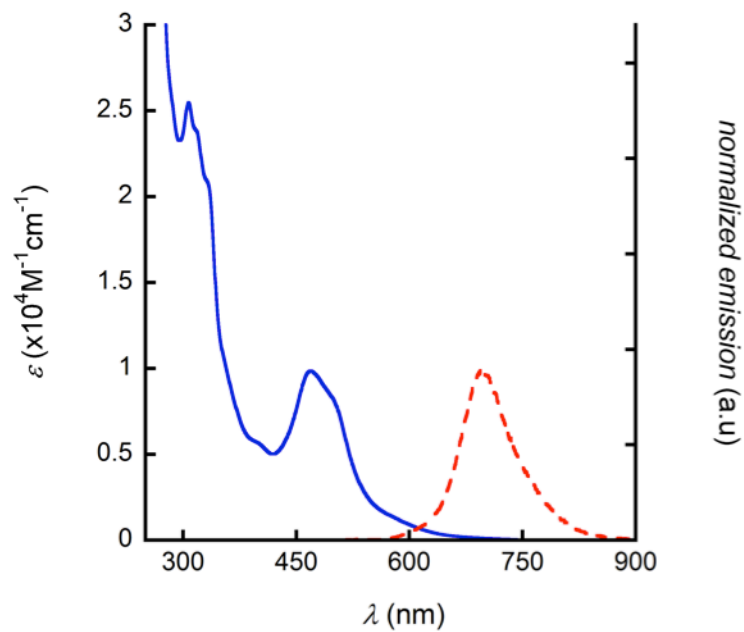


Figure A1.5 Complex **3.2'** absorbance and emission spectra in CH_3CN ($\lambda_{\text{exc}} = 470$ nm). Reprinted with permission from *J. Am. Chem. Soc.*, 2013, *135* (5), pp 1692–1695. Copyright 2017 American Chemical Society.

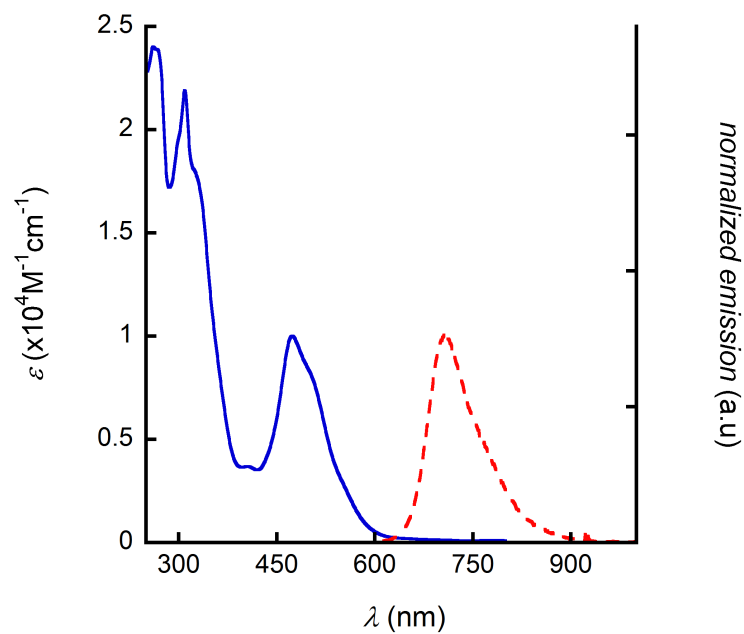


Figure A1.6 Complex **3.3'** absorbance and emission spectra in CH_3CN ($\lambda_{\text{exc}} = 463\text{nm}$). Reprinted with permission from *J. Am. Chem. Soc.*, 2013, 135 (5), pp 1692–1695. Copyright 2017 American Chemical Society.

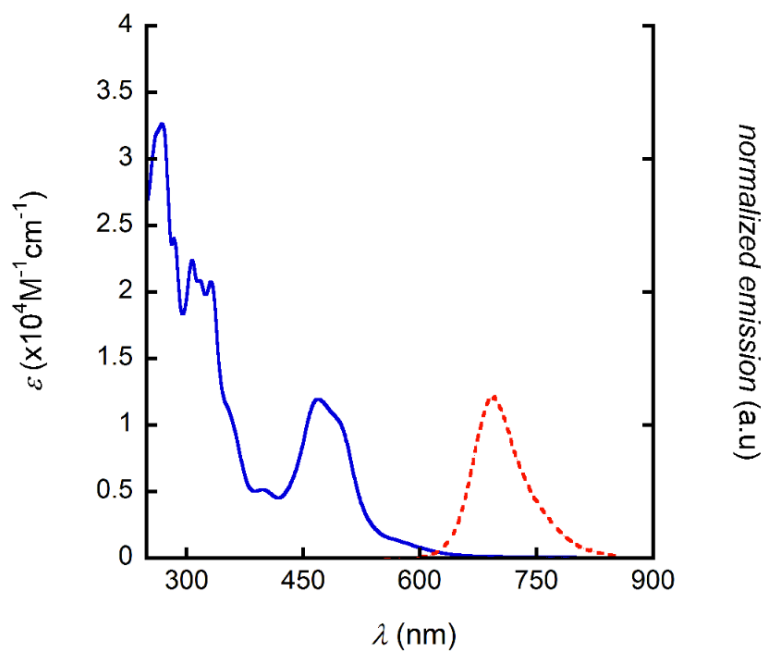


Figure A1.7 Complex **3.4'** absorbance and emission spectra in CH₃CN ($\lambda_{\text{exc}} = 465$ nm).

Reprinted with permission from *J. Am. Chem. Soc.*, 2013, *135* (5), pp 1692–1695. Copyright

2017 American Chemical Society.

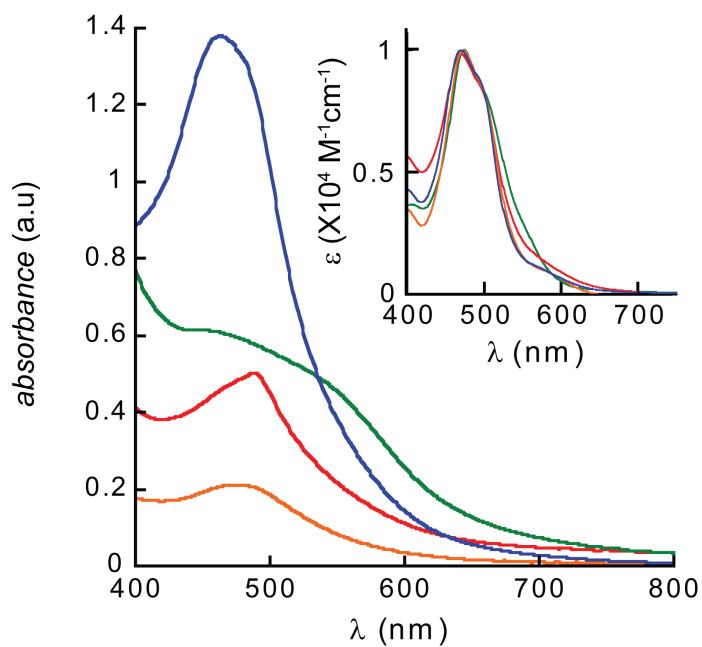


Figure A1.8 UV-Vis absorbance spectra of complexes **3.1-3.4/TiO₂**; *inset*: ester complexes **3.1'-3.4'** in CH₃CN (*inset*). **3.1** (orange), **3.2** (red), **3.3** (green) and **3.4** (blue). Reprinted with permission from *J. Am. Chem. Soc.*, 2013, 135 (5), pp 1692–1695. Copyright 2017 American Chemical Society.

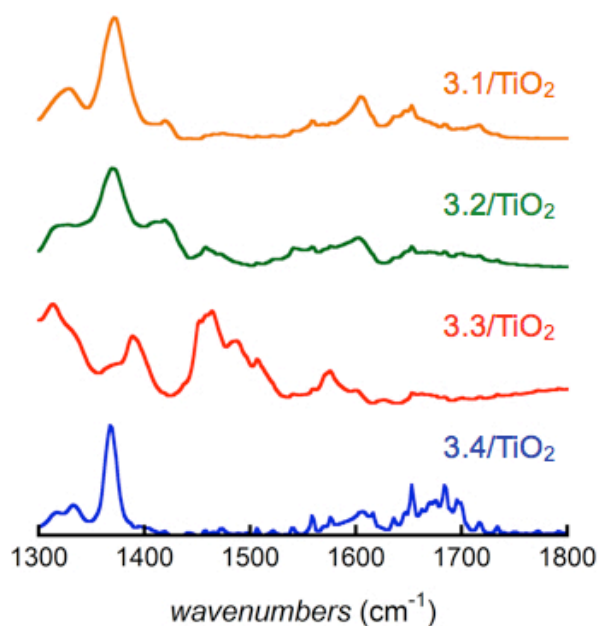


Figure A1.9 Expanded view of DRIFTS spectra for complexes **3.1-3.4/TiO₂**. Reprinted with permission from *J. Am. Chem. Soc.*, 2013, 135 (5), pp 1692–1695. Copyright 2017 American Chemical Society.

All calculations were carried out using the Gaussian 09 software package²¹¹ and visualised with GaussView.²¹² The geometries for complexes **3.1'-3.4'** were optimised with the B3LYP functional, employing the pseudopotential LANL2DZ basis set²¹³⁻²¹⁵ for ruthenium and the 6-31G* basis set^{216,217} for all remaining atoms. Frequency calculations were carried out on the optimised geometries and all model systems were shown to have no imaginary frequencies. TD-DFT calculations were carried out on the optimised geometries employing the IEFPCM solvation model for MeOH.²¹⁸ Orbital population analysis was carried out using the GaussSum2 software suite.²¹⁹ This research was enabled by the use of computing resources provided by WestGrid and Compute/Calcul Canada.

Table A1.2 Fragment orbital analysis for Ester Complexes **3.1'**-**3.4'** as determined from DFT calculations.

<i>MO</i>	3.1'	% contribution			3.2'	% contribution			3.3'	% contribution			3.4'	% contribution		
	<i>eV</i>	<i>Ru</i>	<i>terpy</i>	<i>CNC</i>												
L+10	-4.66	7	3	90	-4.81	17	8	75	-4.70	59	36	5	-5.04	1	3	95
L+9	-4.83	64	27	9	-4.90	53	21	25	-5.05	2	3	95	-5.07	3	2	95
L+8	-5.15	5	2	94	-5.22	5	2	94	-5.07	4	4	92	-5.17	3	5	92
L+7	-5.54	2	98	0	-5.58	2	98	0	-5.16	2	5	94	-5.36	2	92	6
L+6	-5.8	5	1	95	-5.87	5	1	95	-5.70	2	95	4	-5.74	2	94	5
L+5	-5.83	2	95	3	-5.88	2	95	3	-5.72	2	97	1	-5.79	5	5	90
L+4	-5.94	1	99	0	-5.99	1	98	0	-5.75	5	1	94	-5.81	2	94	4
L+3	-6.76	2	70	28	-6.81	2	83	15	-6.55	1	96	2	-6.60	1	97	2
L+2	-6.79	0	28	72	-6.86	0	15	85	-6.68	7	89	4	-6.77	0	2	97
L+1	-6.88	5	1	94	-6.94	5	1	94	-6.73	0	2	98	-6.84	8	84	8
LUMO	-7.00	9	88	3	-7.05	9	88	3	-6.81	5	1	94	-6.85	5	4	90
HOMO	-10.32	60	12	28	-10.39	60	12	28	-10.17	62	18	19	-10.23	61	17	23
H-1	-10.36	63	24	13	-10.43	63	24	13	-10.20	63	17	21	-10.28	63	19	19
H-2	-10.69	78	8	14	-10.74	78	8	14	-10.52	78	8	14	-10.60	78	8	14
H-3	-10.85	0	1	98	-10.97	0	2	97	-10.84	0	1	98	-10.85	0	0	99
H-4	-10.86	0	0	100	-10.99	0	0	100	-10.91	0	3	96	-10.91	0	2	98
H-5	-10.99	0	0	100	-11.20	0	0	100	-10.96	0	0	100	-10.96	0	1	100

H-6	-10.91	0	0	99	-11.31	0	0	100	-11.03	0	5	95	-11.04	0	3	97
H-7	-11.54	0	87	13	-11.60	0	88	12	-11.06	0	0	99	-11.08	0	0	99
H-8	-11.77	0	100	0	-11.78	0	100	0	-11.20	0	1	100	-11.16	0	0	99
H-9	-11.82	13	19	67	-11.88	13	18	69	-11.25	0	1	99	-11.20	0	14	85
H-10	-12.24	0	2	98	-12.30	0	100	0	-11.37	0	79	21	-11.36	0	4	97

Table A1.3 Fragment orbital analysis for Acid Complexes **3.1-3.4** as determined from DFT calculations

<i>MO</i>	3.1	% contribution			3.2	% contribution			3.3	% contribution			3.4	% contribution		
	<i>eV</i>	<i>Ru</i>	<i>terpy</i>	<i>CNC</i>												
L+10	-4.71	7	3	90	-4.87	12	6	82	-4.85	15	79	4	-5.33	1	0	98
L+9	-4.90	65	27	8	-4.98	58	24	18	-5.21	5	3	93	-5.36	4	2	94
L+8	-5.21	4	2	94	-5.28	5	2	94	-5.29	1	3	95	-5.50	1	9	90
L+7	-5.67	2	98	0	-5.72	2	98	0	-5.42	1	3	96	-5.76	2	89	8
L+6	-5.86	5	1	95	-5.93	5	1	95	-5.84	2	95	3	-5.97	2	93	5
L+5	-5.89	2	95	3	-5.95	2	95	3	-5.86	2	97	0	-6.02	5	2	93
L+4	-6.03	1	99	0	-6.09	1	99	0	-5.88	5	1	95	-6.12	1	98	1
L+3	-6.83	1	22	77	-6.89	1	34	65	-6.70	1	96	3	-6.88	2	93	5
L+2	-6.87	1	77	22	-6.93	0	64	36	-6.82	7	89	4	-6.98	0	3	97
L+1	-6.94	5	1	94	-7.00	5	1	93	-6.85	0	2	98	-7.07	5	4	91

LUMO	-7.12	10	87	3	-7.17	9	87	3	-6.93	5	1	94	-7.19	9	87	3
HOMO	-10.40	59	12	29	-10.46	60	12	29	-10.32	61	14	25	-10.51	60	12	28
H-1	-10.45	62	25	14	-10.52	62	25	13	-10.33	64	20	16	-10.55	63	23	13
H-2	-10.77	79	8	13	-10.83	79	8	13	-10.65	78	8	14	-10.86	78	8	14
H-3	-10.89	1	1	98	-11.02	0	1	98	-11.09	0	4	95	-11.15	0	0	99
H-4	-10.91	0	0	100	-11.04	0	0	100	-11.20	0	7	92	-11.28	0	7	92
H-5	-10.94	0	0	100	-11.34	0	0	99	-11.31	0	0	100	-11.33	0	0	100
H-6	-10.95	0	0	99	-11.36	0	0	100	-11.40	0	0	100	-11.54	0	0	100
H-7	-11.64	0	85	14	-11.69	0	86	14	-11.51	0	78	22	-11.64	0	2	97
H-8	-11.88	13	22	65	-11.95	13	21	67	-11.54	0	2	98	-11.68	0	1	99
H-9	-12.09	0	100	0	-12.10	0	100	0	-11.67	0	0	100	-11.72	0	83	17
H-10	-12.30	0	2	98	-12.37	0	2	98	-11.71	0	2	97	-12.01	12	16	72

Table A1.4 Summary of key TD-DFT transitions ($f > 0.01$) and corresponding change in fragment orbital contributions associated with the transition.

3.1'	Trans #	λ (nm)	f	Major contributions	Change in population		
					Ru	terpy	CNC
	3	469	0.0437	H-1→LUMO (56%), HOMO→L+1 (41%)	-54	+32	+22
	4	459	0.0150	HOMO→L+2 (96%)	-60	+15	+44
	5	444	0.0382	H-1→L+1 (97%)	-58	-23	+80
	7	426	0.1715	H-1→LUMO (34%), HOMO→L+1 (55%)	-56	+18	+38
	12	379	0.0656	H-2→L+2 (72%), HOMO→L+3 (16%)	-74	+28	+46
	15	339	0.0366	H-3→LUMO (17%), HOMO→L+4 (72%)	-42	+81	-38
	18	334	0.0416	H-1→L+4 (91%)	-59	+75	-16
	21	326	0.0366	H-1→L+6 (39%), HOMO→L+6 (51%)	-56	-16	+73
	22	326	0.0313	H-1→L+6 (49%), HOMO→L+6 (40%)	-56	-17	+75
	24	320	0.0512	HOMO→L+5 (86%)	-55	+78	-24
	26	319	0.1455	H-7→LUMO (75%)	-6	+13	-7
	35	305	0.1880	H-8→LUMO (61%), HOMO→L+7 (29%)	-11	+19	-7
	38	304	0.0336	H-1→L+7 (88%)	-62	+67	-6
	41	295	0.1059	H-8→L+2 (13%), H-7→L+2 (43%), H-4→L+3 (28%)	-1	-15	+16
	43	292	0.0480	H-8→L+2 (15%), H-7→L+2 (17%), H-4→L+3 (46%), H-3→L+2 (17%)	+1	+18	-17
	47	288	0.0413	H-8→L+1 (46%), H-7→L+1 (46%)	+3	-90	+87

48	284	0.0171	H-1→L+9 (18%), H-1→L+14 (64%)	-29	-19	+48
50	282	0.0205	H-8→L+2 (62%), H-7→L+2 (32%)	-2	-66	+68
3.2'						
Trans #	λ (nm)	f	Major contributions	Ru	terpy	CNC
3	467	0.0431	H-1→LUMO (55%), HOMO→L+1 (42%)	-55	+31	+23
4	456	0.0151	HOMO→L+2 (96%)	-60	+3	+57
5	441	0.0375	H-1→L+1 (97%)	-58	-23	+81
7	425	0.1762	H-1→LUMO (35%), HOMO→L+1 (54%)	-56	+17	+39
12	378	0.0641	H-2→L+2 (72%), HOMO→L+3 (17%)	-74	+20	+53
15	338	0.0357	H-3→LUMO (25%), HOMO→L+4 (62%)	-35	+87	-52
18	332	0.0403	H-1→L+4 (93%)	-62	+75	-13
19	326	0.0649	HOMO→L+6 (88%)	-55	-11	+66
22	319	0.0514	HOMO→L+5 (86%)	-58	+82	-24
23	318	0.1401	H-5→LUMO (60%), H-1→L+5 (20%)	-16	+77	-62
30	310	0.0263	H-8→LUMO (43%), HOMO→L+7 (51%)	-29	+42	-14
31	305	0.1797	H-8→LUMO (49%), HOMO→L+7 (43%)	-21	+35	-14
34	302	0.0321	H-2→L+6 (48%), H-1→L+7 (42%)	-65	+30	+35
37	294	0.1266	H-8→L+2 (18%), H-5→L+2 (53%), H-4→L+3 (15%)	-3	+5	-2
41	290	0.0203	H-8→L+2 (12%), H-4→L+3 (59%), H-3→L+2 (20%)	+1	+44	-45
42	288	0.0452	H-8→L+1 (47%), H-5→L+1 (44%)	+3	-49	+46

46	284	0.0190	H-1→L+8 (22%), H-1→L+14 (60%)	-43	-21	+63
48	282	0.0185	H-8→L+2 (59%), H-5→L+2 (34%)	-2	-44	+46
3.3'						
Trans #	λ (nm)	f	Major contributions	Ru	terpy	CNC
2	471	0.0131	HOMO→L+1 (85%), HOMO→L+2 (11%)	-61	-6	+67
6	443	0.0403	H-1→L+2 (80%)	-57	+64	-8
8	423	0.1077	H-2→L+1 (17%), H-1→LUMO (33%), HOMO→L+2 (28%)	-62	+24	+37
9	419	0.0306	H-1→L+3 (18%), HOMO→L+2 (15%), HOMO→L+3 (48%)	-61	+67	-6
12	389	0.0525	H-2→L+1 (55%), H-2→L+2 (12%), HOMO→L+3 (17%)	-72	+19	+53
15	335	0.0468	HOMO→L+4 (49%), HOMO→L+5 (13%), HOMO→L+13 (27%)	-59	-2	+61
16	334	0.0227	H-1→L+4 (19%), HOMO→L+4 (18%), HOMO→L+13 (36%)	-59	-11	+71
20	323	0.0410	H-1→L+6 (14%), HOMO→L+6 (75%)	-61	+74	-14
26	312	0.0138	H-2→L+5 (11%), H-1→L+8 (64%)	-57	0	+56
27	311	0.1681	H-3→LUMO (71%), HOMO→L+8 (12%)	-9	+1	+8
30	302	0.0541	H-3→L+1 (83%)	0	+5	-5
31	298	0.0116	H-5→L+2 (14%), H-3→L+2 (67%)	+6	+76	-83
33	295	0.0281	H-5→LUMO (88%)	+5	-1	-4
34	294	0.0191	H-3→L+3 (71%)	-1	+77	-76
37	292	0.0817	H-6→L+1 (30%), H-5→L+1 (23%)	-11	+13	-3
40	288	0.1555	H-6→LUMO (89%)	+5	-4	-1

43	283	0.0110	H-7→LUMO (93%)	+5	+1	-6
44	283	0.0261	H-6→L+1 (11%), H-5→L+2 (40%), H-5→L+3 (10%)	+2	+68	-72
45	282	0.0145	H-1→L+15 (51%), H-1→L+16 (14%)	-21	+3	+16
3.4'						
Trans #	λ (nm)	f	Major contributions	Ru	terpy	CNC
3	466	0.0412	H-1→LUMO (54%), HOMO→L+1 (39%)	-56	+19	+37
4	461	0.0163	HOMO→L+2 (93%)	-61	-15	+75
5	443	0.0121	H-1→L+1 (39%), H-1→L+2 (54%)	-59	+19	+40
6	441	0.0297	H-1→L+1 (44%), H-1→L+2 (42%)	-57	+29	+29
7	424	0.1526	H-1→LUMO (27%), H-1→L+1 (13%), HOMO→L+1 (44%)	-57	+35	+21
12	382	0.0610	H-2→L+2 (70%), HOMO→L+3 (15%)	-74	+8	+66
16	333	0.0316	H-1→L+5 (13%), HOMO→L+5 (54%), HOMO→L+13 (14%)	-57	-6	+63
17	332	0.0351	H-1→L+4 (78%), HOMO→L+5 (11%)	-58	+63	-4
18	329	0.0347	H-1→L+5 (57%), HOMO→L+5 (20%)	-58	-13	+72
19	326	0.0772	H-3→LUMO (67%), HOMO→L+4 (12%)	-12	+19	-8
20	323	0.0331	H-1→L+6 (40%), HOMO→L+6 (49%)	-57	+74	-16
21	319	0.0121	H-4→LUMO (77%)	-8	+16	-9
22	319	0.0301	H-4→LUMO (21%), H-1→L+6 (39%), HOMO→L+6 (31%)	-46	+60	-14
24	314	0.0834	H-5→LUMO (81%)	-2	+5	-3
29	306	0.0126	H-6→LUMO (10%), H-2→L+5 (53%), HOMO→L+9 (10%)	-60	-6	+67

31	304	0.0116	H-1→L+8 (10%), HOMO→L+8 (20%), HOMO→L+9 (39%)	-53	-9	+62
32	303	0.0173	H-5→L+1 (14%), H-3→L+1 (62%)	+3	+71	-74
34	302	0.1266	H-6→LUMO (56%), HOMO→L+9 (26%)	-12	+4	+9
35	299	0.0128	H-7→LUMO (48%), H-4→L+1 (17%), H-1→L+9 (24%)	-13	+13	0
37	298	0.0459	H-7→LUMO (19%), H-3→L+2 (32%), H-1→L+9 (24%)	-14	+6	+8
38	298	0.0428	H-3→L+2 (39%), H-1→L+9 (29%)	-21	+7	+14
40	292	0.0269	H-5→L+2 (10%), H-4→L+2 (30%), H-3→L+3 (45%)	+1	+50	-51
41	291	0.0523	H-6→L+2 (19%), H-5→L+2 (27%), H-4→L+2 (14%), H-4→L+3 (13%), H-3→L+2 (10%)	-2	+20	-18
44	286	0.0261	H-6→L+1 (32%), H-5→L+1 (31%)	-2	+72	-70
45	285	0.0299	H-6→L+2 (26%), H-4→L+2 (14%), H-4→L+3 (13%), H-3→L+3 (18%)	-2	+40	-37

All complexes were dark red, needle shaped, and were coated with Paratone 8277 oil (Exxon) and mounted on a glass fiber. All measurements were made on a Nonius KappaCCD diffractometer with graphite monochromated Mo-K α radiation at 173(2) K. Details of crystal data, data collection^{220,221} and structure refinement have been provided in Table A1.5. The data were corrected for Lorentz and polarization effects and for absorption using multi-scan methods.²²⁰ The structure was solved by the direct methods²²² and expanded using Fourier techniques.²²³ The non-hydrogen atoms were refined anisotropically. The hydrogen atoms were included at geometrically idealized positions and were not refined. The final cycle of full-matrix least-squares refinement was performed utilizing SHELXL97.²²⁴ The weighting scheme was based on counting statistics and the final difference map had no chemically significant features. The PLATON/SQUEEZE program²²⁵ was employed to deal with disordered and partial occupancy (MeOH/Et₂O) molecules of solvation.

All molecular structures are presented with thermal ellipsoids plotted at the 50% probability level. Hydrogen atoms, ester alkyl chains, solvent molecules and anions have been omitted for clarity.

Table A1.5 Crystal data and structure refinement parameters

	3.1'	3.3'	3.4'
Empirical formula	C ₄₆ H ₄₄ B ₂ F ₈ N ₁₀ O ₂ Ru	C ₅₀ H ₅₆ B ₂ F ₈ N ₁₀ O ₆ P ₂ Ru	C ₅₂ H ₅₈ B ₂ F ₈ N ₁₀ O ₈ P ₂ Ru
Formula weight (<i>Da</i>)	1043.60	1229.68	1287.71
Crystal system	Monoclinic	Monoclinic	Monoclinic
Space group	P2 ₁ /c	P2 ₁ /c	C2/c
a (Å)	15.4783(3)	13.0493(2)	17.6552(4)
b (Å)	14.6562(3)	18.9726(4)	16.7076(6)
c (Å)	27.0866(5)	23.3282(5)	21.9443(2)
β (°)	122.2810(10)	106.6110(10)	107.569(2)
Volume (Å³)	5194.95(18)	5534.55(19)	6171.1(3)
Z	4	4	4
D_C (g cm⁻³)	1.334	1.476	1.386
μ (mm⁻¹)	0.376	0.425	0.387
F(000)	2128	2520	2640
Crystal size (mm³)	0.14 x 0.06 x 0.04	0.08 x 0.06 x 0.06	0.05 x 0.04 x 0.03
θ_{min}, θ_{max} (°)	2.26, 26.00	2.33, 25.00	1.78, 25.00
Index ranges	-19 ≤ h ≤ 19, -18 ≤ k ≤ 18, -33 ≤ l ≤ 33	-15 ≤ h ≤ 15, -22 ≤ k ≤ 22, -27 ≤ l ≤ 27	-20 ≤ h ≤ 20, -19 ≤ k ≤ 19, -26 ≤ l ≤ 26
N_t	34922	18225	10290
N (R_{int})	10186 (0.0649)	9616 (0.0402)	5391 (0.0321)
Completeness to θ = 26.00°	99.7 %	98.5 %	99.2 %
Max. and min. transmission	0.9851, 0.9492	0.9749, 0.9668	0.9885, 0.9809
Data / restraints / parameters	10186 / 0 / 622	9616 / 1 / 736	5391 / 4 / 399
Goodness-of-fit on F²	1.112	1.083	1.057
R1 (wR2) [I > 2σ(I)]	0.0659 (0.1643)	0.0664 (0.1621)	0.0789 (0.2094)
R1 (wR2) [all data]	0.0806 (0.1738)	0.0841 (0.1756)	0.0886 (0.2189)
Largest diff. peak and hole (e Å⁻³)	0.777, -0.632	0.759, -0.815	1.268, -0.706



Title: Stabilization of Ruthenium Sensitizers to TiO₂ Surfaces through Cooperative Anchoring Groups

Author: Douglas G. Brown, Phil A. Schauer, Javier Borau-Garcia, et al

Publication: Journal of the American Chemical Society

Publisher: American Chemical Society

Date: Feb 1, 2013

Copyright © 2013, American Chemical Society

LOGIN

If you're a **copyright.com** user, you can login to RightsLink using your copyright.com credentials. Already a **RightsLink** user or want to [learn more?](#)

PERMISSION/LICENSE IS GRANTED FOR YOUR ORDER AT NO CHARGE

This type of permission/license, instead of the standard Terms & Conditions, is sent to you because no fee is being charged for your order. Please note the following:

- Permission is granted for your request in both print and electronic formats, and translations.
- If figures and/or tables were requested, they may be adapted or used in part.
- Please print this page for your records and send a copy of it to your publisher/graduate school.
- Appropriate credit for the requested material should be given as follows: "Reprinted (adapted) with permission from (COMPLETE REFERENCE CITATION). Copyright (YEAR) American Chemical Society." Insert appropriate information in place of the capitalized words.
- One-time permission is granted only for the use specified in your request. No additional uses are granted (such as derivative works or other editions). For any other uses, please submit a new request.



Title: Physicochemical Analysis of Ruthenium(II) Sensitizers of 1,2,3-Triazole-Derived Mesoionic Carbene and Cyclometalating Ligands

Author: Stephan Sinn, Benjamin Schulze, Christian Friebe, et al

Publication: Inorganic Chemistry

Publisher: American Chemical Society

Date: Feb 1, 2014

Copyright © 2014, American Chemical Society

LOGIN
If you're a [copyright.com user](#), you can login to RightsLink using your copyright.com credentials. Already a [RightsLink user](#) or want to [learn more?](#)

PERMISSION/LICENSE IS GRANTED FOR YOUR ORDER AT NO CHARGE

This type of permission/license, instead of the standard Terms & Conditions, is sent to you because no fee is being charged for your order. Please note the following:

- Permission is granted for your request in both print and electronic formats, and translations.
- If figures and/or tables were requested, they may be adapted or used in part.
- Please print this page for your records and send a copy of it to your publisher/graduate school.
- Appropriate credit for the requested material should be given as follows: "Reprinted (adapted) with permission from (COMPLETE REFERENCE CITATION). Copyright (YEAR) American Chemical Society." Insert appropriate information in place of the capitalized words.
- One-time permission is granted only for the use specified in your request. No additional uses are granted (such as derivative works or other editions). For any other uses, please submit a new request.

References

1. Targowski, A., *Geo UERJ* **2015**, (27), 378-397.
2. Levy, B., *Int. Bus. Rev.* **2007**, 16 (5), 594-612.
3. Dunning, J. H., *Transnational Corporations* **2006**, 15 (1), 173-227.
4. Development, U. S. A. I. Energy Security and Conflict: A country-Level Review of the issues. http://pdf.usaid.gov/pdf_docs/Pnadw664.pdf (accessed March 5).
5. Brenner, M. The Geo-Politics of Energy. <https://energy.utexas.edu/the-geo-politics-of-energy/> (accessed March 5).
6. Perrow, C., *Contemp. Sociol.-J. Rev.* **2010**, 39 (1), 46-47.
7. Agency, U. S. E. P. Causes of Climate Change. <https://www.epa.gov/climate-change-science/causes-climate-change> (accessed March 5).
8. Edinger, R.; Kaul, S., *Renew. Sust. Energ. Rev.* **2000**, 4 (3), 295-313.
9. *Communicating sustainability for the green economy / Lynn R. Kahle and Eda Gurel-Atay, editors*. M.E. Sharpe: Armonk, New York, 2014.
10. Administration, U. S. E. I. Annual Energy Outlook 2012 Early Release. [http://www.eia.gov/outlooks/aeo/pdf/0383\(2012\).pdf](http://www.eia.gov/outlooks/aeo/pdf/0383(2012).pdf) (accessed December 11).
11. Administration, U. S. E. I. Monthly Electric Generator Inventory. http://www.eia.gov/energyexplained/index.cfm?page=electricity_in_the_united_states (accessed December 12).
12. Li, J.; Geng, X.; Li, J., *Sustainability* **2016**, 8 (12), 1276.
13. Panwar, N. L.; Kaushik, S. C.; Kothari, S., *Renew. Sust. Energ. Rev.* **2011**, 15 (3), 1513-1524.
14. Ellabban, O.; Abu-Rub, H.; Blaabjerg, F., *Renew. Sust. Energ. Rev.* **2014**, 39, 748-764.
15. Ipsakis, D.; Voutetakis, S.; Seferlis, P.; Stergiopoulos, F.; Elmasides, C., *Int. J. Hydrog. Energy* **2009**, 34 (16), 7081-7095.
16. de Vries, B. J. M.; van Vuuren, D. P.; Hoogwijk, M. M., *Energy Policy* **2007**, 35 (4), 2590-2610.
17. Amusat, O. O.; Shearing, P. R.; Fraga, E. S., *Comput. Chem. Eng.* **2016**, 95, 21-37.
18. Dickinson, R. R.; Battye, D. L.; Linton, V. M.; Ashman, P. J.; Nathan, G. J., *Int. J. Hydrog. Energy* **2010**, 35 (3), 1321-1329.
19. Administration, U. S. E. I. How much electricity is lost in transmission and distribution in the United States? <https://www.eia.gov/tools/faqs/faq.cfm?id=105&t=3> (accessed March 5).
20. Lewis, N. S.; Nocera, D. G., *Proc. Natl. Acad. Sci.* **2006**, 103 (43), 15729-15735.
21. Becquerel, A. E., *C. R. Acad. Sci.* **1839**, 9, 561-567.
22. Pickard, W. F.; Shen, A. Q.; Hansing, N. J., *Renew. Sust. Energ. Rev.* **2009**, 13 (8), 1934-1945.
23. Galen, L. B.; Naïm, R. D. *Tracking the Sun IX: The Installed Price of Residential and Non-Residential Photovoltaic Systems in the United States*; 2016.
24. Shahan, Z. Low Costs of Solar Power & Wind Power Crush Coal, Crush Nuclear, & Beat Natural Gas. <https://cleantechnica.com/2016/12/25/cost-of-solar-power-vs-cost-of-wind-power-coal-nuclear-natural-gas/> (accessed April 20).
25. OpenEI database. <http://en.openei.org/apps/TCDB/> (accessed March 5).
26. GCell Smart. Sustainable. Solar. <http://gcell.com> (accessed March 5).

27. Dyesol. <https://www.dyesol.com/> (accessed March 5).
28. Yunaz, I. A.; Kasashima, S.; Inthisang, S.; Krajangsang, T.; Miyajima, S.; Yamada, A.; Konagai, M.; Ieee, EFFECT OF LIGHT INTENSITY ON PERFORMANCE OF SILICON-BASED THIN FILM SOLAR CELLS. In *2009 34th Ieee Photovoltaic Specialists Conference, Vols 1-3*, Ieee: New York, 2009; pp 436-440.
29. O'Regan, B.; Gratzel, M., *Nature* **1991**, 353 (6346), 737-740.
30. Mathew, S.; Yella, A.; Gao, P.; Humphry-Baker, R.; CurchodBasile, F. E.; Ashari-Astani, N.; Tavernelli, I.; Rothlisberger, U.; NazeeruddinMd, K.; Grätzel, M., *Nat. Chem.* **2014**, 6 (3), 242-247.
31. Kakiage, K.; Aoyama, Y.; Yano, T.; Oya, K.; Fujisawa, J.-i.; Hanaya, M., *Chem. Comm.* **2015**, 51 (88), 15894-15897.
32. Burschka, J.; Pellet, N.; Moon, S.-J.; Humphry-Baker, R.; Gao, P.; Nazeeruddin, M. K.; Gratzel, M., *Nature* **2013**, 499 (7458), 316-319.
33. Cook, T. R.; Dogutan, D. K.; Reece, S. Y.; Surendranath, Y.; Teets, T. S.; Nocera, D. G., *Chem. Rev.* **2010**, 110 (11), 6474-6502.
34. Blakemore, J. D.; Crabtree, R. H.; Brudvig, G. W., *Chem. Rev.* **2015**, 115 (23), 12974-13005.
35. Kudo, A., *Int. J. Hydrog. Energy* **2006**, 31 (2), 197-202.
36. Gerischer, H.; Willig, F., Reaction of excited dye molecules at electrodes. In *Physical and Chemical Applications of Dyestuffs*, Schäfer, F. P.; Gerischer, H.; Willig, F.; Meier, H.; Jahnke, H.; Schönborn, M.; Zimmermann, G., Eds. Springer Berlin Heidelberg: Berlin, Heidelberg, 1976; pp 31-84.
37. Gerischer, H.; Michel-Beyerle, M. E.; Rebentrost, F.; Tributsch, H., *Electrochim. Acta* **1968**, 13 (6), 1509-1515.
38. Tributsch, H.; Calvin, M., *Photochem. Photobiol.* **1971**, 14 (2), 95-112.
39. Tributsch, H., *Photochem. Photobiol.* **1972**, 16 (4), 261-269.
40. Spitler, M. T.; Calvin, M., *J. Chem. Phys.* **1977**, 66 (10), 4294-4305.
41. Lane, R. F.; Hubbard, A. T., *J. Phys. Chem.* **1973**, 77 (11), 1401-1410.
42. Moses, P. R.; Wier, L.; Murray, R. W., *Anal. Chem.* **1975**, 47 (12), 1882-1886.
43. Fillinger, A.; Parkinson, B. A., *J. Electrochem. Soc.* **1999**, 146 (12), 4559-4564.
44. Juris, A.; Balzani, V.; Barigelletti, F.; Campagna, S.; Belser, P.; von Zelewsky, A., *Coord. Chem. Rev.* **1988**, 84, 85-277.
45. Dovletoglou, A.; Adeyemi, S. A.; Meyer, T. J., *Inorg. Chem.* **1996**, 35 (14), 4120-4127.
46. Rawling, T.; McDonagh, A., *Coord. Chem. Rev.* **2007**, 251 (9-10), 1128-1157.
47. Campagna, S.; Puntoriero, F.; Nastasi, F.; Bergamini, G.; Balzani, V., Photochemistry and photophysics of coordination compounds: Ruthenium. In *Photochemistry and Photophysics of Coordination Compounds I*, Balzani, V.; Campagna, S., Eds. Springer-Verlag Berlin: Berlin, 2007; Vol. 280, pp 117-214.
48. Kalyanasundaram, K., *Coord. Chem. Rev.* **1982**, 46 (OCT), 159-244.
49. Alstrum-Acevedo, J. H.; Brennaman, M. K.; Meyer, T. J., *Inorg. Chem.* **2005**, 44 (20), 6802-6827.
50. Gu, S. J.; Xu, W. L.; Huang, J. J., *Prog. Chem.* **2013**, 25 (2-3), 330-339.
51. Dragutan, I.; Dragutan, V.; Demonceau, A., *Molecules* **2015**, 20 (9), 17244-17274.
52. Ullrich, B.; Seeger, S.; Wolfrum, J., *J. Organomet. Chem.* **1997**, 541 (1-2), 401-406.

53. Younus, H. A.; Su, W.; Ahmad, N.; Chen, S.; Verpoort, F., *Adv. Synth. Catal.* **2015**, 357 (2-3), 283-330.
54. Ratovelomanana-Vidal, V.; Genet, J. P., *J. Organomet. Chem.* **1998**, 567 (1-2), 163-171.
55. DeRosa, M. C.; Crutchley, R. J., *Coord. Chem. Rev.* **2002**, 233, 351-371.
56. Kalyanasundaram, K.; Gratzel, M., *Coord. Chem. Rev.* **1998**, 177, 347-414.
57. Wang, X. Y.; Del Guerzo, A.; Schmehl, R. H., *J. Photochem. Photobiol. C-Photochem. Rev.* **2004**, 5 (1), 55-77.
58. Medlycott, E. A.; Hanan, G. S., *Coord. Chem. Rev.* **2006**, 250 (13-14), 1763-1782.
59. Fang, Y. Q.; Taylor, N. J.; Laverdiere, F.; Hanan, G. S.; Loiseau, F.; Nastasi, F.; Campagna, S.; Nierengarten, H.; Leize-Wagner, E.; Van Dorselaer, A., *Inorg. Chem.* **2007**, 46 (7), 2854-2863.
60. Vos, J. G.; Kelly, J. M., *Dalton Trans* **2006**, (41), 4869-4883.
61. Kreitner, C.; Heinze, K., *Dalton Trans* **2016**, 45 (35), 13631-13647.
62. Koivisto, B. D.; Robson, K. C. D.; Berlinguette, C. P., *Inorg. Chem.* **2009**, 48 (20), 9644-9652.
63. Harriman, A.; Izzet, G.; Goeb, S.; De Nicola, A.; Ziessel, R., *Inorg. Chem.* **2006**, 45 (24), 9729-9741.
64. Goze, C.; Sabatini, C.; Barbieri, A.; Barigelletti, F.; Ziessel, R., *Inorg. Chem.* **2007**, 46 (18), 7341-7350.
65. Strouse, G. F.; Schoonover, J. R.; Duesing, R.; Boyde, S.; Jones, W. E.; Meyer, T. J., *Inorg. Chem.* **1995**, 34 (2), 473-487.
66. Doppiu, A.; Caijo, F.; Tripoteau, F.; Bompard, S.; Crevisy, C.; Mauduit, M., *Top. Catal.* **2014**, 57 (17-20), 1351-1358.
67. Rao, C. R. K.; Trivedi, D. C., *Coord. Chem. Rev.* **2005**, 249 (5-6), 613-631.
68. Busana, M. G.; Prudenziati, M.; Hormadaly, J., *J. Mater. Sci. Mater. Electron.* **2006**, 17 (11), 951-962.
69. De Cola, L.; Belser, P.; von Zelewsky, A.; Vogtle, F., *Inorg. Chim. Acta.* **2007**, 360 (3), 775-784.
70. Damrauer, N. H.; Cerullo, G.; Yeh, A.; Boussie, T. R.; Shank, C. V.; McCusker, J. K., *Science* **1997**, 275 (5296), 54-57.
71. Wang, J. H.; Fang, Y. Q.; Bourget-Merie, L.; Polson, M. I. J.; Hanan, G. S.; Juris, A.; Loiseau, F.; Campagna, S., *Chem. Eur. J.* **2006**, 12 (33), 8539-8548.
72. Hammarstrom, L.; Johansson, O., *Coord. Chem. Rev.* **2010**, 254 (21-22), 2546-2559.
73. Wolpher, H.; Johansson, O.; Abrahamsson, M.; Kritikos, M.; Sun, L. C.; Akermark, B., *Inorg. Chem. Commun.* **2004**, 7 (3), 337-340.
74. Abrahamsson, M.; Jäger, M.; Österman, T.; Eriksson, L.; Persson, P.; Becker, H.-C.; Johansson, O.; Hammarström, L., *J. Am. Chem. Soc.* **2006**, 128 (39), 12616-12617.
75. Collin, J.-P.; Kayhanian, R.; Sauvage, J.-P.; Calogero, G.; Barigelletti, F.; De Cian, A.; Fischer, J., *Chem. Comm.* **1997**, (8), 775-776.
76. Collin, J.-P.; Beley, M.; Sauvage, J.-P.; Barigelletti, F., *Inorg. Chim. Acta.* **1991**, 186 (1), 91-93.
77. Duati, M.; Fanni, S.; G. Vos, J., *Inorg. Chem. Commun.* **2000**, 3 (2), 68-70.
78. Son, S. U.; Park, K. H.; Lee, Y.-S.; Kim, B. Y.; Choi, C. H.; Lah, M. S.; Jang, Y. H.; Jang, D.-J.; Chung, Y. K., *Inorg. Chem.* **2004**, 43 (22), 6896-6898.

79. Park, H.-J.; Kim, K. H.; Choi, S. Y.; Kim, H.-M.; Lee, W. I.; Kang, Y. K.; Chung, Y. K., *Inorg. Chem.* **2010**, *49* (16), 7340-7352.
80. Schulze, B.; Escudero, D.; Friebe, C.; Siebert, R.; Görls, H.; Köhn, U.; Altuntas, E.; Baumgaertel, A.; Hager, M. D.; Winter, A.; Dietzek, B.; Popp, J.; González, L.; Schubert, U. S., *Chem. Eur. J.* **2011**, *17* (20), 5494-5498.
81. Brown, D. G.; Sangantrakun, N.; Schulze, B.; Schubert, U. S.; Berlinguette, C. P., *J. Am. Chem. Soc.* **2012**, *134* (30), 12354-12357.
82. Jakubikova, E.; Chen, W.; Dattelbaum, D. M.; Rein, F. N.; Rocha, R. C.; Martin, R. L.; Batista, E. R., *Inorg. Chem.* **2009**, *48* (22), 10720-10725.
83. Hagfeldt, A.; Boschloo, G.; Sun, L.; Kloo, L.; Pettersson, H., *Chem. Rev.* **2010**, *110* (11), 6595-6663.
84. Swathy, K. S.; Abraham, P. A.; Panicker, N. R.; Pramanik, N. C.; Jacob, K. S., Nanostructured anatase titania spheres as light scattering layer in Dye-sensitized solar cells. In *International Conference on Emerging Trends in Engineering, Science and Technology*, Viswanathan, C.; Kumar, R. S., Eds. Elsevier Science Bv: Amsterdam, 2016; Vol. 24, pp 767-773.
85. Bakhshayesh, A. M.; Azadfar, S. S.; Bakhshayesh, N., *J. Mater. Sci. Mater. Electron.* **2015**, *26* (12), 9808-9816.
86. Kim, J.-Y.; Kim, J. Y.; Lee, D.-K.; Kim, B.; Kim, H.; Ko, M. J., *J. Phys. Chem. C* **2012**, *116* (43), 22759-22766.
87. Chung, I.; Lee, B.; He, J.; Chang, R. P. H.; Kanatzidis, M. G., *Nature* **2012**, *485* (7399), 486-489.
88. Daeneke, T.; Kwon, T.-H.; Holmes, A. B.; Duffy, N. W.; Bach, U.; Spiccia, L., *Nat. Chem.* **2011**, *3* (3), 211-215.
89. Wu, J.; Lan, Z.; Lin, J.; Huang, M.; Huang, Y.; Fan, L.; Luo, G., *Chem. Rev.* **2015**, *115* (5), 2136-2173.
90. Yella, A.; Lee, H.-W.; Tsao, H. N.; Yi, C.; Chandiran, A. K.; Nazeeruddin, M. K.; Diao, E. W.-G.; Yeh, C.-Y.; Zakeeruddin, S. M.; Grätzel, M., *Science* **2011**, *334* (6056), 629-634.
91. Listorti, A.; O'Regan, B.; Durrant, J. R., *Chem. Mater.* **2011**, *23* (15), 3381-3399.
92. Rowley, J. G.; Farnum, B. H.; Ardo, S.; Meyer, G. J., *J. Phys. Chem. Lett.* **2010**, *1* (20), 3132-3140.
93. Boschloo, G.; Gibson, E. A.; Hagfeldt, A., *J. Phys. Chem. Lett.* **2011**, *2* (24), 3016-3020.
94. Yan, B. J.; Schiff, E. A.; Shafarman, W. N., *Sol. Energy Mater. Sol. Cells* **2014**, *129*, 1-2.
95. Ardo, S.; Meyer, G. J., *Chem. Soc. Rev.* **2009**, *38* (1), 115-164.
96. Hagfeldt, A.; Boschloo, G.; Sun, L.; Kloo, L.; Pettersson, H., *Chem. Rev.* **2010**, *110* (11), 6595-6663.
97. Brown, D. G.; Schauer, P. A.; Borau-Garcia, J.; Fancy, B. R.; Berlinguette, C. P., *J. Am. Chem. Soc.* **2013**, *135* (5), 1692-1695.
98. Clark, A. E.; Hurst, J. K., Mechanisms of Water Oxidation Catalyzed by Ruthenium Coordination Complexes. In *Progress in Inorganic Chemistry, Vol 57*, Karlin, K. D., Ed. 2012; Vol. 57, pp 1-54.
99. Hurst, J. K., *Coord. Chem. Rev.* **2005**, *249* (3-4), 313-328.
100. Zeng, Q.; Lewis, F. W.; Harwood, L. M.; Hartl, F., *Coord. Chem. Rev.* **2015**, *304*, 88-101.
101. Concepcion, J. J.; Tsai, M.-K.; Muckerman, J. T.; Meyer, T. J., *J. Am. Chem. Soc.* **2010**, *132* (5), 1545-1557.

102. Wasylenko, D. J.; Ganesamoorthy, C.; Henderson, M. A.; Koivisto, B. D.; Osthoff, H. D.; Berlinguette, C. P., *J. Am. Chem. Soc.* **2010**, *132* (45), 16094-16106.
103. Chen, Z.; Concepcion, J. J.; Jurss, J. W.; Meyer, T. J., *J. Am. Chem. Soc.* **2009**, *131* (43), 15580-15581.
104. Vannucci, A. K.; Alibabaei, L.; Losego, M. D.; Concepcion, J. J.; Kalanyan, B.; Parsons, G. N.; Meyer, T. J., *Proc. Natl. Acad. Sci.* **2013**, *110* (52), 20918-20922.
105. Concepcion, J. J.; Binstead, R. A.; Alibabaei, L.; Meyer, T. J., *Inorg. Chem.* **2013**, *52* (19), 10744-10746.
106. Zhong, D. K.; Zhao, S.; Polyansky, D. E.; Fujita, E., *J. Catal.* **2013**, *307*, 140-147.
107. Sheehan, S. W.; Thomsen, J. M.; Hintermair, U.; Crabtree, R. H.; Brudvig, G. W.; Schmuttenmaer, C. A., *Nat. Commun.* **2015**, *6*, 6469.
108. Klepser, B. M.; Bartlett, B. M., *J. Am. Chem. Soc.* **2014**, *136* (5), 1694-1697.
109. Budnikov, G. K., *J. Anal. Chem.* **2000**, *55* (11), 1007-1007.
110. Matsuda, H., *Denki Kagaku* **1993**, *61* (9), 1073-1076.
111. Zolotov, Y. A., *J. Anal. Chem.* **1994**, *49* (9), 811-811.
112. Zeng, Z. H.; Chan, M. K. Y.; Zhao, Z. J.; Kubal, J.; Fan, D. X.; Greeley, J., *J. Phys. Chem. C* **2015**, *119* (32), 18177-18187.
113. Bard, A. J., *Nature* **1994**, *368* (6472), 597-598.
114. McEvoy, A. J., Fundamentals and applications of electrochemistry. In *New Strategies for Energy Generation, Conversion and Storage*, Cifarelli, L.; Wagner, F.; Wiersma, D. S., Eds. 2013; Vol. 54.
115. Trammell, S. A.; Meyer, T. J., *J. Phys. Chem. B* **1999**, *103* (1), 104-107.
116. Trammell, S. A.; Wimbish, J. C.; Odobel, F.; Gallagher, L. A.; Narula, P. M.; Meyer, T. J., *J. Am. Chem. Soc.* **1998**, *120* (50), 13248-13249.
117. Binstead, R. A.; Moyer, B. A.; Samuels, G. J.; Meyer, T. J., *J. Am. Chem. Soc.* **1981**, *103* (10), 2897-2899.
118. Binstead, R. A.; Meyer, T. J., *J. Am. Chem. Soc.* **1987**, *109* (11), 3287-3297.
119. Schulze, B.; Escudero, D.; Friebe, C.; Siebert, R.; Goerls, H.; Koehn, U.; Altuntas, E.; Baumgaertel, A.; Hager, M. D.; Winter, A.; Dietzek, B.; Popp, J.; Gonzalez, L.; Schubert, U. S., *Chem. Eur. J.* **2011**, *17* (20), 5494-5498.
120. Campagna, S.; Puntoriero, F.; Nastasi, F.; Bergamini, G.; Balzani, V., *Top. Curr. Chem.* **2007**, *280* (Photochemistry and Photophysics of Coordination Compounds I), 117-214.
121. Hofmeier, H.; Schubert, U. S., *Chem. Soc. Rev.* **2004**, *33* (6), 373-399.
122. Bomben, P. G.; Robson, K. C. D.; Berlinguette, C. P., *Coord. Chem. Rev.* **2012**, DOI: 10.1016/j.bbr.2011.03.031.
123. Tyson, D. S.; Luman, C. R.; Zhou, X.; Castellano, F. N., *Inorg. Chem.* **2001**, *40* (16), 4063-4071.
124. Damrauer, N. H.; Cerullo, G.; Yeh, A.; Boussie, T. R.; Shank, C. V.; McCusker, J. K., *Science* **1997**, *275* (5296), 54-57.
125. Baranoff, E.; Collin, J.-P.; Flamigni, L.; Sauvage, J.-P., *Chem. Soc. Rev.* **2004**, *33* (3), 147-155.
126. Schramm, F.; Meded, V.; Fliegl, H.; Fink, K.; Fuhr, O.; Qu, Z.; Klopper, W.; Finn, S.; Keyes, T. E.; Ruben, M., *Inorg. Chem.* **2009**, *48* (13), 5677-5684.
127. Breivogel, A.; Förster, C.; Heinze, K., *Inorg. Chem.* **2010**, *49* (15), 7052-7056.
128. Hammarström, L.; Johansson, O., *Coord. Chem. Rev.* **2010**, *254* (21, Äi22), 2546-2559.

129. Abrahamsson, M.; Jäger, M.; Osterman, T.; Eriksson, L.; Persson, P.; Becker, H.-C.; Johansson, O.; Hammarström, L., *J. Am. Chem. Soc.* **2006**, *128* (39), 12616-7.
130. Österman, T.; Abrahamsson, M.; Becker, H.-C.; Hammarström, L.; Persson, P., *J. Phys. Chem. A* **2012**, *116* (3), 1041-1050.
131. Abrahamsson, M.; Jäger, M.; Kumar Rohan, J.; Osterman, T.; Persson, P.; Becker, H.-C.; Johansson, O.; Hammarström, L., *J. Am. Chem. Soc.* **2008**, *130* (46), 15533-42.
132. Robson, K. C. D.; Koivisto, B. D.; Yella, A.; Spornova, B.; Nazeeruddin, M. K.; Baumgartner, T.; Grätzel, M.; Berlinguette, C. P., *Inorg. Chem.* **2011**, *50* (12), 5494-5508.
133. Schulze, B.; Escudero, D.; Friebe, C.; Siebert, R.; Görls, H.; Sinn, S.; Thomas, M.; Mai, S.; Popp, J.; Dietzek, B.; González, L.; Schubert, U. S., *Chem. Eur. J.* **2012**, *18* (13), 3785-3785.
134. Medlycott, E. A.; Hanan, G. S., *Chem. Soc. Rev.* **2005**, *34* (2), 133-142.
135. Collin, J. P.; Beley, M.; Sauvage, J. P.; Barigelletti, F., *Inorg. Chim. Acta.* **1991**, *186* (1), 91-93.
136. Djukic, J. P.; Sortais, J. B.; Barloy, L.; Pfeffer, M., *Eur. J. Inorg. Chem.* **2009**, (7), 817-853.
137. Chi, Y.; Chou, P.-T., *Chem. Soc. Rev.* **2007**, *36* (9), 1421-1431.
138. Englman, R.; Jortner, J., *Mol. Phys.* **1970**, *18* (2), 145-164.
139. Freed, K. F.; Jortner, J., *J. Chem. Phys.* **1970**, *52* (12), 6272-6291.
140. Constable, E. C.; Thompson, A.; Tocher, D. A.; Daniels, M. A. M., *New J. Chem.* **1992**, *16* (8-9), 855-867.
141. Collin, J. P.; Kayhanian, R.; Sauvage, J. P.; Calogero, G.; Barigelletti, F.; DeCian, A.; Fischer, J., *Chem. Comm.* **1997**, (8), 775-776.
142. Shin, Y.; Fryxell, G. E.; Johnson, C. A., II; Haley, M. M., *Chem. Mater.* **2008**, *20* (3), 981-986.
143. Masnovi, J. M.; Sankararaman, S.; Kochi, J. K., *J. Am. Chem. Soc.* **1989**, *111* (6), 2263-76.
144. Constable, E. C.; Dunphy, E. L.; Housecroft, C. E.; Neuburger, M.; Schaffner, S.; Schaper, F.; Batten, S. R., *Dalton Trans* **2007**, (38), 4323-4332.
145. Yella, A.; Lee, H. W.; Tsao, H. N.; Yi, C. Y.; Chandiran, A. K.; Nazeeruddin, M. K.; Diau, E. W. G.; Yeh, C. Y.; Zakeeruddin, S. M.; Gratzel, M., *Science* **2011**, *334* (6056), 629-634.
146. Bomben, P. G.; Borau-Garcia, J.; Berlinguette, C. P., *Chem. Commun.* **2012**, *48* (45), 5599-5601.
147. Bomben, P. G.; Robson, K. C. D.; Koivisto, B. D.; Berlinguette, C. P., *Coord. Chem. Rev.* **2012**, *256* (15-16), 1438-1450.
148. Schulze, B.; Brown, D. G.; Robson, K. C. D.; Friebe, C.; Jäger, M.; Birckner, E.; Berlinguette, C. P.; Schubert, U. S., *Chem. Eur. J.* **2013**, *19* (42), 14171-14180.
149. Sinn, S.; Schulze, B.; Friebe, C.; Brown, D. G.; Jäger, M.; Altuntaş, E.; Kübel, J.; Guntner, O.; Berlinguette, C. P.; Dietzek, B.; Schubert, U. S., *Inorg. Chem.* **2014**, *53* (4), 2083-2095.
150. Sinn, S.; Schulze, B.; Friebe, C.; Brown, D. G.; Jäger, M.; Kübel, J.; Dietzek, B.; Berlinguette, C. P.; Schubert, U. S., *Inorg. Chem.* **2014**, *53* (3), 1637-1645.
151. Green, M. A.; Emery, K.; Hishikawa, Y.; Warta, W., *Prog. Photovoltaics* **2010**, *18* (2), 144-150.
152. Nguyen, P. T.; Andersen, A. R.; Skou, E. M.; Lund, T., *Sol. Energy Mater. Sol. Cells* **2010**, *94* (10), 1582-1590.

153. Asghar, M. I.; Miettunen, K.; Halme, J.; Vahermaa, P.; Toivola, M.; Aitola, K.; Lund, P., *Energy Environ. Sci.* **2010**, *3* (4), 418-426.
154. Wang, M.; Moon, S.-J.; Xu, M.; Chittibabu, K.; Wang, P.; Cevey-Ha, N.-L.; Humphry-Baker, R.; Zakeeruddin, S. M.; Grätzel, M., *Small* **2010**, *6* (2), 319-324.
155. Yanagida, S.; Yu, Y.; Manseki, K., *Acc. Chem. Res.* **2009**, *42* (11), 1827-1838.
156. Nguyen, P. T.; Degn, R.; Nguyen, H. T.; Lund, T., *Sol. Energy Mater. Sol. Cells* **2009**, *93* (11), 1939-1945.
157. Bomben, P. G.; Robson, K. C. D.; Sedach, P. A.; Berlinguette, C. P., *Inorg. Chem.* **2009**, *48* (20), 9631-9643.
158. Bomben, P. G.; Gordon, T. J.; Schott, E.; Berlinguette, C. P., *Angew. Chem. Int. Ed.* **2011**, *50* (45), 10682-10685.
159. Gao, F.; Wang, Y.; Shi, D.; Zhang, J.; Wang, M.; Jing, X.; Humphry-Baker, R.; Wang, P.; Zakeeruddin, S. M.; Grätzel, M., *J. Am. Chem. Soc.* **2008**, *130* (32), 10720-10728.
160. Galoppini, E., *Coord. Chem. Rev.* **2004**, *248* (13-14), 1283-1297.
161. Hanson, K.; Brennaman, M. K.; Luo, H. L.; Glasson, C. R. K.; Concepcion, J. J.; Song, W. J.; Meyer, T. J., *ACS Appl. Mater. Interfaces* **2012**, *4* (3), 1462-1469.
162. Bae, E. Y.; Choi, W. Y.; Park, J. W.; Shin, H. S.; Kim, S. B.; Lee, J. S., *J. Phys. Chem. B* **2004**, *108* (37), 14093-14101.
163. Gillaizeau-Gauthier, I.; Odobel, F.; Alebbi, M.; Argazzi, R.; Costa, E.; Bignozzi, C. A.; Qu, P.; Meyer, G. J., *Inorg. Chem.* **2001**, *40* (23), 6073-6079.
164. Bae, E.; Choi, W., *J. Phys. Chem. B* **2006**, *110* (30), 14792-14799.
165. Park, H.; Bae, E.; Lee, J. J.; Park, J.; Choi, W., *J. Phys. Chem. B* **2006**, *110* (17), 8740-8749.
166. Ernstorfer, R.; Gundlach, L.; Felber, S.; Storck, W.; Eichberger, R.; Willig, F., *J. Phys. Chem. B* **2006**, *110* (50), 25383-25391.
167. Mulhern, K. R.; Orchard, A.; Watson, D. F.; Detty, M. R., *Langmuir* **2012**, *28* (17), 7071-7082.
168. Hanson, K.; Brennaman, M. K.; Ito, A.; Luo, H.; Song, W.; Parker, K. A.; Ghosh, R.; Norris, M. R.; Glasson, C. R. K.; Concepcion, J. J.; Lopez, R.; Meyer, T. J., *J. Phys. Chem. C* **2012**, *116* (28), 14837-14847.
169. Robson, K. C. D.; Bomben, P. G.; Berlinguette, C. P., *Dalton Trans* **2012**, *41* (26), 7814-7829.
170. Finnie, K. S.; Bartlett, J. R.; Woolfrey, J. L., *Langmuir* **1998**, *14* (10), 2744-2749.
171. Zhang, Z. P.; Zakeeruddin, S. M.; O'Regan, B. C.; Humphry-Baker, R.; Grätzel, M., *J. Phys. Chem. B* **2005**, *109* (46), 21818-21824.
172. Suto, K.; Konno, A.; Kawata, Y.; Tasaka, S.; Sugita, A., *Chem. Phys. Lett.* **2012**, *536*, 45-49.
173. Bazzan, G.; Deneault, J. R.; Kang, T.-S.; Taylor, B. E.; Durstock, M. F., *Adv. Funct. Mater.* **2011**, *21* (17), 3268-3274.
174. Ganbold, E.-O.; Lee, Y.; Lee, K.; Kwon, O.; Joo, S.-W., *Chem. Asian J.* **2010**, *5* (4), 852-858.
175. Nguyen, T. P.; Hesemann, P.; Gaveau, P.; Moreau, J. J. E., *J. Mater. Chem.* **2009**, *19* (24), 4164-4171.
176. Huang, W.; Zhang, R.; Zou, G.; Tang, J.; Sun, J., *J. Organomet. Chem.* **2007**, *692* (17), 3804-3809.

177. Wasylenko, D. J.; Ganesamoorthy, C.; Koivisto, B. D.; Henderson, M. A.; Berlinguette, C. P., *Inorg. Chem.* **2010**, *49* (5), 2202-2209.
178. Wasylenko, D. J.; Ganesamoorthy, C.; Borau-Garcia, J.; Berlinguette, C. P., *Chem. Commun.* **2011**, *47* (14), 4249-4251.
179. Wasylenko, D. J.; Palmer, R. D.; Schott, E.; Berlinguette, C. P., *Chem. Commun.* **2012**, *48* (15), 2107-2109.
180. Wasylenko, D. J.; Palmer, R. D.; Berlinguette, C. P., *Chem. Commun.* **2013**, *49* (3), 218-227.
181. Wasylenko, D. J.; Tatlock, H. M.; Bhandari, L. S.; Gardinier, J. R.; Berlinguette, C. P., *Chem. Sci.* **2013**, *4* (2), 734-738.
182. Fukuzumi, S.; Hong, D., *Eur. J. Inorg. Chem.* **2014**, *2014* (4), 645-659.
183. Khan, M. M. T.; Ramachandraiah, G.; Mehta, S. H.; Abdi, S. H. R.; Kumar, S., *Chemical J. Mol. Catal.* **1990**, *58* (2), 199-203.
184. Tong, L.; Thummel, R. P., *Chem. Sci.* **2016**, *7* (11), 6591-6603.
185. Francàs, L.; Bofill, R.; García-Antón, J.; Escriche, L.; Sala, X.; Llobet, A., Ru-Based Water Oxidation Catalysts. In *Molecular Water Oxidation Catalysis*, John Wiley & Sons, Ltd: 2014; pp 29-50.
186. Huynh, M. H. V.; Meyer, T. J., *Chem. Rev.* **2007**, *107* (11), 5004-5064.
187. Romain, S.; Vigara, L.; Llobet, A., *Acc. Chem. Res.* **2009**, *42* (12), 1944-1953.
188. Oki, A. R.; Morgan, R. J., *Synth. Commun.* **1995**, *25* (24), 4093-4097.
189. Miyoshi, D.; Karimata, H.; Wang, Z.-M.; Koumoto, K.; Sugimoto, N., *J. Am. Chem. Soc.* **2007**, *129* (18), 5919-5925.
190. Sauvage, F., *Adv. Chem.* **2014**, *2014*, 23.
191. She, C.; Guo, J.; Irle, S.; Morokuma, K.; Mohler, D. L.; Zabri, H.; Odobel, F.; Youm, K.-T.; Liu, F.; Hupp, J. T.; Lian, T., *J. Phys. Chem. A* **2007**, *111* (29), 6832-6842.
192. Nazeeruddin, M. K.; Humphry-Baker, R.; Officer, D. L.; Campbell, W. M.; Burrell, A. K.; Grätzel, M., *Langmuir* **2004**, *20* (15), 6514-6517.
193. Hettler, D. G. H.; Reek, J. N. H., *Angew. Chem. Int. Ed.* **2012**, *51* (39), 9740-9747.
194. Swierk, J. R.; Mallouk, T. E., *Chem. Soc. Rev.* **2013**, *42* (6), 2357-2387.
195. Hanson, K.; Brennaman, M. K.; Luo, H.; Glasson, C. R. K.; Concepcion, J. J.; Song, W.; Meyer, T. J., *ACS Appl. Mater. Interfaces* **2012**, *4* (3), 1462-1469.
196. Shi, P.; Amb, C. M.; Dyer, A. L.; Reynolds, J. R., *ACS Appl. Mater. Interfaces* **2012**, *4* (12), 6512-6521.
197. Colón, C. M.; Guadalupe, A. R., *Electroanalysis* **1998**, *10* (9), 621-627.
198. Yum, J.-H.; Baranoff, E.; Kessler, F.; Moehl, T.; Ahmad, S.; Bessho, T.; Marchioro, A.; Ghadiri, E.; Moser, J.-E.; Yi, C.; Nazeeruddin, M. K.; Grätzel, M., *Nat. Commun.* **2012**, *3*, 631.
199. Gong, J.; Sumathy, K.; Qiao, Q.; Zhou, Z., *Renew. Sustainable Energy Rev.* **2017**, *68*, Part 1, 234-246.
200. McCusker, J. K.; Rheingold, A. L.; Hendrickson, D. N., *Inorg. Chem.* **1996**, *35* (7), 2100-2112.
201. McCusker, J. K.; Walda, K. N.; Dunn, R. C.; Simon, J. D.; Magde, D.; Hendrickson, D. N., *J. Am. Chem. Soc.* **1993**, *115* (1), 298-307.
202. Monat, J. E.; McCusker, J. K., *J. Am. Chem. Soc.* **2000**, *122* (17), 4092-4097.

203. Smeigh, A. L.; Creelman, M.; Mathies, R. A.; McCusker, J. K., *J. Am. Chem. Soc.* **2008**, *130* (43), 14105-14107.
204. Zhang, W.; Alonso-Mori, R.; Bergmann, U.; Bressler, C.; Chollet, M.; Galler, A.; Gawelda, W.; Hadt, R. G.; Hartsock, R. W.; Kroll, T.; Kjaer, K. S.; Kubicek, K.; Lemke, H. T.; Liang, H. W.; Meyer, D. A.; Nielsen, M. M.; Purser, C.; Robinson, J. S.; Solomon, E. I.; Sun, Z.; Sokaras, D.; van Driel, T. B.; Vanko, G.; Weng, T.-C.; Zhu, D.; Gaffney, K. J., *Nature* **2014**, *509* (75), 345-348.
205. Juban, E. A.; Smeigh, A. L.; Monat, J. E.; McCusker, J. K., *Coord. Chem. Rev.* **2006**, *250* (13-14), 1783-1791.
206. Cannizzo, A.; Milne, C. J.; Consani, C.; Gawelda, W.; Bressler, C.; van Mourik, F.; Chergui, M., *Coord. Chem. Rev.* **2010**, *254* (21-22), 2677-2686.
207. Jamula, L. L.; Brown, A. M.; Guo, D.; McCusker, J. K., *Inorg. Chem.* **2014**, *53* (1), 15-17.
208. Yang, M.; Thompson, D. W.; Meyer, G. J., *Inorg. Chem.* **2000**, *39* (17), 3738-+.
209. Yang, M.; Thompson, D. W.; Meyer, G. J., *Inorg. Chem.* **2002**, *41* (5), 1254-1262.
210. Liu, Y.; Kjaer, K. S.; Fredin, L. A.; Chabera, P.; Harlang, T.; Canton, S. E.; Lidin, S.; Zhang, J.; Lomoth, R.; Bergquist, K.-E.; Persson, P.; Warnmark, K.; Sundstrom, V., *Chem. Eur. J.* **2015**, *21* (9), 3628-3639.
211. Frisch, M. J.; Trucks, G. W.; Schlegel, H. B.; Scuseria, G. E.; Robb, M. A.; Cheeseman, J. R.; Scalmani, G.; Barone, V.; Mennucci, B.; Petersson, G. A.; Nakatsuji, H.; Caricato, M.; Li, X.; Hratchian, H. P.; Izmaylov, A. F.; Bloino, J.; Zheng, G.; Sonnenberg, J. L.; Hada, M.; Ehara, M.; Toyota, K.; Fukuda, R.; Hasegawa, J.; Ishida, M.; Nakajima, T.; Honda, Y.; Kitao, O.; Nakai, H.; Vreven, T.; Montgomery, J. A.; Peralta, J. E.; Ogliaro, F.; Bearpark, M.; Heyd, J. J.; Brothers, E.; Kudin, K. N.; Staroverov, V. N.; Kobayashi, R.; Normand, J.; Raghavachari, K.; Rendell, A.; Burant, J. C.; Iyengar, S. S.; Tomasi, J.; Cossi, M.; Rega, N.; Millam, J. M.; Klene, M.; Knox, J. E.; Cross, J. B.; Bakken, V.; Adamo, C.; Jaramillo, J.; Gomperts, R.; Stratmann, R. E.; Yazyev, O.; Austin, A. J.; Cammi, R.; Pomelli, C.; Ochterski, J. W.; Martin, R. L.; Morokuma, K.; Zakrzewski, V. G.; Voth, G. A.; Salvador, P.; Dannenberg, J. J.; Dapprich, S.; Daniels, A. D.; Farkas, Foresman, J. B.; Ortiz, J. V.; Cioslowski, J.; Fox, D. J., Gaussian 09, Revision B.01. Wallingford CT, 2009.
212. Dennington, R.; Keith, T.; Millam, J. *GaussView*, Semichem Inc.: Shawnee Mission KS, 2009.
213. Wadt, W. R.; Hay, P. J., *J. Chem. Phys.* **1985**, *82* (1), 284-298.
214. Hay, P. J.; Wadt, W. R., *J. Chem. Phys.* **1985**, *82* (1), 299-310.
215. Hay, P. J.; Wadt, W. R., *J. Chem. Phys.* **1985**, *82* (1), 270-283.
216. Rassolov, V. A.; Ratner, M. A.; Pople, J. A.; Redfern, P. C.; Curtiss, L. A., *J. Comput. Chem.* **2001**, *22* (9), 976-984.
217. Francl, M. M.; Pietro, W. J.; Hehre, W. J.; Binkley, J. S.; Gordon, M. S.; Defrees, D. J.; Pople, J. A., *J. Chem. Phys.* **1982**, *77* (7), 3654-3665.
218. Tomasi, J.; Mennucci, B.; Cammi, R., *Chem. Rev.* **2005**, *105* (8), 2999-3093.
219. O'Boyle, N. M.; Tenderholt, A. L.; Langner, K. M., *J. Comp. Chem.* **2008**, *29*, 839-845.
220. Otwinowski, Z.; Minor, W., *Methods Enzymol.* **1997**, *276* (Macromolecular Crystallography, Part A), 307-326.
221. Hoof, R., *COLLECT: Users Manual, Nonius B.V., Delft*. The Netherlands, 1998.
222. Altomare, A.; Cascarano, G.; Giacovazzo, C.; Guagliardi, A., *Journal of Applied Crystallography* **1993**, *26* (3), 343-50.

223. Beurskens, P. T. A., G.; Beurskens, G.; Bosman, W. P.; de Gelder, R.; Israel, R.; Smits, J. M. M., *The DIRDIF-94 program system, Technical Report of the Crystallography Laboratory*. University of Nijmegen, The Netherlands, 1994.
224. Sheldrick, G. M., *Acta Crystallographica, Section A: Foundations of Crystallography* **2008**, *A64* (1), 112-122.
225. Spek, A. L., *PLATON/SQUEEZE A multipurpose crystallographic tool*. Utrecht University, 2000.